Technische Universität München

Max-Planck-Institut für Physik
(Werner-Heisenberg-Institut)

Development of Segmented Germanium Detectors for Neutrinoless Double Beta Decay Experiments

Jing Liu

Vollständiger Abdruck der von der Fakultät für Physik der Technischen Universität
München zur Erlangung des akademischen Grades eines
Doktors der Naturwissenschaften (Dr. rer. nat.)
genehmigten Dissertation.

Vorsitzender:	Univ.-Prof. Dr. Alejandro Ibarra
Prüfer der Dissertation:	1. Hon.-Prof. Allen C. Caldwell, Ph.D. 2. Univ.-Prof. Dr. Franz von Feilitzsch

Die Dissertation wurde am 20.04.2009 bei der Technischen Universität München
eingereicht und durch die Fakultät für Physik am 09.06.2009 angenommen.

Abstract

The results from neutrino oscillation experiments indicate that at least two neutrinos have mass. However, the value of the masses and whether neutrinos and anti-neutrinos are identical, *i.e.*, Majorana particles, remain unknown. Neutrinoless double beta decay experiments can help to improve our understanding in both cases and are the only method currently possible to tackle the second question.

The GERmanium Detector Array (GERDA) experiment, which will search for the neutrinoless double beta decay of ^{76}Ge, is currently under construction in Hall A of the INFN Gran Sasso National Laboratory (LNGS), Italy. In order to achieve an extremely low background level, segmented germanium detectors are considered to be operated directly in liquid argon which serves simultaneously as cooling and shielding medium.

Several test cryostats were built at the Max-Planck-Institut für Physik in München to operate segmented germanium detectors both in vacuum and submerged in cryogenic liquid. The performance and the background discrimination power of segmented germanium detectors were studied in detail. It was proven for the first time that segmented germanium detectors can be operated stably over long periods submerged in a cryogenic liquid. It was confirmed that the segmentation scheme employed does well in the identification of photon induced background and demonstrated for the first time that also neutron interactions can be identified.

The C++ Monte Carlo framework, MaGe (Majorana-GERDA), is a joint development of the Majorana and GERDA collaborations. It is based on GEANT4, but tailored especially to simulate the response of ultra-low background detectors to ionizing radiation. The predictions of the simulation were verified to be accurate for a wide range of conditions. Some shortcomings were found and corrected.

Pulse shape analysis is complementary to segmentation in identifying background events. Its efficiency can only be correctly determined using reliable pulse shape simulations. A fully functional pulse shape simulation package was developed to augment the MaGe package. The simulation was verified using data taken with the first segmented prototype detector for GERDA. This work also led to a considerable improvement in the understanding of segmented germanium detectors.

Zusammenfassung

Die Ergebnisse von Neutrinooszillationsexperimenten zeigen, dass mindestens zwei Neutrinos eine endliche Masse haben. Die absolute Massenskala ist jedoch nicht bekannt. Ungelöst ist auch die Frage, ob das Neutrino sein eigenes Antiteilchen ist, *i.e.*, ob Neutrinos Majoranateilchen sind. Eine mögliche Beobachtung von neutrinolosem Doppelbetazerfall könnte zur Feststellung der Massenskala beitragen und ist im Moment die einzige realisierbare Möglichkeit, die Frage nach der Natur der Neutrinos zu klären.

Das GERmanium Detector Array (GERDA) für die Suche nach neutrinolosem Doppelbetazerfall von ^{76}Ge wird derzeit in der Halle A des "INFN Gran Sasso National Laboratory (LNGS)" in Italien aufgebaut. Um ein extrem niedriges Untergrundniveau zu ereichen, werden segmentierte Germaniumdetektoren direkt in flüssigem Argon, das gleichzeitig als Kühl-und Abschirmmedium dient, betrieben.

Mehrere Testkryostaten wurden für den Betrieb segmentierter Germaniumdetektoren in Vakuum und kryogener Flüssigkeit am Max-Planck-Institut für Physik in München entwickelt. Es wurde zum ersten Mal gezeigt, dass segmentierte Germaniumdetektoren über lange Zeit stabil in einer kryogenen Flüssigkeit betrieben werden können. Die Möglichkeiten, Untergrundereignisse in segmentierten Germaniumdetektoren zu identifizieren, wurden im Detail untersucht. Dabei wurde betstätigt, dass geeignete Segmentierung die Identifikation von photoninduzierten Ereignissen ermöglicht und zum ersten Mal gezeigt, dass auch neutroninduzierte Ereignisse identifiziert werden können.

Das C++ Monte Carlo Paket MaGe (Majorana-GERDA) ist ein Gemeinschaftprojekt der Majorana und GERDA Kollaborationen. Es basiert auf GEANT4, ist aber zurechtgeschnitten auf die Simulation der Wechselwirkungen ionisierender Strahlung mit Detektoren für Experimente in einer Umgebung mit extrem niedriger Radioaktivität. Die Simulationen wurden mit Daten überprüft. Daten und Simulation stimmen für viele Anwendungsfälle gut überein.

Pulsformanalyse kann Segmentierung bei der Identifikation von dem Untergrund zuzurechnenden Ereignistopologien ergänzen. Zur Ermittlung der Effizienz von Pulsformanalysen wird eine exakte Pulsformsimulation benötigt. Ein komplettes Pulsformsimulationspaket wurde im Rahmen diesr Arbeit entwickelt. Die simulierten Pulse wurden mit Messungen am ersten segmentierten Prototypdetektor verglichen und den Daten erfolgreich angepasst. Dabei wurde auch das Verständnis der Detektoren signifikant verbessert.

Table of Contents

Introduction

At the time the *Standard Model* was established the neutrino was believed to be massless. In experiments it always had the same chirality and there was no evidence for a non-zero mass. However, the picture changed dramatically when neutrino oscillations were observed in solar and atmospheric neutrinos. They were explained by the weak interaction eigenstates of neutrinos being admixtures of mass eigenstates and the latter propagating with different velocities. The introduction of neutrino mass terms into the Standard Model became necessary.

There are various methods to introduce neutrino mass terms into the Standard Model. The most straightforward approach is to follow the same procedure as for the charged leptons; *i.e.*, the leptons obtain mass by coupling to the Higgs field. The problems of this approach are that it does not explain why neutrinos couple to the Higgs field so weakly compared to their charged partners, and that it requires the introduction of right-handed neutrinos which have not yet been experimentally observed. An elegant way to solve these problems is to assume that neutrinos are Majorana particles; *i.e.*, their own anti-particles. This way, the second problem does not arise, and once the Majorana mass terms are introduced into the Lagrangian, the so-called *see-saw mechanism* can make the different coupling strengths look natural.

The only experimental test currently possible to verify that neutrinos are Majorana particles is the search for neutrinoless double beta ($0\nu\beta\beta$) decay. In this process, a neutrino emitted from one neutron is absorbed as an anti-neutrino by another neutron. This can only occur if neutrinos are of Majorana type. About ten naturally occurring isotopes are observed to undergo double-beta decay. Among them, ^{76}Ge is of special importance because germanium is a semiconductor material used in highly efficient detectors with very good energy resolution (it can serve as source and detector simultaneously), and it is one of the purest materials produced in the world limiting intrinsic background.

The GERDA (GERmanium Detector Array) experiment [1,2], searching for the $0\nu\beta\beta$ decay of ^{76}Ge, is currently under construction in Hall A of the INFN Gran Sasso National Laboratory (LNGS), Italy. In order to achieve an extremely low background level, it is considered to use 18-fold segmented germanium detectors operated directly in cryogenic liquid, serving as cooling and shielding material, in the second phase of GERDA. The main goals of the work presented in this thesis are to examine systematically the operation and performance of segmented detectors in cryogenic liquid and to investigate their power of background discrimination by analyzing the spatial distribution over which energy is deposited. The time structure of the detector response is studied and simulated to lay the foundation for its use in background suppression.

Two test facilities were used to take data with two 18-fold segmented GERDA Phase II prototype detectors:
Gerdalinchen II, a specially designed cryostat containing liquid nitrogen or argon, inside which up to three segmented detectors can be operated simultaneously. It was used

- to operate and study for the first time segmented detectors submerged directly in cryogenic liquid.
- to develop detailed operating procedures.
- to carefully study the data of a prototype detector.

A vacuum cryostat, especially equipped to operate one segmented detector. It allowed

- the analysis of background induced by external photons in the MeV-energy range. These photons typically undergo multiple Compton scattering and deposit their energies over a range of several centimeters. This distinguishes them from the electrons from $0\nu\beta\beta$ decay which deposit energy on a millimeter scale.
- the analysis of background induced by neutron interactions with germanium isotopes and surrounding materials. Most of the neutron induced events deposit their energies in several segments of the detector. In particular, the inelastic scattering of neutrons on germanium isotopes can be identified through the separation of the energies deposited by the prompt photon and the nuclear recoil.
- the characterization of the detector, including the segment boundaries, crystal axes, impurities, *etc.*. The data was used to study the time structure of the detector response, *i.e.*, the pulse shape and to verify the corresponding simulations.

The test facilities were modeled using a Geant4 based simulation framework, MaGe, which is jointly developed by the GERDA and Majorana collaborations. The simulation of low energy electrons, photons and neutrons interacting with germanium detectors and surrounding materials were verified in detail. A fully functional pulse shape simulation package was also developed within the MaGe framework. The whole signal formation process in segmented germanium detectors and the read-out system was simulated and verified by being compared with data.

The thesis is structured as follows:

Chapter 1 describes the theoretical background for $0\nu\beta\beta$ decay as well as other approaches to test whether neutrinos are of Majorana or Dirac type.

Chapter 2 summarizes different technical approaches for searching for $0\nu\beta\beta$ decays of different isotopes, compares the experiments with each other and estimates the potential of future $0\nu\beta\beta$ decay experiments.

Chapter 3 introduces the basic ideas of the GERDA experiment, summarizes the latest progress, and estimates the potential of GERDA.

Chapter 4 describes the basic concepts of semiconductor detectors and the important properties of germanium crystals and detectors related to the later analysis.

Chapter 5 introduces the two test stands that provided the data for all studies and describes the slow control and data acquisition system on which the test stands rely.

Chapter 6 characterizes the short and long term performance of segmented germanium detectors submerged in cryogenic liquid.

Chapter 7 describes a special class of events with negative baseline shifts.

Chapter 8 demonstrates the power of segmented detectors to identify photon induced background and verifies the Monte Carlo simulation.

Chapter 9 demonstrates the power of segmented detectors to identify neutron interactions with germanium isotopes and surrounding materials and validates the simulation in this aspect as well.

Chapter 10 describes the physics models of the charge carrier drift inside germanium detectors to simulate the pulse shape and introduces methods to add electronic effects.

Chapter 11 verifies the pulse shape simulation by comparing it to the data taken with the GERDA prototype detector and introduces new methods to determine the crystal orientation and impurity distributions.

The results are summarized within the context of the GERDA Phase II experiment and an outlook to further studies is given.

Chapter 1

Neutrino mass and its origin

Neutrinos were introduced into the *Standard Model* as massless particles. Strong evidence from neutrino oscillation experiments indicates that at least two of the neutrinos have mass. Neutrino mass terms can be introduced into the Standard Model within the Dirac or the Majorana formalism. If the latter describes nature, neutrinos are their own antiparticles. Constraints on the neutrino mass scale come from different aspects of physics. Cosmology constrains the sum of the masses of all flavors. Single beta decay experiments measure the mass of the electron neutrino and are sensitive to the neutrino mixing parameters. Neutrinoless double beta decay can only occur if neutrinos are of Majorana type. The decay rate would allow the determination of the effective Majorana neutrino mass.

1.1 Neutrinos in the Standard Model

In the Standard Model neutrinos are assumed to be fermions with spin 1/2 and rest mass $m_\nu = 0$. They always have fixed helicity because there is no frame of reference moving faster than a neutrino, in which the helicity of the neutrino could change its sign. Neutrinos and anti-neutrinos are assumed to be different particles. Lepton numbers +1 and -1 are assigned to them, respectively, and lepton number is conserved. Only left-handed neutrinos and right-handed anti-neutrinos participate in the weak interaction. The field operators of right-handed neutrinos and left-handed anti-neutrinos do not exist in the Lagrangian of the weak interaction.

New experimental evidence, particularly neutrino oscillations, made a modification and extension of the Standard Model necessary. Crucial theoretical considerations and experimental observations are briefly reviewed in the following.

The neutrino was postulated to exist by W. Pauli in 1930 [3] in order to explain the continuous energy spectrum of electrons emitted from beta decay without abandoning the law of energy conservation. He assumed that it was a neutral fermion with spin 1/2, and its mass was of the same order of magnitude as the electron mass. E. Fermi soon developed his theory of beta decay [4, 5]. He investigated the influence of the neutrino mass on the shape of the beta spectrum and inferred that $m_\nu \approx 0$ by comparing the calculation to the experimental data. A precise measurement of the beta spectrum of tritium by L. Langer and R. Moffat in 1952 [6] gave an upper limit on the rest mass of the neutrino, $m_\nu \lessapprox 0.05 m_e$. The neutrino was assumed to be massless afterwards. Although the upper limit was pushed down again and again by later experiments, the possibility that neutrinos have very small masses was never completely ruled out, and was strongly supported by the neutrino oscillation experiments.

Beta plus decay was observed by I. Curie and J. F. Joliot in 1934 [7]. Beta decay and beta plus decay in a nucleus can be noted as follows:

$$\beta\text{-decay: } n \rightarrow p + e^- + \bar{\nu}_e, \tag{1.1}$$

$$\beta^+\text{-decay: } p \rightarrow n + e^+ + \nu_e. \tag{1.2}$$

According to Fermi's theory, the following processes also have to exist:

$$e^+ + n \rightarrow p + \bar{\nu}_e, \tag{1.3}$$

$$e^- + p \rightarrow n + \nu_e, \tag{1.4}$$

where instead of $e^{-/+}$ being emitted $e^{+/-}$ are absorbed. Process 1.4 occurring in a nucleus is called electron capture (EC in short). It was observed by L. W. Alvarez in 1938 [8]. In 1956, the inverse process of 1.3 was used by F. Reines and C. L. Cowan, Jr., to detect neutrinos from a nuclear reactor [9,10]. They proved for the first time that neutrinos do exist in nature.

Whether neutrinos accompanying e^+ and e^- are identical was of great interest at that time. Consider the inverse process of EC,

$$\nu_e + n \rightarrow p + e^-, \tag{1.5}$$

which, theoretically speaking, also has to exist[1]. If $\bar{\nu}$ and ν were identical, the following reaction with ν_e replaced by $\bar{\nu}_e$ would be possible:

$$\bar{\nu}_e + n \rightarrow p + e^-. \tag{1.6}$$

This was investigated by R. Davis in 1955 [11,12]. He was looking for

$$\bar{\nu}_e + {}^{37}\mathrm{Cl} \rightarrow {}^{37}\mathrm{Ar} + e^- \tag{1.7}$$

and reported a negative result. Before the observation of parity violation and neutrino oscillations this result supported the idea that $\bar{\nu}$ and ν are intrinsically different particles. To formulate this idea theoretically different *lepton numbers* were assigned to e^-, e^+, ν_e and $\bar{\nu}_e$:

$$+1 \text{ for } e^-, \nu_e, \; -1 \text{ for } e^+, \bar{\nu}_e, \tag{1.8}$$

and required to be conserved in interactions. The reaction described by Eq. 1.7 is thus forbidden by lepton number conservation.

---

[1] The process was experimentally proven to exist and used to detect solar neutrinos in many experiments.

In 1956 T. D. Lee and C. N. Yang found the existing evidence for parity conservation in weak interaction unsatisfactory and specified the experiments required [13]. Soon after parity violation was observed in the beta decay of ^{60}Co [14] and the creation and decay of muons [15, 16]. Lee and Yang [17] and some other authors [18, 19] started to apply the so-called two-component model [20] to the weak interaction. According to this model only the left-handed neutrino and right-handed anti-neutrino or right-handed neutrino and left-handed anti-neutrino participate in the weak interaction. In 1958 an elegant experiment was carried out by M. Goldhaber *et al.* to see whether the right-handed or left-handed components were preferred by nature [21]. By measuring the polarization of γ-rays emitted from ^{152}Sm* created in the electron capture, $^{152}\mathrm{Eu}(e^-, \nu)$, they inferred that neutrinos from $^{152}\mathrm{Eu}(e^-, \nu)$ were left-handed. Now the absence of reaction 1.7 could be explained in two different ways:

- $\bar{\nu}$ and ν behave differently because they are intrinsically different particles.
- $\bar{\nu}$ and ν behave differently only because they have different helicities.

In summary, though the *Standard Model* of weak interaction was a very successful theory some modifications were still possible:

- neutrinos could be massive;
- $\bar{\nu}$ and ν might not be different, and hence lepton number not conserved.

1.2 Neutrino oscillations

The assumption that neutrinos were massless was challenged in 1969 by Gribov and Pontecorvo who predicted that neutrinos might oscillate into different flavors if some of them were massive and if there was mixing between them [22]. This is what is called *neutrino oscillations.*

The theory of neutrino oscillations can be briefly summarized as follows: the mass eigenstates of neutrinos, ν_i, with mass m_i, are not the same as their weak interaction eigenstates, ν_α; the latter are combinations of the former

$$|\nu_\alpha\rangle = \sum_i U^*_{\alpha i}|\nu_i\rangle, \tag{1.9}$$

where $\alpha = e, \mu, \tau$, and $i = 1, 2, 3$, and U is a unitary matrix referred to as the Pontecorvo-Maki-Nakagawa-Sakata(PMNS) matrix. A common parameterization of the PMNS matrix is

$$\begin{aligned} U = &\begin{pmatrix} 1 & 0 & 0 \\ 0 & \cos\theta_{23} & \sin\theta_{23} \\ 0 & -\sin\theta_{23} & \cos\theta_{23} \end{pmatrix} \times \begin{pmatrix} \cos\theta_{13} & 0 & \sin\theta_{13}e^{-i\delta} \\ 0 & 1 & 0 \\ -\sin\theta_{13}e^{i\delta} & 0 & \cos\theta_{13} \end{pmatrix} \\ &\times \begin{pmatrix} \cos\theta_{12} & \sin\theta_{12} & 0 \\ -\sin\theta_{12} & \cos\theta_{12} & 0 \\ 0 & 0 & 1 \end{pmatrix} \times \begin{pmatrix} e^{i\alpha_1/2} & 0 & 0 \\ 0 & e^{i\alpha_2/2} & 0 \\ 0 & 0 & 1 \end{pmatrix}, \end{aligned} \tag{1.10}$$

where θ_{ij} are three mixing angles and δ, α_1 and α_2 are CP-violating phases. Especially, α_1 and α_2 are also called Majorana phases. They only have physical consequences, if neutrinos are Majorana particles. The probability that a neutrino originally of flavor α will be observed as having flavor β after traveling a distance L is

$$\begin{aligned} P_{\alpha\to\beta} &= |\langle\nu_\beta|\nu_\alpha(t)\rangle|^2 = \left|\sum_i U^*_{\alpha i}U_{\beta i}e^{-im_i^2 L/2E}\right|^2 \\ &= \Delta_{\alpha\beta} - 4\sum_{i>j} Re(U^*_{\alpha i}U_{\beta i}U_{\alpha j}U^*_{\beta j})\sin^2(\Delta m^2_{ij}\frac{L}{4E}) \\ &\quad + 2\sum_{i>j} Im(U^*_{\alpha i}U_{\beta i}U_{\alpha j}U^*_{\beta j})\sin(\Delta m^2_{ij}\frac{L}{2E}), \end{aligned} \tag{1.11}$$

where Δm^2_{ij} is the squared mass difference between the two mass eigenstates $m_i^2 - m_j^2$ and E is the average energy of the mass eigenstates.

Oscillations would not occur ($P_{\alpha\to\beta} = 0$) if neutrinos were all massless or all masses were degenerate ($\Delta m^2 = 0$) or there was no mixing ($\theta = 0$). As there are neutrino oscillations, at least two neutrinos must have mass and they must mix.

1.2.1 Solar neutrinos

The hypothesis of neutrino oscillations was first used to explain the problem of the solar neutrino flux [23,24], which was measured to be lower than that predicted by the standard solar model [25]. This explanation was at first not widely accepted because it required very large neutrino mixing and a fine-tuned squared mass difference to fit the distance between the Sun and the Earth. The uncertainties of the standard solar model were used to resolve the problem instead, *i.e.* to deny its existence.

It was first realized by L. Wolfenstein in 1978 that neutrinos propagating in matter have different effective masses than those in vacuum due to charged current coherent forward scattering of electron neutrinos with electrons in matter [26]. Since neutrino oscillations depend upon the squared mass difference of the neutrinos, they can be different in matter than in vacuum. S. P. Mikheyev and A. Yu. Smirnov noticed in 1986 that, even if the intrinsic oscillations were small, the matter effect could still cause maximal mixing between electron neutrinos and the other flavors [27]. Their observation is called MSW effect. Since this mechanism did not require the intrinsic mixing angle to be very large and the squared mass difference fine-tuned, people started to believe that neutrino oscillations might be the answer to the solar neutrino flux problem.

The experiments [28,29,30] following the chlorine experiment all observed solar neutrino deficits which were explained as the result of neutrino oscillations. The ranges of allowed neutrino mixing parameters were narrowed step by step. However, the most convincing evidence came from the combined results from the Sudbury Neutrino Observatory (SNO) [31] and Super-Kamiokande [32] in 2001. SNO measured precisely the neutrino flux through the charged current (CC) reaction, $\phi^{CC}(\nu_e)$, which is sensitive exclusively to ν_e. Super-Kamiokande measured precisely the neutrino flux through the elastic scattering

(ES), $\phi^{ES}(\nu_\alpha)$, which is sensitive to all active neutrino flavors ($\alpha = e, \mu, \tau$).[2] If ν_es from the sun change into other flavors $\phi^{CC}(\nu_e)$ should be smaller than $\phi^{ES}(\nu_\alpha)$. The experimental result was that $\phi^{CC}(\nu_e)$ was smaller than $\phi^{ES}(\nu_\alpha)$ with a 3.3σ difference. Since the result did not rely on solar model flux calculations the solar neutrino oscillation was finally well established.

1.2.2 Atmospheric neutrinos

Studies of atmospheric neutrinos also indicated the existence of neutrino oscillations. In the early 1980s several massive detectors were built to search for proton decays. Neutrinos created by cosmic rays in the atmosphere were studied in detail as a source of background events. A deficit in the muon neutrino flux relative to the electron neutrino flux compared with the calculation was found in two experiments, IMB [33] (1986) and Kamiokande [34] (1988). The IMB group, however, took the conservative attitude and ascribed the deficit to some unknown systematics. On the other hand, the Kamiokande group, relying on its capability to clearly separate e and μ events, interpreted it as evidence for neutrino oscillations.

Kamiokande further investigated this phenomenon and, in 1994, discovered that the flux of high energy muon neutrinos showed a nontrivial zenith-angle dependence that could best be explained by ν_μ oscillating to ν_τ [35]. This still did not convince everybody, because the oscillation interpretation required very large mixing between the two neutrino species which was not considered reasonable. Finally, Super-Kamiokande, the enlarged facility of Kamiokande, showed that all aspects of atmospheric neutrino data were consistent with neutrino oscillation between ν_μ and ν_τ, and the mixing was nearly maximal (1998) [36].

1.2.3 Reactor neutrinos

Neutrinos from artificial sources, reactors and accelerators, allow precise measurements of the oscillation parameters under more controlled and better understood conditions than solar and atmospheric neutrinos. Reactor neutrino experiments detect anti-neutrinos from the decays of radioactive fission products in the nuclear fuel. Detectors can be constructed at varying distances from the source, and hence variable sensitivity to different oscillation parameters. For instance, KamLAND [37] has a flux weighted average distance of ~ 180 km from more than 60 nuclear reactors around. It has better precision in the measurement of the mass difference Δm^2_{21} but is less sensitive to the mixing angle θ_{12} than the solar neutrino experiments. The combined fit of its and the solar neutrino experiments data gives the best results on Δm^2_{21} and $\sin^2\theta_{12}$ [38]. KamLAND can also detect the anti-neutrino energy. The energy spectrum clearly reflects the oscillation pattern, and thus excludes hypotheses such as neutrino decay and decoherence.

The Chooz experiment, instead, was situated only ~ 1000 m away from the reactors. It was sensitive to the PMNS matrix element U_{e3}, and gave the best limit on $\sin^2\theta_{13}$ [39].

---

[2] SNO also measured $\phi^{ES}(\nu_\alpha)$ with reduced sensitivity to ν_μ and ν_τ. The results were consistent with that from Super-Kamiokande. SNO published in 2002 the result of the neutral current (NC) measurement, which was also sensitive to all active neutrino flavors. The result was consistent with that from ES measurement.

Since θ_{13} modulates the effect of CP violation, a more precise determination of θ_{13} is of great interest. Using a second detector closer to the reactors the systematic uncertainties related to neutrino production and interaction cancel in relative measurements [40]. Following this idea, three experiments, Double Chooz [41], Daya Bay [42] and RENO [43], are under construction. Daya Bay aims at a sensitivity in $\sin^2 2\theta_{13}$ of better than 0.01 while Double Chooz and RENO aim at $0.02 \sim 0.03$ at 90% CL for 3 years measuring time.

1.2.4 Accelerator neutrinos

Neutrino beams from accelerators usually contain dominantly muon neutrinos or antineutrinos. Their energy is adjusted to the application and ranges from almost 0 to several hundred GeV. The close-far detector configuration is also used in some cases. Accelerator neutrino experiments hence can investigate different oscillation phenomena. K2K [44] and MINOS [45] measure a muon neutrino deficit and energy distribution in the far detector normalized to the observations in the close one. The aim is to precisely measure the squared mass difference and the mixing angle. Opera [46] searches for the appearance of τ neutrinos in the CERN muon neutrino beam. KARMEN [47] and LSND [48] searched for the appearance of electron neutrinos in their muon neutrino beams. The former reported a negative result, while the latter claimed the existence of $\nu_\mu/\bar{\nu}_\mu \rightarrow \nu_e/\bar{\nu}_e$ oscillations, but with quite a different mass difference squared as found in solar and atmosphere oscillation experiments. This could only be accommodated by the existence of extra sterile neutrinos. The evidence provided by LSND was partially refuted recently by MiniBOONE [49]. Further scrutiny is needed to exclude some more exotic possibilities. Two future experiments, T2K [50] and NOvA [51], are under construction to search for electron neutrino appearance and to measure the mixing angle θ_{13} and the CP violation phase δ.

1.2.5 Summary of neutrino oscillations

Neutrino oscillations have been observed not only in solar and atmospheric neutrino experiments but also in reactor and accelerator neutrino experiments. It is established that neutrinos do have masses. Comprehensive data analyses of the mass differences squared and the mixing parameters based on the 3-neutrino mixing scheme can be found in the latest *Review of Particle Physics* [52]. Since the oscillation experiments can only measure the mass differences between the neutrino mass eigenstates and cannot determine the signs of Δm^2_{23}, there are two interesting questions left as shown in Fig. 1.1:

- what are the absolute values of the neutrino masses?

- what is the real mass hierarchy? Does it correspond to the (normal) mass hierarchy of the charged lepton sector or is it inverted?

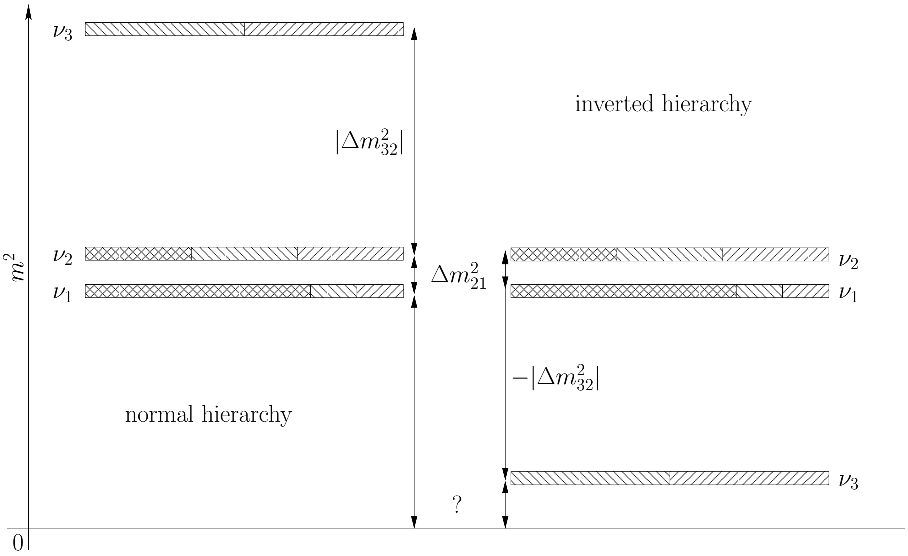

Figure 1.1: Possible neutrino mass squared spectra. The cross-, right- and left-hatched areas give the contributions of the electron, muon and tau neutrino flavor eigenstates to the neutrino mass eigenstates. Oscillation experiments can neither help to determine the absolute mass scale nor to distinguish between normal and inverted hierarchy.

1.3 Neutrino mass terms

The observation of neutrino oscillations makes the introduction of neutrino mass terms into the Standard Model necessary.

1.3.1 Dirac mass terms

The most straightforward approach to introduce mass terms is to follow the same procedure as for the electron; *i.e.*, the lepton obtains mass by coupling to the Higgs field. The mass term of the electron can be expressed as

$$-\mathcal{L}_e \equiv m_e \bar{e} e = g_e \langle h^0 \rangle \bar{e} e, \tag{1.12}$$

with $m_e = g_e \langle h^0 \rangle$, where g_e is the coupling strength of the electron field e to the Higgs field, and $\langle h^0 \rangle$ is the vacuum expectation value of the Higgs field. Similarly, the Dirac mass term of the neutrino can be introduced as

$$-\mathcal{L}_\nu^D \equiv m_D \bar{\nu} \nu = g_\nu \langle h^0 \rangle \bar{\nu} \nu, \tag{1.13}$$

with $m_D = g_\nu \langle h^0 \rangle$, where g_ν is the coupling strength of the neutrino field ν to the Higgs field. Since neutrinos are much lighter than their leptonic partners, the coupling strength of the neutrino field to the Higgs field has to be much smaller than that of the electron:

$$g_\nu \ll g_e. \tag{1.14}$$

After introducing the Dirac mass term the question arises why neutrinos couple to the Higgs field so weakly compared to their leptonic partners. And since an insertion of the Dirac matrix γ^5 yields

$$\bar{\nu}\nu = \bar{\nu}\left(\frac{1+\gamma^5}{2}+\frac{1-\gamma^5}{2}\right)\left(\frac{1+\gamma^5}{2}+\frac{1-\gamma^5}{2}\right)\nu = \overline{\nu_L}\nu_R + \overline{\nu_R}\nu_L, \tag{1.15}$$

a right-handed partner of the left-handed neutrino and a left-handed partner of the right-handed anti-neutrino must be introduced in order to prevent $m_D\bar{\nu}\nu$ to vanish.

1.3.2 Majorana mass terms

Theoretically, $\overline{\psi^c}\psi^c, \bar{\psi}\psi^c$ and $\overline{\psi^c}\psi$ are also possible mass terms, where ψ^c is the charge conjugate of the fermion field ψ. $\overline{\psi^c}\psi^c$ is equivalent to $\bar{\psi}\psi$. $\bar{\psi}\psi^c$ and $\overline{\psi^c}\psi$ cannot be mass terms for electrons or quarks because they destroy or create two particles of equal electric charge. However, they can be used as mass terms for neutrinos, because neutrinos do not have electric charge. These mass terms destroy or create two particles of the same lepton number, hence violate lepton number conservation and are called Majorana mass terms:

$$-\mathcal{L}_\nu^M \equiv \frac{1}{2}m_L\left(\overline{\nu_L}(\nu_L)^c + \overline{(\nu_L)^c}\nu_L\right) + \frac{1}{2}m_R\left(\overline{(\nu_R)^c}\nu_R + \overline{\nu_R}(\nu_R)^c\right), \tag{1.16}$$

where m_L and m_R are two independent constants.

1.3.3 Generic mass terms

Nature could reflect a combination of the Dirac and Majorana mass terms:

$$\begin{aligned}
-2\mathcal{L}_\nu^{D+M} &\equiv -2\mathcal{L}_\nu^D - 2\mathcal{L}_\nu^M \\
&= (m_D\bar{\nu}\nu + m_D\overline{\nu^c}\nu^c) \\
&+ (m_L\overline{\nu_L}(\nu_L)^c + m_L\overline{(\nu_L)^c}\nu_L + m_R\overline{(\nu_R)^c}\nu_R + m_R\overline{\nu_R}(\nu_R)^c) \\
&= m_D\overline{\nu_L}\nu_R + m_D\overline{(\nu_R)^c}(\nu_L)^c + m_L\overline{\nu_L}(\nu_L)^c + m_R\overline{(\nu_R)^c}\nu_R + h.c.,
\end{aligned} \tag{1.17}$$

where $h.c.$ stands for Hermitian conjugate. Introducing the notation $\nu^c_{L,R} \equiv (\nu^c)_{L,R} = (\nu_{R,L})^c$ eq. 1.17 can be written as

$$-2\mathcal{L}_\nu^{D+M} = \left(\overline{\nu_L}, \overline{\nu_L^c}\right)\begin{pmatrix} m_L & m_D \\ m_D & m_R \end{pmatrix}\begin{pmatrix} \nu_R^c \\ \nu_R \end{pmatrix} + h.c. \tag{1.18}$$

By choosing a orthogonal matrix $\mathcal{U}$ ($\mathcal{U}^T\mathcal{U} = 1$) such,

$$\mathcal{U}^T\begin{pmatrix} m_L & m_D \\ m_D & m_R \end{pmatrix}\mathcal{U} = \begin{pmatrix} \epsilon_1 m_1 & 0 \\ 0 & \epsilon_2 m_2 \end{pmatrix}, \tag{1.19}$$

where $m_1, m_2 > 0$, $\epsilon_{1,2} = \pm 1$, and defining

$$(\nu_{1L}, \nu_{2L}) = \left(\overline{\nu}_L, \overline{\nu_L^c}\right)\mathcal{U}, \quad \begin{pmatrix} \nu_{1R}^c \\ \nu_{2R}^c \end{pmatrix} = \mathcal{U}^T\begin{pmatrix} \nu_R^c \\ \nu_R \end{pmatrix}, \tag{1.20}$$

eq. 1.18 can be rewritten as

$$\mathcal{L}_\nu^{D+M} = m_1\overline{\nu_{1L}}\nu_{1R}^c + m_1\overline{\nu_{1R}^c}\nu_{1L} + m_2\overline{\nu_{2L}}\nu_{2R}^c + m_2\overline{\nu_{2R}^c}\nu_{2L}. \tag{1.21}$$

With

$$\phi_1 = \nu_{1L} + \epsilon_1\nu_{1R}^c \quad \text{and} \quad \phi_2 = \nu_{2L} + \epsilon_2\nu_{2R}^c \tag{1.22}$$

eq. 1.18 reduces to

$$-2\mathcal{L}_\nu^{D+M} = m_1\bar{\phi}_1\phi_1 + m_2\bar{\phi}_2\phi_2. \tag{1.23}$$

Obviously,

$$\phi_k^c = (\nu_{kL})^c + \epsilon_k(\nu_{kR}^c)^c = \epsilon_k\phi_k, \quad (k = 1, 2) \tag{1.24}$$

i.e. ϕ is its own anti-particle, and hence of Majorana type.

If $m_R \gg \mathcal{O}(m_e), m_L = 0$ and $m_D \approx \mathcal{O}(m_e)$,

$$m_1 = \frac{m_D^2}{m_R} \ll m_D \quad \text{and} \quad m_2 = m_R(1 + \frac{m_D^2}{m_R^2}) \approx m_R \gg m_D. \tag{1.25}$$

Thus, if there exists a very heavy Majorana state ϕ_2, the other state ϕ_1 would be much lighter than m_e. This is the so-called seesaw mechanism.

In summary, both Dirac and Majorana mass terms should be taken into account. For fermions carrying charge or similar quantum numbers Majorana mass terms are forbidden. This is not the case for neutrinos. Majorana neutrinos ϕ_1, ϕ_2 can be constructed out of combinations of Dirac and Majorana fields. Using the seesaw mechanism the tiny neutrino masses can be explained naturally.

1.4 Probing neutrino masses

Current neutrino oscillation experiments cannot address either problem, the absolute mass scale and the mass hierarchy. Three major methods to address the questions are:

Cosmological observations which are sensitive to the sum of all neutrino masses Σ,

Single beta decay experiments which are sensitive to the effective electron neutrino mass m_β,

Neutrinoless double beta decay experiments which are sensitive to the effective Majorana neutrino mass $m_{\beta\beta}$.

1.4.1 Cosmological observations

According to the standard model of cosmology neutrinos affect the evolution of the universe in three aspects. First, the number of neutrino flavors, N_ν, affects the abundances of light elements in the early universe which are reflected in the cosmic microwave background (CMB). Using current CMB data, the value of N_ν is determined to be $1.8 \sim 3.3$ [53]. Secondly, if our universe is flat, the energy density of the universe $\Omega = \Omega_\Lambda + \Omega_{cd} + \Omega_b + \Omega_\nu = 1$, where $\Omega_\Lambda, \Omega_{cd}, \Omega_b$ and Ω_ν indicate the contribution to the energy density from dark energy, cold dark matter, baryons and neutrinos, respectively. If neutrinos have substantial mass, the percentages of the other components of the universe change as does the evolution of the universe. This would be reflected in the CMB data. Finally, the large-scale structures (LSS) existing today evolved from small initial density fluctuations. Relativistic neutrinos, as weakly interacting particles, could escape without interaction from areas of high density to areas of low density (free streaming); hence, could wash out the fluctuations. The larger the neutrino masses, the stronger is the effect. The data on anisotropies in LSS thus gives access to neutrino masses.

Cosmological observations are only sensitive to the sum of the neutrino masses

$$\Sigma \equiv \sum_i m_i. \tag{1.26}$$

They are not sensitive to the oscillation parameters and cannot distinguish between Dirac and Majorana neutrinos. However, the limit on the sum of neutrino masses from cosmology does help to answer the questions left by the oscillation experiments. Fig. 1.2, taken from Ref. [54], shows the allowed range of the sum of the neutrino masses as a function of the lightest neutrino mass. The regions noted with $\Delta m^2_{32} < 0$ and $\Delta m^2_{32} > 0$ are the allowed regions in case of inverted and normal hierarchy, respectively. If the limit was as low as ~ 0.08 eV, the normal and inverted hierarchy could be distinguished. Considering only the CMB data, the 2σ (95% CL) constraint on the sum of neutrino masses is 1.19 eV. Taking into account LSS the constraint could go down to the sub eV level [55]. Several calculations show that the Planck satellite, which is going to be launched soon, can set a limit at the $0.07 \sim 0.25$ eV level [56].

Additional information could come from supernova neutrinos. They arrive slightly later than γ-rays from the same source due to their finite mass.

1.4.2 Single beta decay

Single beta decay experiments probe the effective electron neutrino mass, m_β, by precisely measuring the shape of the beta decay spectrum around its end point. With the terminology of Eq. 1.10 m_β is defined as

$$m_\beta \equiv \sqrt{\sum_{i=1} m_i^2 |U_{ei}|^2}. \tag{1.27}$$

The Dirac or Majorana nature of the neutrino cannot be inferred from m_β because the phases in the PMNS matrix do not contribute to the absolute values of the U_{ei}. The MAINZ [57] and TROITSK [58] experiments measured m_β in tritium decay. The combined limit is $m_\beta < 2.0$ eV at 99% CL. The sensitivity targeted by the future experiments KATRIN [59], also based on tritium decay, and MARE [60], based on ^{187}Re decay, is ~ 0.2 eV. Fig. 1.3, taken from Ref. [54], shows the allowed range of the effective electron neutrino mass m_β as a function of the lightest neutrino mass. The regions noted with

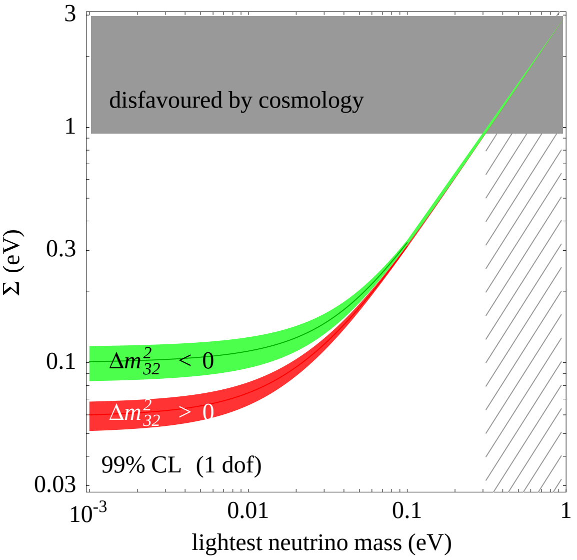

Figure 1.2: Allowed range of the sum of the neutrino masses Σ as a function of the lightest neutrino mass (taken from Ref. [54]). The regions noted with $\Delta m^2_{32} < 0$ and $\Delta m^2_{32} > 0$ are the allowed regions at 99% confidence level (CL) in case of inverted and normal hierarchy, respectively. The darker lines in the middle of the regions correspond to the central values of the oscillation parameters. The hatched area indicates the region of the lightest neutrino mass disfavoured by cosmology.

$\Delta m^2_{32} < 0$ and $\Delta m^2_{32} > 0$ are the allowed regions in case of inverted and normal hierarchy, respectively. Obviously, the sensitivities of KATRIN and MARE are not good enough to resolve the hierarchy problem.

1.4.3 Neutrinoless double beta decay

Due to the pairing interaction even-even nuclei are more bound than the odd-odd ones. Take $^{76}_{32}$Ge as an example. It is an even-even nucleus and cannot decay into its nearest neighbor even-odd nucleus $^{76}_{33}$As due to energy conservation. It can, however, decay into the next to nearest neighbor $^{76}_{34}$Se by emitting two electrons (double beta decay) as shown in Fig. 1.4. If neutrinos are of Dirac type, two neutrinos also have to be emitted in the double beta decay ($2\nu\beta\beta$). If neutrinos have masses and of Majorana type, the neutrino emitted in one beta decay could be absorbed in another and a decay without neutrino emission would become possible. This is the so-called neutrinoless double beta decay ($0\nu\beta\beta$). These two types of double beta decays are denoted:

$$2\nu\beta\beta : (Z, A) \rightarrow (Z + 2, A) + 2e^- + 2\bar{\nu}_e, \tag{1.28}$$

$$0\nu\beta\beta : (Z, A) \rightarrow (Z + 2, A) + 2e^-, \tag{1.29}$$

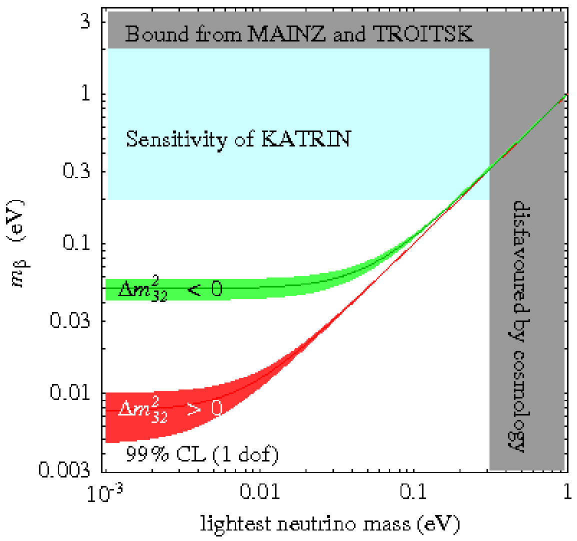

Figure 1.3: Allowed range of the effective electron neutrino mass m_β as a function of the lightest neutrino mass (taken from Ref. [54]). The regions noted with $\Delta m^2_{32} < 0$ and $\Delta m^2_{32} > 0$ are the allowed regions at 99% confidence level (CL) in case of inverted and normal hierarchy, respectively. The darker lines in the middle of the regions correspond to the central values of the oscillation parameters. The area as excluded by cosmology and previous single beta decay experiment are shown in dark. The area over which KATRIN is sensitive is shown in grey (cyan online).

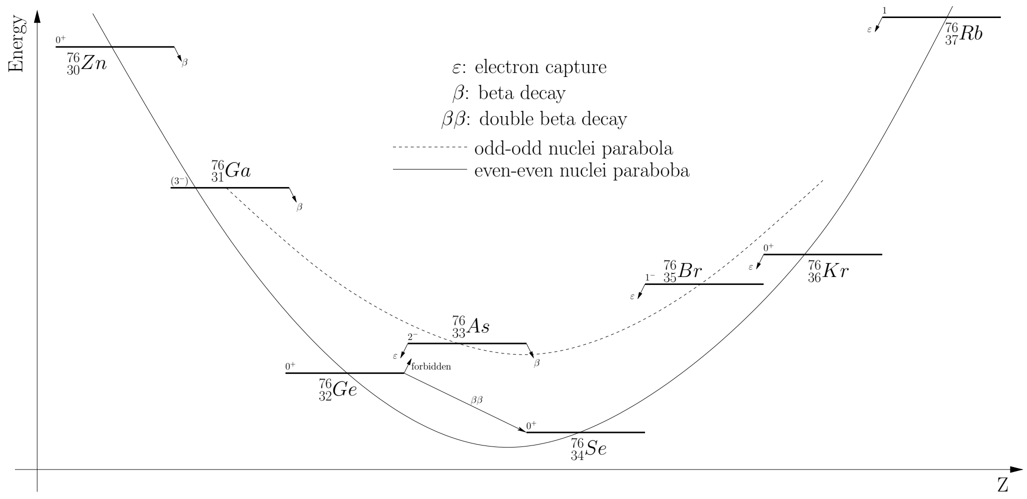

Figure 1.4: Decay sequence of nuclei with $A = 76$. Even-even nuclei (chained with solid parabola) are more bound than the odd-odd nuclei (chained with dashed parabola). The single beta decay from $^{76}_{32}$Ge to $^{76}_{33}$As is forbidden due to the energy conservation.

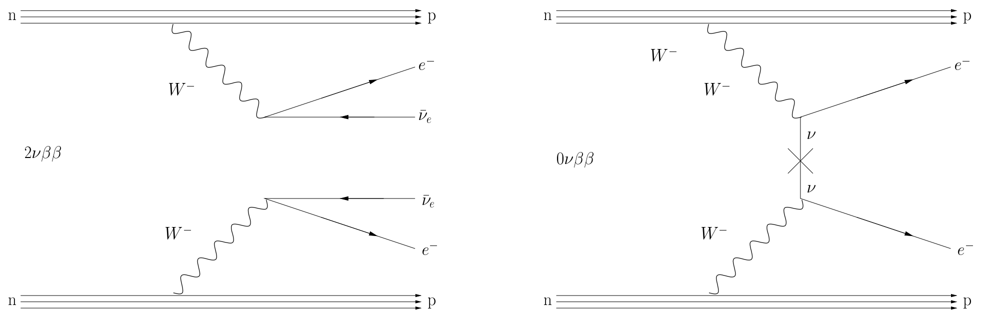

Figure 1.5: Feynman diagrams of double beta decay with and without two neutrinos being emitted.

where Z is the charge of the nucleus and A is the atomic number. The Feynman diagrams of both processes are shown in Fig. 1.5.

According to Fermi's golden rule the rates of these two types of double beta decays are

$$1/T^{2\nu}_{1/2} = G_{2\nu}(Q, Z)|\mathcal{M}_{2\nu}|^2, \tag{1.30}$$

$$1/T^{0\nu}_{1/2} = G_{0\nu}(Q, Z)|\mathcal{M}_{0\nu}|^2 m^2_{\beta\beta}, \tag{1.31}$$

where the phase space factors $G_{2\nu}(Q, Z)$ and $G_{0\nu}(Q, Z)$ depend on the Q-value and the nuclear charge Z; the nuclear matrix elements $\mathcal{M}_{2\nu}$ and $\mathcal{M}_{0\nu}$ describe the hadronic part of the decays; and the effective Majorana neutrino mass $m_{\beta\beta}$ can be expressed as

$$m_{\beta\beta} \equiv \left|\sum_k m_k U^2_{ek}\right| = \left|m_1|U_{e1}|^2 + m_2|U_{e2}|^2 e^{i(\alpha_2-\alpha_1)} + m_3|U_{e3}|^2 e^{-i(\alpha_1+2\delta)}\right|, \tag{1.32}$$

assuming only the exchange of three light neutrinos.

Figure 1.6, taken from Ref. [54], shows the allowed range of the effective Majorana neutrino mass $m_{\beta\beta}$ as a function of the lightest neutrino mass. The regions marked $\Delta m^2_{32} < 0$ and $\Delta m^2_{32} > 0$ are the allowed regions in case of inverted and normal hierarchy, respectively. The effective Majorana neutrino mass $m_{\beta\beta}$ could be invisibly small in case of a normal hierarchy, because the terms in Eq. 1.32 can cancel if the CP-violation phases α_1, α_2 and δ take special values. An experiment sensitive to $m_{\beta\beta} \sim 10$ meV would have an excellent chance to see a signal in case of an inverted mass hierarchy. And if the observed $m_{\beta\beta}$ is far below 10 meV, the inverted mass hierarchy can be ruled out. Currently the best constraint on $m_{\beta\beta}$ was given by the CUORICINO collaboration [61]. They gave an upper limit (90% CL) on $m_{\beta\beta}$ between 0.19 and 0.68 eV when analyzed with the many published nuclear structure calculations. There is also a claim from part of the Heidelberg-Moscow (HdM in short) collaboration that $m_{\beta\beta} = 0.2 \sim 0.6$ eV (99% CL) [62].

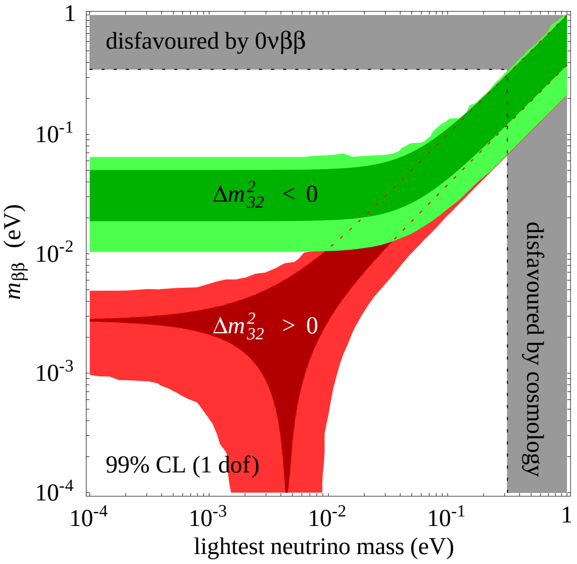

Figure 1.6: Allowed range of the effective Majorana neutrino mass $m_{\beta\beta}$ as function of the lightest neutrino mass (taken from Ref. [54]). The regions noted with $\Delta m^2_{32} < 0$ and $\Delta m^2_{32} > 0$ are the allowed regions at 99% confidence level (CL) in case of inverted and normal hierarchy, respectively. The inner/outer bands correspond to calculations without/with the 3σ-uncertainties on the oscillation parameters.

1.4.4 Combined analysis

The constraints on the neutrino mass from cosmological observations, single beta decay and $0\nu\beta\beta$ decay experiments cannot be compared directly because they refer to different observables, Σ, m_β and $m_{\beta\beta}$. However, all being functions of the neutrino masses and oscillation parameters, they can be used in a combined analysis.

Figure 1.7, taken from Ref. [63], shows regions allowed at 2σ by neutrino oscillation data, in each of the three coordinate planes of the parameter space $(\Sigma, m_\beta, m_{\beta\beta})$, for both normal and inverted hierarchy. The most "aggressive" cosmological constraint (labeled as 7 in the top left plot of Fig. 1.7) already conflicts with the HdM claim on $m_{\beta\beta}$. And the planned sensitivity of KATRIN can confirm or refute the HdM claim.

1.4.5 Other approaches

The effective muon neutrino mass can be obtained from the pion decay $\pi \rightarrow \mu\nu_\mu$. Since the masses of the pion m_π and the muon m_μ are known, the muon neutrino mass can be calculated as $m_{\nu_\mu} = m^2_\pi + m^2_\mu - 2m_\pi(p^2_\mu + m^2_\mu)^{1/2}$, where p_μ is the muon momentum. The difficulty is to precisely measure p_μ. Currently the best limit is $m_{\nu_\mu} < 170$ keV (90% CL) [64]. New experiments like NuMass aim at a sensitivity of ~ 8 keV [65], which is not competitive with the approaches mentioned before.

It is also possible to measure the absolute neutrino masses by studying neutrino pair

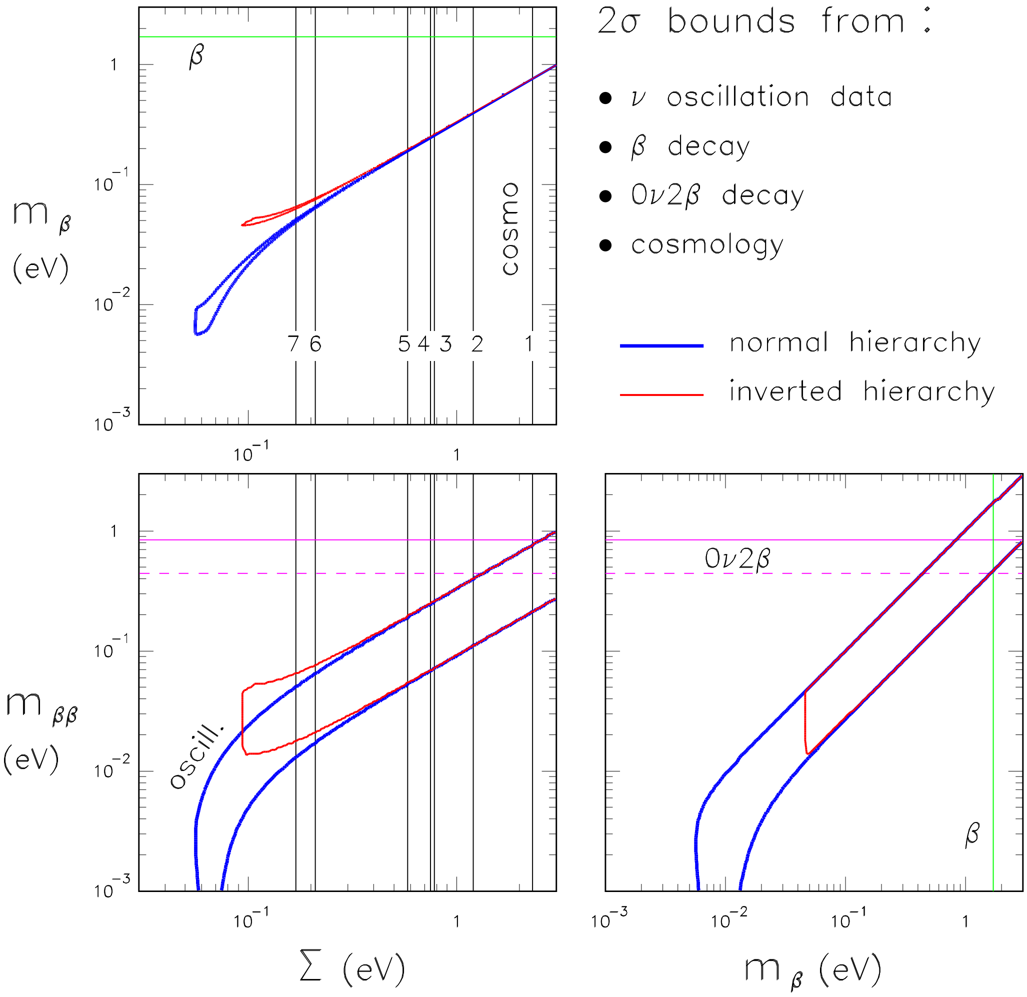

Figure 1.7: Regions allowed at 2σ by neutrino oscillation data, in each of the three coordinate planes of the parameter space $(\Sigma, m_\beta, m_{\beta\beta})$, for both normal and inverted hierarchy. Cosmological constraints are labeled with numbers corresponding to different data sets and models from the most conservative one (1) to the most "aggressive" one (7). The plot is taken from Ref. [63].

emission from meta-stable excited atoms [66]. The emission rate scales with the fifth power of the neutrino mass; hence is very small. Novel mechanisms which could largely enhance the rate are needed. The rate also depends on the nature of neutrinos; hence could be used to distinguish between Dirac and Majorana neutrinos.

In the Standard Model extended to include Dirac neutrino masses (see Sec. 1.3.1) the neutrino magnetic moment μ_ν is proportional to the neutrino mass: $\mu_\nu = 3.2 \times 10^{-19}(m_\nu/\mathrm{eV})\mu_B$ [67], where μ_B is the Bohr magneton. It is unobservably small given the known upper bounds on neutrino masses. For Majorana neutrinos only transition moments are allowed. The transition moment could convert left-handed neutrinos to right-handed anti-neutrinos of a different flavor. The interaction of the transition moment with the solar magnetic field was used to explain the solar neutrino deficit by Lim and Marciano [68] and by Akhmedov [69] (LMA). The expected magnitude of the transition moment is $\sim 10^{-11}\mu_B$. The current best limit, $2 \times 10^{-10}\mu_B$, comes from a combined analysis of solar and reactor data [70].

Chapter 2

Neutrinoless double beta decay experiments

Neutrinoless double beta decay is an extremely rare process even if it does exist. Requirements, which are crucial to increase the sensitivity of $0\nu\beta\beta$ decay experiments, are summarized. The "Pros and Cons" of different experimental approaches are discussed based on these requirements.

2.1 Sensitivity

The number of observed $0\nu\beta\beta$ decay events N_s within the measuring time t, can be calculated as

$$N_s = M \cdot \kappa \cdot \frac{N_A}{M_A} \cdot \epsilon \cdot (1 - e^{-t/\tau}) \approx M \cdot \kappa \cdot \frac{N_A}{M_A} \cdot \epsilon \cdot \frac{t}{\tau}, \tag{2.1}$$

where, M is the total mass of the source material, κ is the mass fraction of the isotope under study, N_A is Advogadro's number, M_A is the atomic mass of the isotope, ϵ is the signal detecting efficiency, and τ is the mean lifetime of the decay. Since the measuring time t is much shorter than the mean lifetime τ, $(1 - e^{-t/\tau})$ is approximated as t/τ. The half lifetime, $T^{0\nu}_{1/2}$, is then

$$T^{0\nu}_{1/2} = \ln 2 \cdot \tau \approx \ln 2 \cdot M \cdot \kappa \cdot \frac{N_A}{M_A} \cdot \epsilon \cdot \frac{t}{N_s}. \tag{2.2}$$

The number of background events within the measuring time t and within the energy window of interest ΔE is

$$N_b = b \cdot M \cdot t \cdot \Delta E, \tag{2.3}$$

where b is the background index given in per kilogram of source material per measuring year and per keV. If N_s is smaller than the standard fluctuation expected for N_b, *i.e.*,

$N_s < \sqrt{N_b}$[1], the signal cannot be extracted. In this case the relation

$$T_{1/2}^{0\nu} > \ln 2 \cdot M \cdot \kappa \cdot \frac{N_A}{M_A} \cdot \epsilon \cdot \frac{t}{\sqrt{N_b}} = \ln 2 \cdot \kappa \cdot \frac{N_A}{M_A} \cdot \epsilon \sqrt{\frac{Mt}{b\Delta E}} \tag{2.4}$$

can be used to set a lower limit on the half lifetime. Combined with Eq. 1.31, the following relation can be deduced to set an upper limit on the effective Majorana neutrino mass:

$$m_{\beta\beta} < \sqrt{\frac{M_A}{\ln 2 \cdot \kappa \cdot N_A \cdot \epsilon}} \sqrt{\frac{1}{G_{0\nu}(Q,Z)}} \frac{1}{|\mathcal{M}_{0\nu}|} (\frac{b\Delta E}{Mt})^{1/4} \tag{2.5}$$

The sensitivity of a $0\nu\beta\beta$ decay experiment in terms of lifetime or neutrino mass can be estimated based on Eq. 2.4 or 2.5, respectively.

2.2 Experimental approaches

2.2.1 General considerations

An analysis of Eq. 2.5 provides guidance on how to design a $0\nu\beta\beta$ decay experiment with a good sensitivity. As many of the following requirements should be met:

- the mass of the source material M should be large;
- the abundance of the isotope under study should be high, either naturally or by enrichment;
- the calculation of the nuclear matrix element $|\mathcal{M}_{0\nu}|$ for this isotope should be accurate;
- the Q-value should be large, because $G_{0\nu}(Q,Z) \propto Q^5$, and the higher the Q-value, the fewer lines from natural radioactivity produce background;
- the signal detecting efficiency should be large;
- the energy resolution should be good in order to allow a small ΔE;
- last but not the least, the background level b should be as low as possible.

And then patience is needed; data is generally collected over many years.

Except for background suppression techniques, the experimental approaches are mainly determined by the choice of the source material. Table 2.1 presents a selection of isotopes used or planned to be used to search for $0\nu\beta\beta$ decay. Also listed are their Q-values, nuclear matrix elements [72, 73, 74, 75], natural abundance κ_0 and properties important for the experimental design. Different experimental approaches can be classified into two categories: 1. the source material can be used to produce the detector; 2. the source is not the detector, the decay products need to be detected using equipment around the source.

---

[1] The standard fluctuation expected for N_b can be expressed as $\sqrt{N_b}$ only if $N_b \gtrsim 10$. A detailed study of the sensitivity with small N_b can be found in Ref. [71]

Table 2.1: A selection of possible source candidates for $0\nu\beta\beta$ decay experiments. Also listed are their Q-values, nuclear matrix elements, natural abundance κ_0 and properties important for the design of experiments.

Isotope	Q [MeV]	$\mathcal{M}_{0\nu}$	κ_0 [%]	Properties
^{48}Ca	4.271	0.67^a	0.19	CaF_2 & $CaWO_4$ is a scintillator
^{76}Ge	2.039	4.51 ± 0.17	7.8	semiconductor
^{82}Se	2.995	4.02 ± 0.15	9.2	-
^{96}Zr	3.350	1.12 ± 0.03	2.8	-
^{100}Mo	3.034	3.34 ± 0.19	9.6	-
^{116}Cd	2.809	2.74 ± 0.19	7.5	CdZnTe^b is a semiconductor; $CdWO_4$ is a scintillator
^{124}Sn	2.287	2.11^a	5.8	semiconductor
^{130}Te	2.530	3.26 ± 0.12	35	TeO_2 can be used as bolometer
^{136}Xe	2.480	2.11 ± 0.11	8.9	active material for time projection chambers
^{150}Nd	3.367	4.74 ± 0.20	5.6	could be dissolved in liquid scintillator

---

[a] The values are from an ISM (Interacting Shell Model) calculation in Ref [75]. The other $\mathcal{M}_{0\nu}$ values with errors are from QRPA (Quasi-particle Random Phase Approximation) calculations [73]. The errors are from the measurement of $2\nu\beta\beta$ experiments.

[b] There are other isotopes in the CdZnTe crystal that could undergo $0\nu\beta\beta$ decay. The rest of them are ^{70}Zn with $Q = 1.001$ MeV, $\kappa_0 = 0.62\%$, ^{114}Cd with $Q = 0.534$ MeV, $\kappa_0 = 28.7\%$, ^{128}Te with $Q = 0.868$ MeV, $\kappa_0 = 31.7\%$ and ^{130}Te.

2.2.2 Source and detector are identical

As shown in Table 2.1, quite a few $0\nu\beta\beta$ decay candidates have special properties which allow them to be used as detectors. There are advantages to this concept. As the decay electrons do not have to leave the source and reach the detector, the detection efficiency is not limited and the energy resolution of the detector not deteriorated. As a consequence large compact masses are useable limiting the loss of events close to a surface with electrons escaping. The drawback is that such detectors usually have limited capability to reconstruct event topologies and normally only one isotope can be studied.

^{48}Ca has the highest Q-value among all the candidates. Hence low background from natural radioactivities is expected. It also means a large phase space factor which enlarges the $0\nu\beta\beta$ decay rate for a given Majorana mass. However, until now only few experiments have been carried out because of its low natural abundance. The most stringent limit on the $0\nu\beta\beta$ decay of ^{48}Ca came from ELEGANT VI [76] using CaF_2 scintillator. Two future experiments using CaF_2 and $CaWO_4$ as scintillator, respectively, are CANDLES [77] and CARVEL [78]. They aim at a sensitivity in $m_{\beta\beta} <$ (0.04-0.09) eV.

The search for the $0\nu\beta\beta$ decay of ^{76}Ge is affected by natural radioactivity due to its low Q-value. Enrichment in ^{76}Ge is also needed in order to overcome the low natural abundance. However, semiconductor detectors made from high purity germanium crystals have been used as gamma spectrometers for years and have an excellent energy resolution. Previous ^{76}Ge $0\nu\beta\beta$ decay experiments include IGEX [79] and HdM [62]. GERDA [2]

Phase I is currently under construction and will be described in detail in the next chapter. The planned future experiments include GERDA Phase II and Majorana [80, 81]. The GERDA and Majorana Collaborations have reached an agreement to share resources and knowledge where appropriate in their parallel development of the two different detector designs. The ultimate goal is to combine the strength of the two collaborations in a future experiment that will employ the best technology for reaching a Majorana neutrino mass sensitivity of below 0.05 eV.

The Cobra experiment [82,83,84] is a special case in the "source = detector" concept. A large array of CdZnTe semiconductor detectors is going to be used. The CdZnTe crystal contains 5 isotopes which could undergo $0\nu\beta\beta$ decay. Pixellated CdZnTe detectors can be operated as solid-state time projection chambers (TPC) and hence offer tracking capability which allows reconstruction of the event topology. Another advantage of CdZnTe detectors is that they can be operated at room temperature. No large and complicated cooling facility is needed. However, the energy resolution of CdZnTe detectors currently available is not as good as those of germanium detector and TeO_2 bolometers.

The tungstate $CdWO_4$ is similar to $CaWO_4$, and can be used as scintillator. A comprehensive comparison between them can be found on page 27 of Ref. [85]. The $CdWO_4$ crystal is less contaminated and has better background/signal discrimination power than the $CaWO_4$ crystal. Previous $0\nu\beta\beta$ decay experiments using $CdWO_4$ scintillators include the one performed by the Kiev-Florence collaboration in the Solotvina Underground Laboratory since 1989 [86, 87] and CAMEO [88, 89]. The CAMEO project also proposes to exploit 1 ton of $^{116}CdWO_4$ detectors placed in one of the large underground neutrino detectors such as BOREXINO [90], SNO or KamLAND. The sensitivity is estimated to be $m_{\beta\beta} < 0.02$ eV.

CUORICINO [91], the pilot experiment for CUORE [92,93], just released a new upper limit of $m_{\beta\beta}$ [94] using TeO_2 bolometers. TeO_2 bolometers have almost the same energy resolution as the germanium detector. ^{130}Te has the highest natural abundance among all the $0\nu\beta\beta$ decay candidates. CUORE is also trying to use $CdWO_4$ as scintillating bolometer [95]. The scintillating bolometer could provide more parameters helping background rejection, especially from surface contamination. One of the challenges of CUORE is to stabilize the contact between the bolometer and the thermometer.

Both gaseous and liquid xenon can be used as active material in a TPC, the later can also be used as a scintillator. The XMASS experiment [98], currently under construction in the Kamioka Observatory, is going to use liquid xenon as a scintillator. The position of a interaction can be extracted from the hit pattern of the PMTs around the scintillator. The EXO experiment [97], also under construction currently, is going to use TPC filled with liquid xenon which can be used as scintillator at the same time. The position of a interaction can be inferred from the time difference of the scintillation light signal and the ionization signal. In gaseous xenon it is possible to reconstruct the tracks of the electrons from the beta decay. This makes it easy to discriminate against background induced by natural radioactivity. An experiment was carried out in the Gotthard underground laboratory using TPC filled with xenon gas enriched to 62.5 % in ^{136}Xe at a pressure of 5 bar [96].

^{150}Nd has the second highest Q-value, the largest nuclear matrix element $\mathcal{M}_{0\nu}$ (though the uncertainty is large) and a relatively high natural abundance (enrichment is possible) among all the $0\nu\beta\beta$ decay candidates. In a follow-up experiment to SNO, called SNO+ [99], the old SNO infrastructure will be filled with Nd-loaded liquid scintillator instead of D_2O. Although the energy resolution of the detector will not be as good as that of other existing experiments, the mass that could be suspended in the scintillator is large (0.1% load of enriched Nd corresponds to about 500 kg of ^{150}Nd). This may give SNO+ the sensitivity of $m_{\beta\beta}$ as low as 0.03 eV.

2.2.3 Source and detector are not identical

The advantages of using external detectors are (1) the source material could be changed so that several $0\nu\beta\beta$ decay candidates could be investigated in the same experiment; (2) using tracking devices the event topology could be reconstructed which leads to excellent background discrimination. The disadvantages are (1) normally the energy resolution is not good; (2) in order to release the beta decay electrons, the source has to be made into thin foils and hence large masses are difficult to integrate in an experiment.

The previous experiments include TGV I and II [100,101,102], NEMO I [103], II [104] and III [105, 106]. In TGV Cd plates were put in between germanium spectrometers. In NEMO the source foils (Ca, Se, Zr, Cd, Mo, Te and Nd) were fixed between two tracking volumes composed of many drift cells. The planned future experiments include SuperNEMO [107], MOON [108] and DCBA [109]. Based on the NEMO III experience, SuperNEMO aims at the sensitivity of $m_{\beta\beta} \sim 0.03$ eV. In MOON, enriched ^{100}Mo foils will be interleaved with plastic scintillators which work as a calorimeter as well as an active shield. The designed sensitivity of MOON is $m_{\beta\beta} \sim 0.03$ eV. In DCBA thin source plates (^{150}Nd,^{100}Mo ^{82}Se) will be installed in tracking chambers located in a uniform magnetic field. DCBA is an R&D project for MTD (Magnetic Tracking Detector), the design sensitivity of which is $m_{\beta\beta} \sim$ 0.02-0.07 eV [111].

2.2.4 Summary

Table 2.2 summarizes the proposed $0\nu\beta\beta$ decay experiments mentioned in the previous discussion. The schedule is not clear in most cases. However, the table provides a quick reference concerning the experimental aspects of $0\nu\beta\beta$ decay research.

Table 2.2: Characteristics of proposed $0\nu\beta\beta$ experiments. The corresponding references are: CARVEL [78], CANDLES [77], GERDA [2,71], Majorana [81], Cobra [84], CAMEO [89], CUORE [93], XMASS [110], EXO [97], SNO+ [99], MOON [108], SuperNEMO [107], DCBA/MTD [111]

Experiment	Technique	Sensitivity[a] ($m_{\beta\beta}$/eV)	Schedule
CARVEL	$CaWO_4$ scintillator	0.04-0.09	-
CANDLES	CaF_2 scintillator	-	-
GERDA Phase I	Ge detector in LAr[b]	0.27	2009
GERDA Phase II	Ge detector in LAr	0.11	-
Majorana	^{76}Ge detector	0.03-0.04	-
Cobra	CdZnTe semiconductor	< 1	-
CAMEO	$CdWO_4$ scintillator	< 0.02	-
CUORE	TeO_2 bolometer	< 0.03	-
XMASS	liquid Xe TPC	0.06-0.09	-
EXO	liquid Xe TPC with laser tagging	< 0.01	-
SNO+	Nd-load scintillator	< 0.05	2010
MOON	Mo foil interleaved with scintillators	~ 0.03	-
SuperNEMO	drift chamber + calorimeter	< 0.05	2012
DCBA/MTD	source plates in drift chamber	0.02-0.07	2016

---

[a] Please refer to the references for the definition of the sensitivities for the individual experiment.

[b] liquid argon

Chapter 3

The GERDA experiment

The GERDA (GERmanium Detector Array) experiment [1,2] is designed to search for the $0\nu\beta\beta$ decay of ^{76}Ge. The physics reach will depend on the achievable background level. The main design feature is to operate "naked" germanium detectors directly in liquid argon in order to make an extremely low background level possible. The concept is based on ideas presented in Ref. [112]. The experiment is described in the first section of this chapter. GERDA is currently under construction in Hall A of the INFN Gran Sasso National Laboratory (LNGS), Italy. The current status of the experiment is given in the second section. GERDA is planned in three phases. In the first phase (Phase I) unsegmented germanium detectors, which were previously used in the IGEX [79] and HdM [62] experiments, will be re-deployed. The envisioned background level is 10^{-2} events/(kg·keV·year). In the second phase (Phase II), in addition, 18-fold segmented detectors will be used. The background level aimed at is 10^{-3} events/(kg·keV·year). A later phase (Phase III) is under discussion in cooperation with the Majorana collaboration [80, 81], aiming at a one-ton experiment. The physics observation capability of GERDA is discussed in the last section.

3.1 Background reduction techniques

Germanium detectors have been used to detect ionizing radiation, particularly X-rays and γ-rays, for decades. The energy resolution is typically better than 1% around the Q-value of the ^{76}Ge $\beta\beta$ decay. This is among the best of all detectors introduced in Sec. 2.2.1 and provides a very good separation between the $0\nu\beta\beta$ signal and the $2\nu\beta\beta$ background. However, the natural abundance of ^{76}Ge is only 7.6%. As both signal and background scale with mass, isotopic enrichment is needed to improve the signal to background ratio. In addition, the Q-value of the $0\nu\beta\beta$ decay of ^{76}Ge, 2.039 MeV, is lower than some lines prominent in natural radioactivity. Therefore the design of the experiment has to minimize the amount of radioactive elements in the vicinity of the detectors. Fig. 3.1 is an artist's view of GERDA. Each part of the experiment is introduced in the following sections and its function in reducing background is discussed.

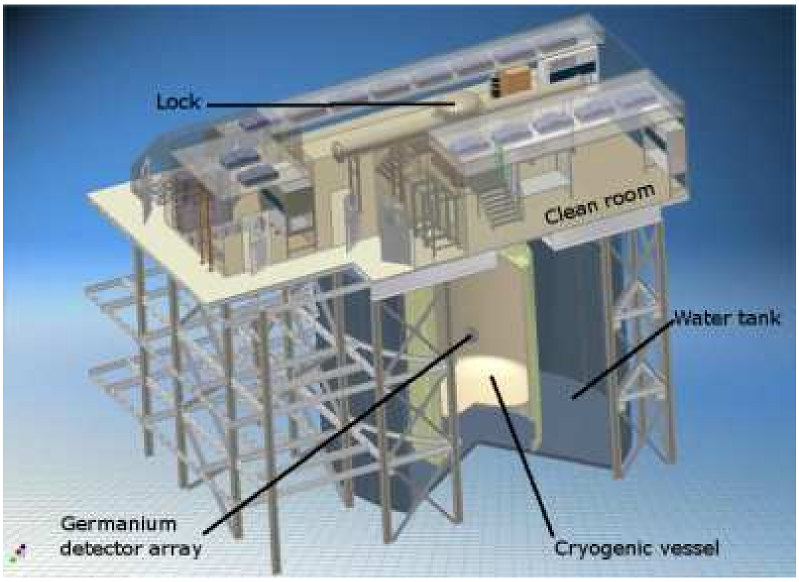

Figure 3.1: Artist view of GERDA. An array of germanium detectors is submerged in liquid argon inside a cryogenic vessel surrounded by a water tank. A lock system inside the clean room above the water tank provides access to the cryogenic volume.

3.1.1 Underground location and muon veto

To reduce the cosmic ray induced background GERDA is located underground, in Hall A of the INFN[1] Gran Sasso National Laboratory (LNGS), Italy. LNGS is the largest underground facility in the world for low-background experiments. It is accessed from the 10 km long highway tunnel under the Gran Sasso mountains. It has three experimental halls hosting a large variety of experiments, most of which focus on dark matter or neutrino physics. Fig. 3.2 shows the location of GERDA inside LNGS. The main experimental site of GERDA is between the Large Volume Detector (LVD) and the service tunnel crossing Hall A. The GERDA auxiliary and cryogenic storage system will be located in the service tunnel on the northeast side of Hall A.

The overburden of 1.4 km of rock above the experimental halls corresponds to 3400 meter of water equivalent (m.w.e). It reduces the cosmic ray induced muon (neutron) flux by a factor of 10^6 (10^3) compared to the surface. The energy and angular distributions of cosmic ray muons in Hall A of LNGS have been precisely measured [113, 114, 115]. A comprehensive study of cosmic ray induced muon and neutron background in underground laboratories can be found in Ref. [116].

In order to further reduce the muon induced background an additional muon veto system will be installed. Cosmic muons traversing the water tank (see Fig. 3.1) will cause Čerenkov radiation. To detect the radiation 66 photomultiplier tubes (PMTs) will be installed on the walls of the water tank. The positions of the PMTs are optimized

---

[1] Istituto Nazionale di Fisica Nucleare

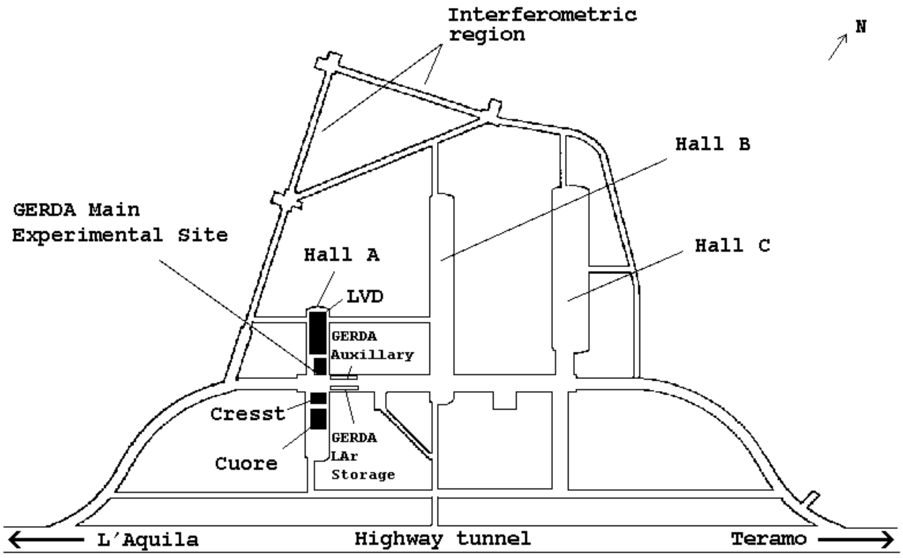

Figure 3.2: Location of GERDA inside LNGS. The main experimental site of GERDA is between the Large Volume Detector (LVD) and a service tunnel crossing Hall A. The GERDA auxiliary and cryogenic storage system will be located in the service tunnel on the northeast side of Hall A.

according to Monte Carlo simulation. The detection efficiency is about 95% depending on the incident angle of the muon. In order to compensate for the missing water around the neck of the cryostat plastic scintillator plates will be placed on top of the clean room. They will be used to detect the muons entering the cryostat almost vertically. The combined detection efficiency is expected to be above 99%.

3.1.2 Water tank and cryostat

To shield against neutron radiation from the surrounding rock about 630 m^3 of ultra-pure water will be filled in a stainless steel tank with an outer diameter of 10 m and a height of about 8 m. The stainless steel cryostat inside the water tank has an internal copper lining. The height of the vessel is 5.88 m (7.62 m with the neck) with an outer diameter of 4.16 m. It can contain 98 t of liquid argon. As liquid argon can be produced with a much greater purity than lead or even copper traditionally used for shielding, this minimizes the radioactivity close to the detector array. The liquid argon also acts as a shield against γ-rays, especially originating from the cryostat itself.

3.1.3 Detector array and electronics

The germanium detectors will be lowered into the liquid argon from the top of the cryostat. In order to minimize the radioactivity from the suspension system low mass detector holders and minimal cabling will be used (See Fig. 3.3a and 3.3b). The holders are made out of thin ultra-pure copper with a total weight of about 30 g per detector. They are chained together vertically into strings. Each string consists of up to five (most likely three) detectors of the same type as shown in Fig. 3.3c. The whole detector array could maximally consists of 16 hexagonally packed detector strings as shown in Fig. 3.3d.

The horizontal distance between the centers of two detectors is 9 cm. The vertical clearance between two detectors is about 6 cm. The Phase I detectors are p-type diodes with a cylindrical closed-ended coaxial geometry. The detectors are enriched in ^{76}Ge to a level of about 86% and have masses between 0.9 kg and 2.9 kg. Two options are under consideration for GERDA Phase II. The norminal configuration consists of 18-fold segmented n-type detectors. A second solution based on point-contact p-type detecters is also under consideration. In this thesis, we focus on the normial solution. The precise size of the detectors in this solution will depend on manufacturing details. The most likely dimensions are a height of 70 mm and a diameter of 75 mm. The detectors will be segmented 6-fold in the azimuthal angle ϕ and a 3-fold in the height z.

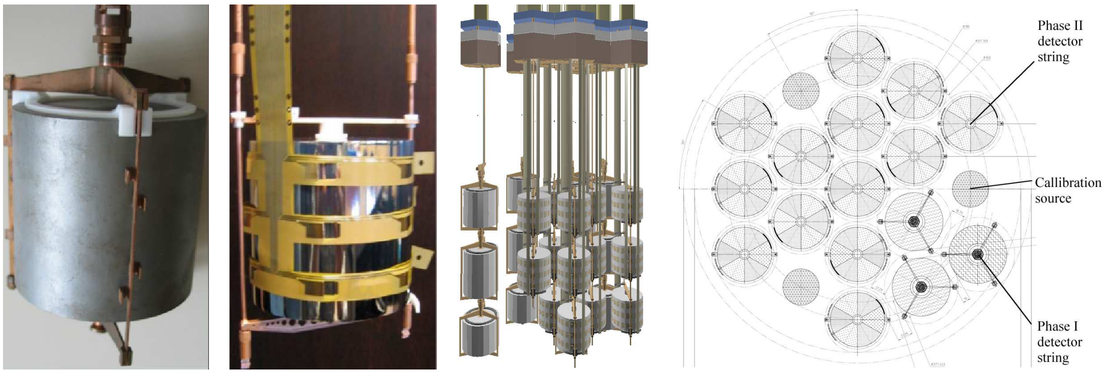

(a) (b) (c) (d)

Figure 3.3: Detector array configuration: (a) a single Phase I detector in its copper holder, (b) a single Phase II detector in its copper frame and with contact cable, (c) Phase II detector array and (d) top view of the full array indicating the possible positions for Phase I and Phase II detector strings as well as for the calibration sources.

A couple of solutions are actively pursued for the read-out electronics of GERDA [117]. A likely scheme foresees a cold FET close to the crystal followed by amplifying and load driving circuits located at room temperature. The cold FET would be placed near the connection matrix (top blocks in Fig. 3.3c), 30 cm above the detector array. Pre-amplified signals would be sent to electronics located outside the lock system at room temperature through at least 6 m long cables.

3.1.4 Detector storage and clean room

Whenever above ground, germanium detectors are exposed to cosmic radiation and radioactive isotopes are produced inside the detector through spallation caused by energetic cosmic rays. Two cosmogenic isotopes, ^{60}Co and ^{68}Ge, have Q-values above that of ^{76}Ge $0\nu\beta\beta$ decay and are potential sources of background. Therefore the time above ground needs to be minimized. Since the half life time of ^{60}Co and ^{68}Ge is 5.3 years and 271 days, respectively, a passive method to reduce the contamination is to keep the detectors long enough underground and wait for it to decay.

When exposed to air the surface a germanium detector can collect dust which contains many radioactive isotopes, particularly Pb^{214}, undergoing α decay. Some parts of the detector surface are not fully charge sensitive and only part of the energy lost by the α particle can be detected. This may result in a signal close to the Q-value of the ^{76}Ge $0\nu\beta\beta$ decay. Therefore the testing, preparation and insertion of the detector has to be done in a clean environment. For this purpose, a class 10000 clean room with radon-reduced air will be built on top of the cryostat. It houses a lock, through which detector strings are inserted into and removed from the cryogenic volume. Detector handling will be performed in flow-boxes and a detector mounting-station which will reach class 100. The lock consists of a rail system which allows to move detector strings into their correct position and lower them into the cryostat. In addition, the clean room will be used to temporarily store germanium detectors in a controlled atmosphere of gaseous argon or vacuum as shown in Fig. 3.4.

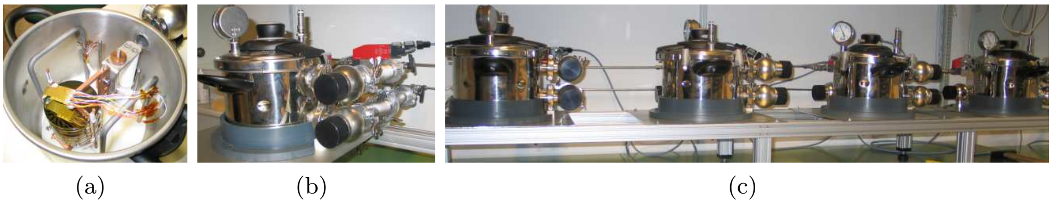
(a) (b) (c)

Figure 3.4: Detector storage system: (a) an open vacuum storage unit with a detector inside, (b) a closed vacuum storage unit equipped with valves and gas flux sensor and (c) four vacuum storage units connected by gas lines.

3.2 Background rejection methods

Even though the experimental setup is optimized to reduce the creation of potential background radiation as much as possible, there are still external photons which reach the detector array. In addition, some meta stable isotopes are created inside the detectors by cosmic muon induced neutrons. They are also potential background sources. Methods to identify and reject these remaining background events are described in this section.

3.2.1 Spatial anti-coincidence

Photons in the relevant energy range are most likely to interact via Compton scattering. Thus, they are likely to deposit energy in more than one detector (see Sec. 4.1.2). The electrons from $0\nu\beta\beta$ decay will predominantly deposit energy in only one detector. Photons can thus be identified by requiring more than one detector to see energy above the threshold. Considering the segmented detectors for Phase II photons depositing energy in only one crystal can still be identified by requiring more than one segment to show energy (see Sec. 8.2 and Ref. [118]).

3.2.2 Pulse shape analysis

Although photons are likely to create more than one energy deposition, they could all be in one segment; the anti-coincidence between segments cannot identify this kind of event. However, by analyzing the time structure of the detector response, *i.e.* pulse shape, photon induced events can still be identified [119]. The study of pulse shapes will be discussed in detail in Sec. 4.4, 4.5 and Chapters 10, 11.

3.2.3 Time anti-coincidence

Since meta stable isotopes created inside the detectors by cosmic muon induced neutrons, such as the meta stable states of ^{68}Ge and ^{77}Ge, do not decay right after the original muon event, a muon veto with a narrow time window can do very little to reject this background. This can be overcome by introducing time anti-coincidence between the original muon event and the later decays. Feasibility studies are currently carried out.

3.2.4 Instrumentation of the cryostat

Liquid argon scintillates if energy is deposited inside the argon volume. The scintillation light could be detected by PMTs mounted on the walls of the cryostat. Events with photons in the final state which deposit only a fraction of their energy inside the germanium detectors could be vetoed by requiring an anti-coincidence between the observed scintillation light and the energy deposit inside the detectors. This technique is not part of the GERDA baseline design. Feasibility studies are currently being performed [120, 121].

3.3 Status

This section closes with the status of GERDA as of Winter 2008/09. Important milestones are discussed below.

3.3.1 Cryostat and water tank

On March 6, 2008, the cryostat was delivered to LNGS and placed at the foreseen location in Hall A (see Fig. 3.5b). Mounting of the internal copper shield was completed on March 18. The cryostat underwent pressure tests, helium leak tests, liquid nitrogen evaporation tests and radon emanation measurements. The water tank installation finished at the end of June (see Fig. 3.5c). The installations of the cryostat and water tank were major milestones for GERDA.

(a) (b) (c)

Figure 3.5: Construction of cryostat and water tank at the GERDA main site: (a) empty GERDA main site, (b) cryostat and (c) water tank and some infrastructure around it.

3.3.2 Clean room and lock system

Figure 3.5c shows the first parts of the superstructure around the water tank, on top of which the clean room and lock will be built. The clean room is under construction. The design of the lock structure is almost finished. The lock will be pre-installed at the Max-Planck-Institut für Physik in Munich and then transported to the LNGS in 2009. A provisional lock system is in production. It will be used before the complete lock system is ready, so that the commissioning of GERDA can start in spring 2009.

3.3.3 Phase I and II detectors

In total 17.9 kg of enriched and 15 kg of non-enriched high-purity p-type germanium detectors from IGEX [79], HdM [62] and the Genius Test Facility (GTF) [122] will be operated in Phase I of GERDA. The tests of these p-type detectors operated in cryogenic liquids are practically completed.

A total of 37.5 kg of enriched germanium was procured for GERDA Phase II detectors. It has an enrichment level of about 90% and is stored in the HADES facility in the form of GeO_2. The purification tests with depleted germanium have shown that the yield for 6N material is about 90%, and the exposure time above ground will not exceed $2 \sim 3$ days. The resulting 6N material will be transformed into crystals by the Institut für Kristallzüchtung (IKZ) in Berlin. Crystals with a concentration of impurities down to 10^{11} per cm^3 have been pulled at IKZ, see Fig. 3.6. The Čzochralski puller was already refurbished to produce larger crystals.

The first two prototype detectors for GERDA Phase II were developed and produced in close collaboration with the manufacturer Canberra-France. They are called Siegfried I and Siegfried II. The Siegfried series are n-type true coaxial cylindrical crystals made of natural germanium with a height of 70 mm and a diameter of 75 mm with a 10 mm hole

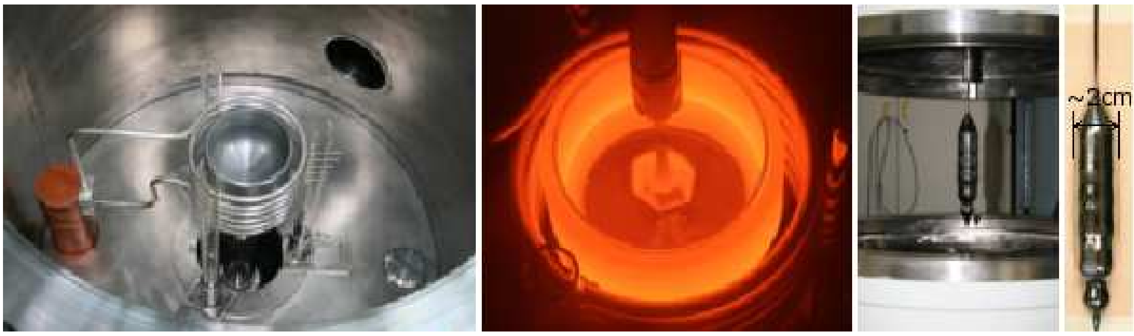

Figure 3.6: Pulling crystal in Čzochralski puller (from left to right): a Čzochralski puller, growing crystal, cooled-off crystal in open puller and a close-up of crystal.

in the center. The active volume is 302 cm^3, the total mass is 1.6 kg. They are 18-fold segmented with a 6-fold segmentation in the azimuthal angle ϕ and a 3-fold segmentation in the height z. The segmentation scheme and the detector coordinate system are depicted in Fig. 3.7 where a scheme of the cabling (left) and the segment numbering (right) are shown. The segments are read out using a Kapton flexible printed-circuit-board (FPCB) with snap-contacts [123]. Pictures of the two detectors together with the contact cables are shown in Fig. 3.8. The detector specifications as provided by Canberra-France are summarized in Table 3.1.

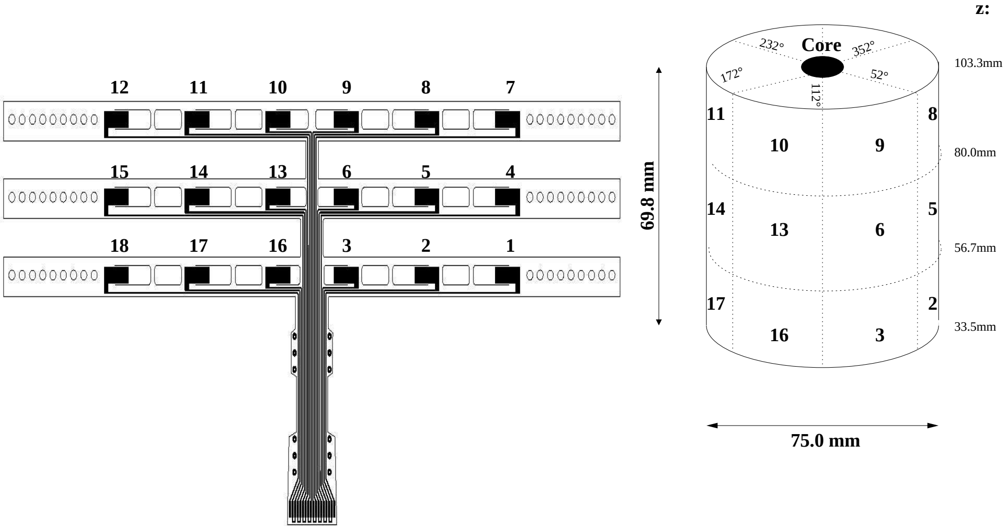

Figure 3.7: Schematic of cable (left) and segment numbering (right) of the prototype detectors.

Siegfried I was operated in a conventional cryostat and extensively tested and charac-

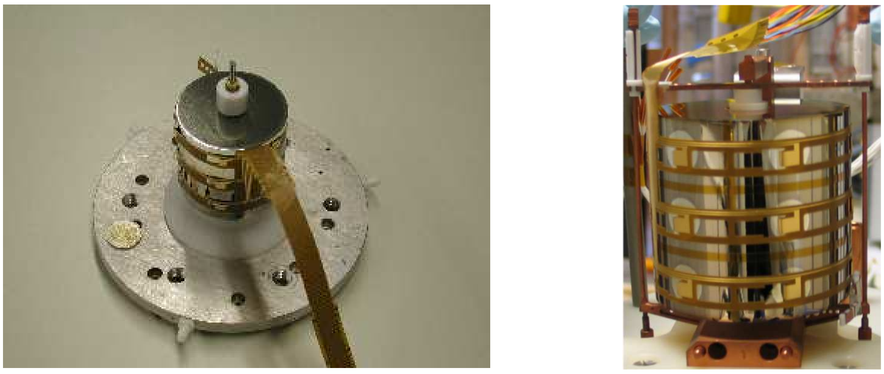

(a) (b)

Figure 3.8: Siegfried series of detectors with Kapton FPCB contact cables around: (a)Siegfried I and (b) Siegfried II.

Table 3.1: Detector specifications as provided by Canberra-France.

Parameter	*Siegfried* I	*Siegfried* II
Outer diameter (mm)	75.0	75.2
Inner diameter (mm)	10	10
impurity (10^{10} cm^{-3})	0.70(top), 1.35(bottom)	0.35(top), 0.55(bottom)
Height (mm)	69.8	70.2
Operating voltage (V)	+3000	+2000
FWHM at 122 keV (keV)	0.99	0.96
FWHM at 1333 keV (keV)	1.99	2.11

terized [123]. Siegfried II was operated in liquid nitrogen for five months. The handling, operating and testing of the prototype detectors and the physics analyses based on the data from them are the main topics of this thesis and will be discussed in detail in the following chapters.

3.4 Sensitivity

A dedicated discussion of the sensitivity of GERDA can be found in Ref. [71]. Figure 3.9a taken from Ref. [71] shows the expected 90% probability lower limit on the half-life of $0\nu\beta\beta$ decay versus the exposure under different background conditions. Figure 3.9b shows the expected 90% probability upper limit on the effective Majorana neutrino mass versus the exposure under different background conditions.

For GERDA Phase I, assuming a background level of 10^{-2} events/(kg·keV·year) and an exposure of 30 (kg·year), an upper limit on $m_{\beta\beta}$ of 0.42 eV is achievable. For Phase II, assuming a background level of 10^{-3} events/(kg·keV·year) and an exposure of 100 (kg·year),

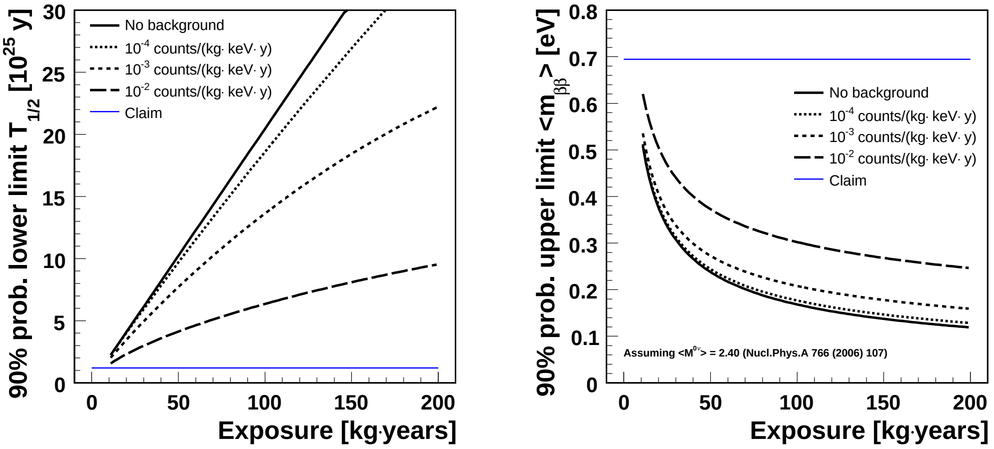

(a) (b)

Figure 3.9: Sensitivity of GERDA: (a) the expected 90% probability lower limit on the half-life for $0\nu\beta\beta$ decay and (b) the expected 90% probability upper limit on the effective Majorana neutrino mass versus the exposure under different background conditions. Also shown is the half-life and the effective Majorana neutrino mass for the claimed observation by H. V. Klapdor-Kleingrothaus *et al.* [62]. All mass values are determined from the half-life using the matrix elements reported in Ref. [73].

an upper limit on $m_{\beta\beta}$ of 0.2 eV is achievable.

Chapter 4

Signal formation in germanium detectors

When particles ($\alpha, \beta, \gamma, n, p$, etc.) interact inside the germanium semiconductor detector, they create electron-hole pairs, which act as charge carriers. Due to the electric field inside the detector the charge carriers drift and induce electric signals in electrodes. The electric signals are amplified, digitized and recorded by the electronics and data acquisition systems connected to the germanium detector. The whole process of signal formation in germanium detectors and their supporting electronics is briefly reviewed in this chapter.

4.1 Interactions of radiation with matter

4.1.1 Electrons and positrons

Electrons and positrons traversing matter lose their kinetic energy mainly by two processes, ionization and bremsstrahlung. High energy (GeV range) electrons and positrons predominantly lose energy by bremsstrahlung. Low energy (MeV range) electrons and positrons predominantly lose energy by ionization. The energy at which an electron or a positron loses as much energy in collisions as in radiation is called critical energy ϵ. For elements with charge $Z > 13$ the critical energy is [124]

$$\epsilon = (550/Z)\ \text{MeV}. \tag{4.1}$$

For germanium $\epsilon \approx 17$ MeV. Hence, electrons emitted from the double beta decay of ^{76}Ge mainly loss their energy by ionization.

The range of electrons and positrons depends on their energy and the material they traverse (see Ref. [125] and references therein). The average range of a 1 MeV electron in germanium is about 0.5 mm.

After a positron has lost all its kinetic energy, it annihilates with an electron into two photons with an energy of 511 keV each, corresponding to the rest mass of electrons.

4.1.2 Photons

Photons emitted by radioactive isotopes have energies ranging from several keV to several MeV. The possible interaction processes of photons in matter are photoelectric effect, Compton (incoherent) scattering, Rayleigh (coherent) scattering and pair production. Since Rayleigh scattering does not change the energy of the scattered photon but only its momentum, it is not relevant for GERDA.

Photoelectric effect: When a photon interacts with an atom, its entire energy may be transferred to an atomic shell electron which leaves the shell. The energy of the secondary electron is equal to the difference of the incident photon energy and the binding energy of the electron. If the electron originates from an inner shell of the atom, an outer shell electron fills the vacancy. Consequently, either characteristic x-rays are emitted, or, if the x-ray photons are re-absorbed, secondary Auger-electrons are emitted. The cross section of the photoelectric effect is inversely proportional to the photon energy. Hence, the photoelectric effect is the main interaction mechanism for photons at low energy (up to about 200 keV for Ge).

Compton scattering: A photon scatters on a weakly bound electron (quasi-free), transferring only part of its energy and momentum. The angular distribution of the scattered photons is described by the Kein-Nishina formula. The maximum energy transfer occurs when the incident photon is scattered by 180°. Compton scattering is the predominant interaction process for photons of energies between about 200 keV and 8 MeV for germanium. A 1.33 MeV photon undergoes on average three Compton scatterings before being absorbed through the photoelectric effect. The mean free path of such a photon is about three centimeters.

Pair production: If the photon energy exceeds twice the rest mass of the electron, the photon can create an electron-positron pair in the electric field of a nucleus. The rest of the photon energy is transferred to the created electron and positron as kinetic energy. A significant cross section for this interaction mechanism arises only for energies above $4 \sim 5$ MeV.

4.1.3 Neutrons

Because of the lack of charge, neutrons have a relatively high penetration power. However, there are five processes that occur when neutrons interact with nuclei depending on the kinetic energy of the incident neutrons:

Capture: The nucleus, Z, absorbs the incident neutron, n, and de-excites with the emission of one or more photons, denoted as $^{\mathrm{A}}\mathrm{Z}(n,\gamma)$, where A is the atomic number of the nucleus. In case of **internal conversion** an electron from a lower shell of the nucleus is emitted instead of a photon, denoted as $^{\mathrm{A}}\mathrm{Z}(n,e)$. The excited nucleus can also be metastable and not de-excite instantaneously, denoted as $^{\mathrm{A}}\mathrm{Z}(n,\gamma^m)$. Capture is the dominant process for thermal neutrons, i.e., neutrons with energies in the sub-eV range.

Elastic scattering: A neutron collides with a nucleus, transfers some energy to it and bounces off in a different direction; the target nucleus gains the energy lost by the neutron (also called recoil energy). This is one of the significant processes for neutrons with energies in the range of keV to several tens of MeV. The recoil energy is very small (mostly less than 200 keV) and has an exponentially decaying distribution. Hence, this process is not relevant as a background for $0\nu\beta\beta$ decay searches.

Inelastic scattering: A nucleus temporarily absorbs the incident neutron and forms a compound nucleus in an excited state. It then de-excites by emitting another neutron of lower energy together with a photon which takes the de-excitation energy. The nucleus takes some recoil energy. The reaction is denoted as $^{\mathrm{A}}\mathrm{Z}(n, n'\gamma)$ and is significant for neutrons with energies in the range of 1 to several tens of MeV.

Transmutation: A nucleus absorbs a neutron and then de-energizes by emitting a proton, p, or an α particle. This produces a nucleus of a different element. The process can occur when the incident neutron energy exceeds ≈ 100 MeV and becomes dominant at several GeV.

If the neutron energy is even higher, fission reactions occur. Such high energy neutrons can only be produced by cosmic ray muons which are vetoed by the muon detecting system in GERDA. However, the meta-stable nuclei created by such neutrons could be a serious background for the $0\nu\beta\beta$ decay search (see Sec.3.2.1).

4.2 Germanium detectors

4.2.1 Working principle of semiconductor detectors

Insulators, semiconductors and conductors are distinguished according to the energy gap between the valence and the conduction bands. The widths of the band gap of semiconductors are between those of insulators and conductors and are of the order of several eV. This allows an electron to be lifted from the valence to the conduction band by thermal motion or external ionizing radiation.

The resistivity of a semiconductor is determined by impurities (dopant) in its crystal lattice. Elements with only three valence electrons create energy states a little bit higher than the valence band, making it easy to lift valence electrons to these states and create freely moving holes in the valence band. This kind of dopant is called acceptor. The semiconductor doped with them is called p-doped. Elements with five valence electrons donate electrons to energy states a little bit lower than the conduction band, making it easy to lift these weakly bound electrons to the conduction band. This kind of dopant is called donor. The semiconductor doped with them is called n-doped. In general, the thermal energy available at room temperature is sufficient to ionize most of the dopant. The created freely moving electrons and holes are called charge carriers.

A p-n junction forms when p- and n-doped pieces of semiconductor are placed together. The charge carriers diffuse into regions with lower concentrations and are eliminated by recombination. Left behind are the charged ions adjacent to the interface in a region with no mobile carriers, called the *depletion zone.* Since these ions create positive space charges on the n side and negative ones on the p side, an electric field is created providing a force opposing the continued diffusion of charge carriers. The size of the depletion zone changes when an external potential is applied to the junction. Under *reverse bias* (anode connected to the n side, cathode to the p side) the majority charge carriers are driven away from the junction. This widens the depletion zone. Since the carrier density is small in the depletion zone, only a very small reverse saturation current occurs. Likewise, the depletion zone squeezes under *forward bias* while the current strongly increases.

The depletion zone is the active volume of any semiconductor detector. When ionizing radiation strikes the depletion zone, some of its deposited energy excites electrons out of the valence band and electron-hole pairs are created. Due to the electric field electron-hole pairs cannot recombine but split and drift towards the electrodes and induce electric signals there. In most of the cases a reverse bias is applied in order to create an active volume as large as possible. The bias voltage turning the whole bulk of a semiconductor detector into a depletion zone is called the full depletion voltage.

4.2.2 Operating voltage of germanium detectors

The depletion depth is proportional to the square root of the ratio of the applied voltage and the dopant concentration. The fewer dopants, the bigger the depleted region under a certain reverse bias. The concentration of active impurities in germanium detectors is of the order of $10^{10}/\mathrm{cm}^3$. Germanium has about 10^{22} atoms per cm^3. The dopant concentration in germanium detectors is thus of the order of 1 ppt (particle per trillion) which is extremely low. Consequently, the depletion voltages of germanium detectors are two orders of magnitude lower than for silicon detectors of the same size. This allows the construction of large germanium detectors operating at relatively low voltage. The largest germanium detectors are based on a cylindrical geometry with diameter and height both in the several centimeter range. The full depletion voltage for them is just several kilo-volts. The operating voltage is normally a little bit above the full depletion voltage to ensure a regular electric field.

4.2.3 Operating temperature of germanium detectors

The smaller the band gap, the higher the probability that an electron is transferred to the conduction band. The band gap in germanium is 0.72 eV, in silicon it is 1.1 eV. At room temperature the population of electrons in the conduction band in germanium is a factor of 1000 higher than in silicon. Applying a bias voltage to a germanium detector with a large bulk (about several cm) at room temperature would create a large current. This would make the operation impossible[1], or even destroy the detector. Germanium detectors are usually cooled via a metal cooling stick submerged in a cooling medium, *e.g.*, liquid nitrogen, to suppress thermal excitation.[2] Due to imperfect heat conduction the temperature of the germanium crystal is slightly higher than that of the cooling medium.

---

[1] The large bulk current creates a large noise distorting any signal.

[2] The number of thermally excited electrons could be very small when the germanium volume becomes small. Germanium pieces thinner than several microns are used to make room temperature detectors. No high voltage is needed to create the depletion zone. The leakage current is very small. The noise from the thermal excitation also becomes tolerable given very few thermally excited electrons.

4.2.4 Types of germanium detectors

Germanium detectors are naturally divided into two classes characterized by the active impurities in the bulk material. If the impurities are mainly acceptors, the material is *p*-doped and the detector is called *p*-type. If the impurities are mainly donors, the material is *n*-doped and the detector is called *n*-type.

Large germanium detectors normally have a cylindrical shape. They can be divided into two types: *true coaxial* and *closed-ended coaxial*. In both cases the shape is cylindrical with an inner bore.[3] For true coaxial detectors the core is completely removed, whereas for the closed-ended coaxial geometry the core is only partially removed leaving a *cap* on one side.

The outer surface layer of a *p*-type detector is normally converted into *n*-type with a typical thickness of about 0.5 mm by diffusing lithium. It is sometimes classified as a *dead layer*, because the charge carriers created in this layer cannot be detected. The inner surface of a *p*-type detector is implanted with boron in order to make good electric contact. The thickness of the implantation is of the order of several microns. *n*-type detectors have the lithium drifted zone and thus the dead layer on the inner surface. Hence they have less inactive volume. The boron implantation is on the outside.

Germanium detectors can also be classified as segmented or unsegmented. The segmentation is normally performed on the outer surface of the detector. For *p*-type detectors the outer surface is milled in order to penetrate the thick lithium-drifted layer. The fringe depths and thicknesses of the segments are of the order of a millimeter. Distortions in the electric field are expected in this case. For *n*-type detectors photo-lithographic techniques are used to form the segments. The electric field is expected to be quite homogeneous.

4.3 Charge carriers

4.3.1 Creation of charge carriers

A big fraction of the energy deposited by incident radiation causes the excitation of phonons, the rest excites electrons from the valence band to the conduction band. Thus, the average energy needed to create one electron-hole pair, called pair energy, is much bigger than the band gap. In germanium the pair energy is 2.95 eV at 80 K.

4.3.2 Electric field and carrier drift

The reverse bias applied to the electrodes creates an electric field in the bulk of the germanium detector which lets the charge carriers drift to the electrodes. The field **E** is determined by the boundary conditions as well as the space charges in the depletion zone. It can be calculated by solving Poisson's equation:

$$\nabla \cdot \mathbf{E} = \frac{\rho}{\epsilon}, \tag{4.2}$$

---

[3] There are also some germanium detectors having no hole in the middle. All the contacts are on the surface.

where ρ is the space charge density defined by the effective number of impurities and ϵ is the dielectric constant.

4.3.3 Effects of crystal structure

The relation between the drift velocity of the charge carriers, $\mathbf{v}_{e/h}(\mathbf{r})$, and the electric field, $\mathbf{E}(\mathbf{r})$ can be simply expressed as:

$$\mathbf{v}_{e/h}(\mathbf{r}) = \mu_{e/h}\mathbf{E}(\mathbf{r}), \tag{4.3}$$

where $\mu_{e/h}$ is called the *mobility* and $\mathbf{r}$ indicates the position. In germanium detectors operating at low temperatures the mobility is influenced by the crystal lattice orientation and taking a complex form instead of a number. The drift velocities along different directions differ from each other (longitudinal anisotropy) and are not always parallel to the electric field (transverse anisotropy). The angle between the drift direction and the electric field is known as the Sasaki angle [126]. A detailed discussion of the effects of the crystal structure on the charge carrier drift is formed in Chapter 10.

4.4 Induction of signals in detector electrodes

Electric signals are induced in the electrodes of a detector by the cumulative influence of electrons and holes moving toward the electrodes. Shockley-Ramo's Theorem [127,128,129] can be used to calculate the time development of the induced charge $Q(t)$ or current $I(t)$ in each electrode:

$$Q(t) = -Q_0 \times [\varphi_w(\mathbf{r}_h(t)) - \varphi_w(\mathbf{r}_e(t))], \tag{4.4}$$

$$I(t) = Q_0 \times [\mathbf{E}_w(\mathbf{r}_h(t)) \cdot \mathbf{v}_h(t) - \mathbf{E}_w(\mathbf{r}_e(t)) \cdot \mathbf{v}_e(t)], \tag{4.5}$$

where Q_0 is the electric charge carried by electrons or holes, $\mathbf{r}_{e/h}(t)$ and $\mathbf{v}_{e/h}(t)$ are the position and velocity vectors of electrons/holes as a function of time, and $\varphi_w(\mathbf{r})$ and $\mathbf{E}_w(\mathbf{r})$ are the so-called *weighting potentials* and *weighting fields*. They can be calculated by solving Poisson's equations, $\nabla^2\varphi(\mathbf{r}) = 0$ and $\nabla \cdot \mathbf{E}(\mathbf{r}) = 0$, with the boundary condition that the potential on the electrode of interest equals to 1 and the potentials on all other electrodes equal to zero.

Figure 4.1a shows the weighting potential of a segment with the indication of an event for the cross section at the center of a Siegfried-like detector. Figure 4.1b shows the raw charge and current pulses induced by the resulting hit in this particular segment, its neighboring segments and the core of the detector. The pulses induced in the neighboring segments are called *mirror pulses.* The amplitude of the mirror pulse induced in one neighboring segment is larger than in the other, because the trajectory of the hit is closer to this segment.

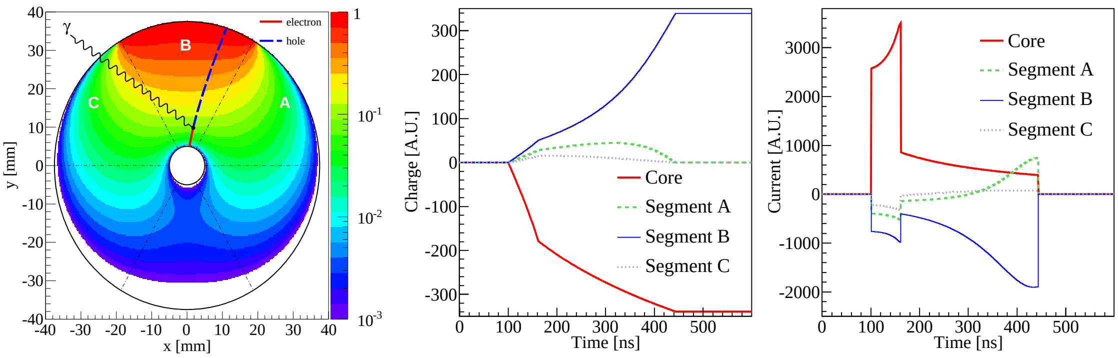

(a) (b)

Figure 4.1: (a) weighting potential of segment B together with an indication of a γ interaction. (b) Simulated charge and current pulses induced in segments A, B and C.

4.5 Electronics

4.5.1 Noise

The total energy resolution in terms of the full width at half maximum (FWHM) of the peak under study, W_T, is composed of three terms:

$$W_T^2 = W_D^2 + W_X^2 + W_E^2, \tag{4.6}$$

where W_D describes the statistical fluctuations of the creation of electron-hole pairs, W_X describes the effect of incomplete charge collection and scales linearly with the incident energy, and W_E accounts for noise contributions from the electronics and does not depend on energy. Given a perfect electronic system, germanium detectors have an energy resolution of about 2 keV at 1.3 MeV, where W_X dominates the contribution and W_D contributes less than 1 keV. These two contributions cannot be reduced. In reality, thermal noise in the pre-amplifiers and noise picked up by the cables and connectors contribute significantly to the total noise. These contributions have to be kept as small as possible.

4.5.2 Cross talk

For segmented germanium detectors, signals from all the electrodes are read out simultaneously. There is intrinsic cross talk between different channels because of the capacitive couplings between electrodes. This cross talk is not due to improper electric connections, hence cannot be avoided. However, it can be reduced to an acceptable level by choosing proper values of resistors and capacitors used in the pre-amplifier coupling and feed-back circuits to match the intrinsic capacities between detector electrodes. A detailed analysis is found in Chapter 4 of Ref. [130] and references therein.

Chapter 5

Detector test facilities

Several test facilities were developed at the Max-Planck-Institut für Physik, Munich, for research and development of segmented n-type germanium detectors like the ones to be used in GERDA Phase II. The operation and performance of several segmented detectors in vacuum and submerged in cryogenic liquid were systematically examined; various data samples were taken to investigate the event discrimination power of segmented germanium detectors. The test facilities are briefly discussed in this chapter. The data and analyses based on them are described in the following chapters.

5.1 Cryostats

5.1.1 Vacuum cryostat

Canberra-France developed a test cryostat shown in Fig. 5.1. A standard liquid nitrogen dewar is complemented by a two-walled aluminum vacuum can with a combined thickness of 6 mm. The detector was placed inside the can and the coordinate system was chosen such that its center was at $z = 66$ mm and $r = 0$ mm. The vacuum can extended to $z = 116$ mm and $r = 75$ mm. A copper cooling finger was used as a thermal link between the detector and the dewar. The temperature was monitored at several locations using Pt100 resistors. Liquid nitrogen was refilled daily, maintaining a temperature stability of about ±3 K. A comparison of spectra taken at different temperatures within this range showed neither significant differences in the general shape of the spectra nor in the energy resolution.

5.1.2 Gerdalinchen II

Gerdalinchen II (GII) is a special cryostat developed by the technical division of the Max-Planck-Institut für Physik to test the operation of up to three segmented germanium detectors submerged in cryogenic liquid. Figure 5.2a is a schematic of the main body of GII, a two-walled cryogenic dewar inside a cylindrical aluminum tank with a height of 960 mm and a diameter of 612 mm. The top flange can be moved up, allowing the

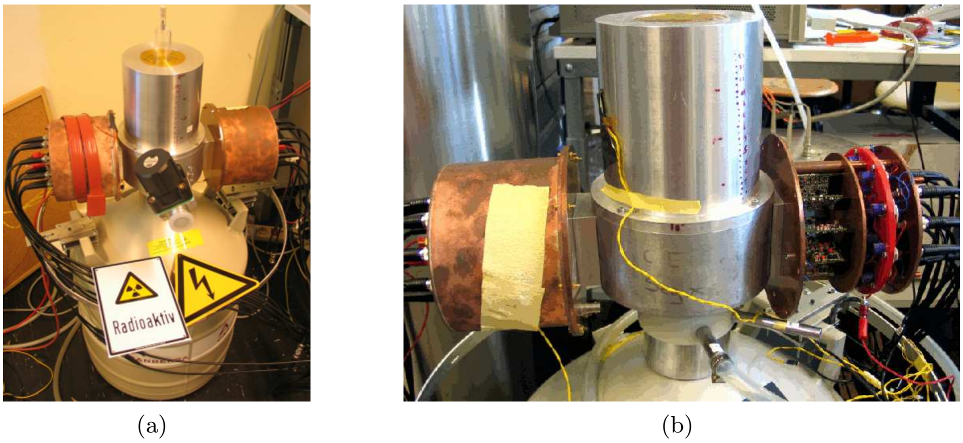

(a) (b)

Figure 5.1: Test cryostat developed by Canberra-France: (a) the standard liquid nitrogen dewar with the vacuum can on top and (b) a close-up of the vacuum can and the copper "ears" housing the pre-amplifier boards.

mounting of detectors to a vertical stainless steel bar attached to the bottom of the flange, see Fig. 5.2c. Figure 5.2b shows GII in operation with a neutron source placed on its side. For more details please see Fig. 6.1 in the next chapter.

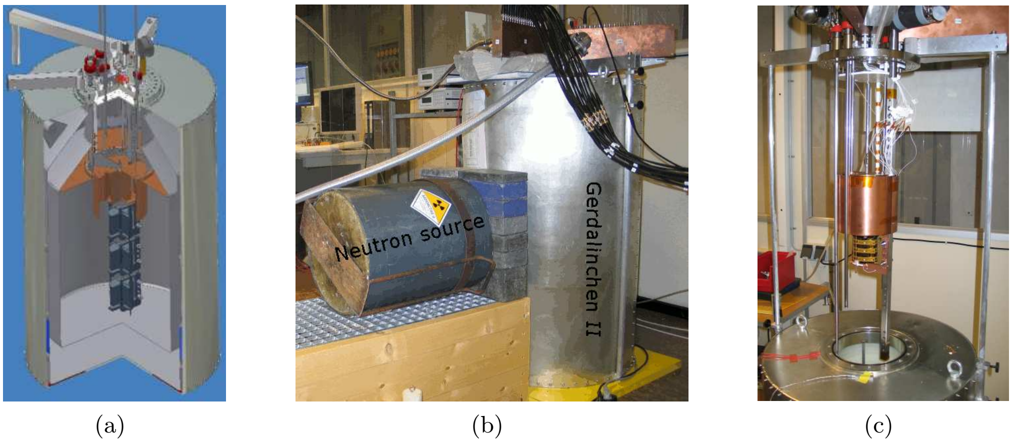

(a) (b) (c)

Figure 5.2: Gerdalinchen II cryostat. (a) schematic of GII, (b) GII in operation with a neutron source and (c) detector installation above GII dewar.

There are three high voltage feed-throughs and four signal connectors, each with 18 channels, on the GII flange. This allows the operation of up to three 18-fold segmented detectors simultaneously. The flange also facilitates the re-filling of the dewar with cryogenic liquid and the flushing with gaseous nitrogen without opening the system. The dewar is re-filled daily to keep the level of the cryogenic liquid above the infrared shields, and the liquid level is monitored using several PT100 thermal resistances mounted at different places inside the dewar (see Fig. 6.1).

5.2 Electronics

5.2.1 Front-end

The read-out scheme of a segmented detector mounted inside the vacuum cryostat is shown in Fig. 5.3a. The signals were read out using charge sensitive PSC-823C pre-amplifiers with a decay time of 50 μs. The FET for the core electrode was mounted inside the cryostat close to the detector, the FETs for the segment electrodes were incorporated into the pre-amplifier boards which were housed inside the copper ears on both sides of the detector as shown in Fig. 5.1b. Figure 5.3b depicts the layout of the feed-throughs between the vacuum can and the copper ears.

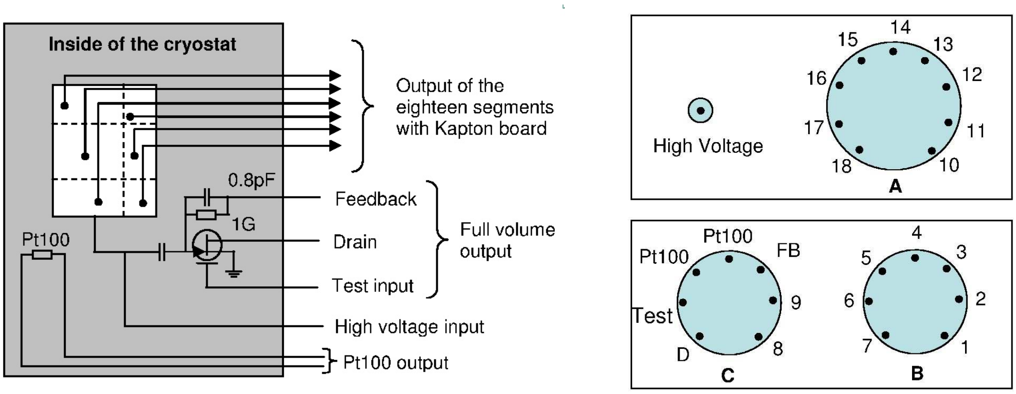

(a) (b)

Figure 5.3: Frond-end electronics of a segmented detector mounted in the vacuum cryostat: (a) read-out scheme and (b) layout of the feed-throughs between the vacuum can and the copper ears.

A different setup was used in GII. The FET for the core electrode was incorporated into the pre-amplifier boards like for the segment electrodes. Thus, the cross talk from the core signal to the segment signals was minimized. All the pre-amplifier boards were mounted in a copper box and shared a common ground as shown in Fig. 5.4b. The filters for the high voltage lines and the coupling capacitors for the core signal cables were placed under the top flange as shown in Fig. 5.4a. They were first operated above the cryogenic liquid level and later submerged for better temperature stability.

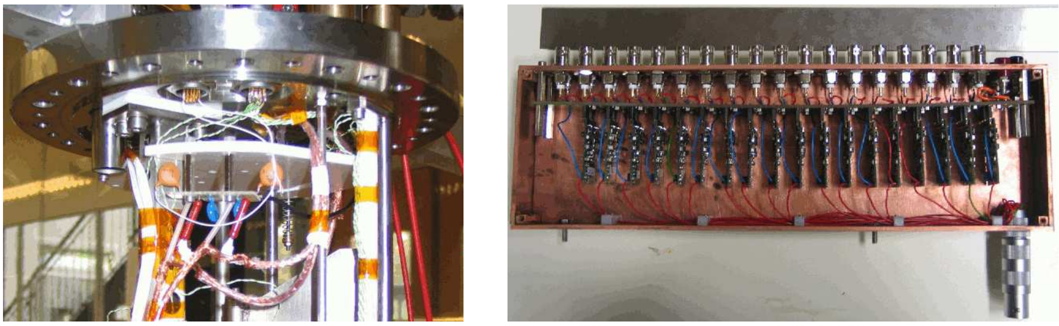
(a) (b)

Figure 5.4: Front-end electronics in GII: (a) high voltage filters and coupling capacitors and (b) pre-amplifier box for a segmented detector.

5.2.2 DAQ

The pre-amplified signals are digitized using an XIA data acquisition system [131] based on 14-bit ADC PIXIE-4 modules with a sampling rate of 75 MHz. The bandwidth of the analog signals is limited by a Nyquist filter to half the sampling rate, *i.e.* 37.5 MHz. This avoids aliasing the noise from higher frequencies. It is implemented in the analog section of the PIXIE-4 module as a low-pass Sallen-Key filter resulting in a sharp cut-off at this frequency.

Energies of the pulses are calculated using software filters. In principle, the energies of both positively and negatively polarized pulses can be calculated. However, since the polarization of all channels was set to be positive, there should not be any negative pulse. The system was configured such that only the energies of positive pulses were calculated and the energies of other kinds of pulses were simply set to zero rather than calculated. This led to the observation of a special type of events with negative pulses in some of the channels as will be described in Chapter 7.

Recorded pulse shape data consist of 300 samples of the integrated charge amplitude. The delay for the onset of the signal can be set by hand and was set to 1 μs for most of the measurements. The trigger and energy thresholds of the core and segment electrodes can be set to different values. Pile-up pulses can be rejected or stored using a rough energy estimation.

5.3 Monitoring

The operation of the test facilities requires the monitoring of high voltage supplies, temperature monitors, vacuum gauges, oxygen sensors, etc.. The monitoring needs to be automated for overnight and long term measurements. A generalized “Laboratory Monitor system”, LaMo, was developed to monitor and control most of the hardware in the laboratories using the graphic programming language, LabVIEW. The system has a set of user friendly interfaces to perform most of the common lab tasks and a modularized design of the functionality to facilitate the implementation of new pieces of hardware.

Figure 5.5 shows the most important control panels of LaMo. The main panel is called “Laboratory” as shown in Fig. 5.5a. It shows a list of experiments going on in the laboratory and their status. An experiment can be created, edited, started, stopped using the buttons next to the experiment list. The “Laboratory” panel also provides functions common to all experiments, such as email alerts, electricity, oxygen sensors, etc.. Pieces of hardware to be associated to an experiment can be chosen from a list of available hardware. This is done in the “Config” panel of LaMo as shown in Fig. 5.5b, where pieces of hardware can be added or deleted from the list to be monitored. Once an experiment is created and configured, it is started from the “Laboratory” panel. An “Experiment” panel, as shown in Fig. 5.5c, where monitored variables are shown in different ways, automatically pops up. The functions specified for a particular experiment can be executed from there.

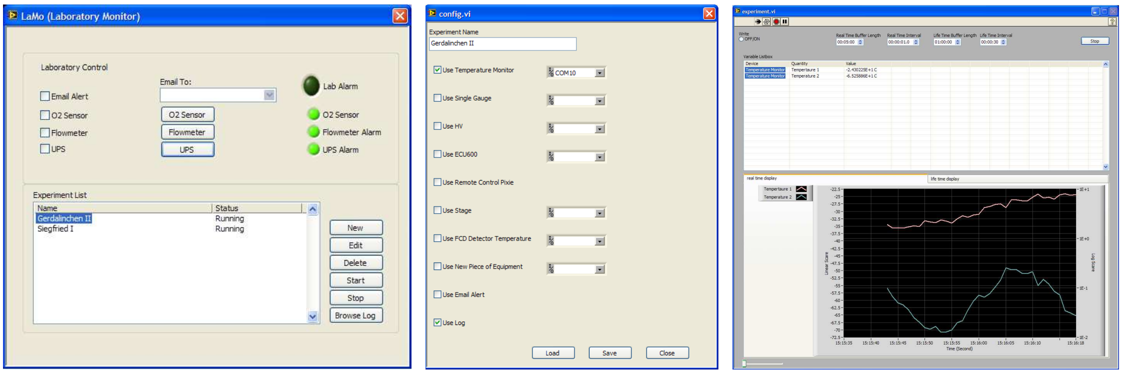

Laboratory Control

☐ Email Alert
☐ O2 Sensor
☐ Flowmeter
☐ UPS

Email To:

Experiment List

Name	Status
Gerdalinchen II	Running
Siegfried I	Running

Experiment Name: Gerdalinchen II

☑ Use Temperature Monitor COM10
☐ Use Single Gauge
☐ Use HV
☐ Use ECU600
☐ Use Remote Control Pixie
☐ Use Stage
☐ Use FCD Detector Temperature
☐ Use New Piece of Equipment
☐ Use Email Alert
☑ Use Log

Write ○ OFF/ON

Real Time Buffer Length: 00:05:00
Real Time Interval: 00:00:01.0
Life Time Buffer Length: 01:00:00
Life Time Interval: 00:00:30

Variable Listbox

Device	Quantity	Value
Temperature Monitor	Tempertaure 1	-2.430225E+1 C
Temperature Monitor	Temperature 2	-6.525886E+1 C

(a) (b) (c)

Figure 5.5: Main panels of LaMo: (a) “Laboratory” panel: it provides a list of experiments and their status, and gives access to functions common to all experiments; (b) “Config” panel: pieces of hardware to be associated to an experiment can be added, deleted from the list to be monitored; (c) “Experiment” panel: various displays of monitored variables can be requested and the execution of experimental tasks can be steered.

The common user interface enforces common I/Os for different pieces of hardware. The functionality of LaMo is modularized so that the effort to implement a new piece of hardware is minimized. To add a new piece of equipment the developer only needs to define its I/O interface to LaMo. The other efforts, such as programming the user interface, etc., do not have to be repeated every time.

Chapter 6

Operation of segmented detectors in liquid nitrogen

Segmented *n*-type germanium detectors will be directly submerged in cryogenic liquid in GERDA Phase II. It is therefore very important to study the performance of segmented detectors in cryogenic liquid. Siegfried II, the second 18-fold segmented *n*-type prototype detector built (see Sec. 3.3.3), was inserted into the Gerdalinchen II test stand (see Sec. 5.1.2) containing liquid nitrogen on April 23rd, 2008. It was kept in liquid nitrogen for nearly five months and was warmed up on September 15th, 2008. The resolutions and leakage currents of the core and all segments were constantly monitored. Four short cool-down and warm-up cycles were carried out afterward to optimize the setup and perform dedicated measurements. The leakage currents were remeasured after each cool-down. The detector performance is summarized in this chapter.

6.1 Experimental setup

Figure 6.1 depicts the test stand with three segmented detectors mounted inside. Only the upper and middle detector positions were occupied during the measurements. The dewar is filled bottom up through a filling tube. The numbers inside parentheses indicate the positions of eight PT100 thermal resistors. They were used to monitor the level of the liquid nitrogen. Liquid nitrogen was added once per day to keep its level between PT100 (2) and (3). This ensured that the infrared shields were always kept inside the liquid nitrogen minimizing the infrared radiation load on the detector.

6.2 Cool-down test

The speed at which the detector strings will be lowered in GERDA has to be chosen such, that the whole process can be finished in a reasonable time without subjecting the strings and detectors to dangerous thermal and mechanical stress. The submersion speed envisioned for GERDA is 10 mm/min. The temperature profile of a detector during the

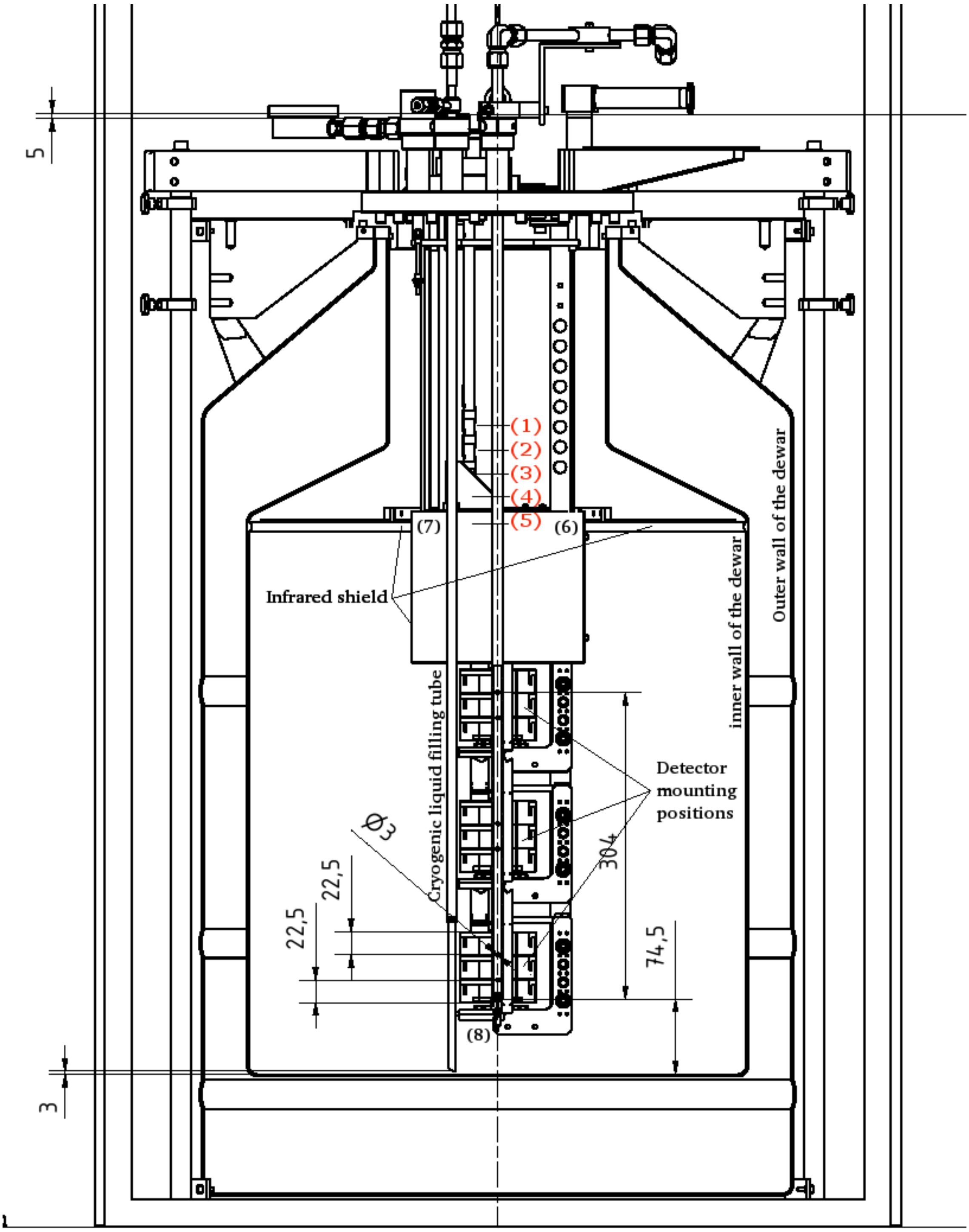

Figure 6.1: Gerdalinchen II setup to operate segmented detectors in liquid nitrogen. For details see text.

submersion process was studied in GII with an aluminum mock-up detector mounted at the highest GII position.

The rising of the liquid nitrogen level was tuned to about 10 mm/min. The temperature profile of the mock-up detector was monitored using three PT100 thermal resisters mounted on the top, bottom and in the middle of the mock-up. Figure 6.2 shows the temperature profiles of the mock-up detector during the filling of GII. In addition it shows the temperatures measured by the thermal sensor 8 near the bottom of the dewar and the thermal sensor 1 at the top most position always above the liquid. The largest temperature difference between the top and bottom of the detector occurred at the first contact of the detector with the liquid nitrogen. It was about 130°C and lasted about three minutes. While germanium has a thermal conductivity four times smaller than aluminum at room temperatures, the thermal conductivities of germanium and aluminum are almost equal at 80 K. Thus, it is expected that the germanium detector will cool down at about the same rate as the aluminum mock-up.

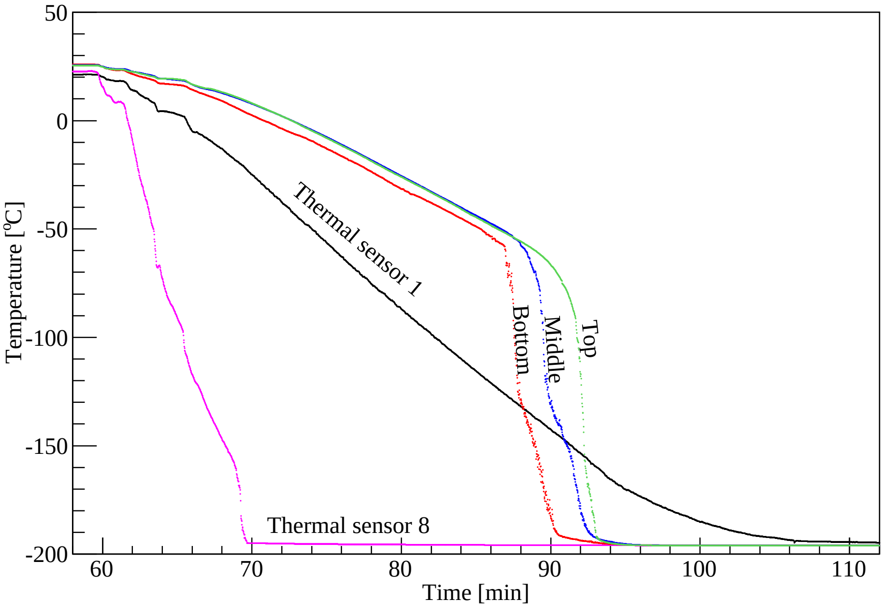

Figure 6.2: Temperature profile of a mock-up detector during the cool-down process. Curves are shown for sensors mounted on top, middle and bottom of the detector. Also shown are curves for sensors 8 and 1 mounted close to the bottom and top of the dewar.

6.3 Resolution

Siegfried II was mounted at the highest position in GII after a detailed cool-down procedure had been developed. It was cooled down on April 23^{rd}, 2008. The core and segment resolutions of Siegfried II were constantly monitored during the 140 days of operation.

The variation of the resolutions (FWHM) at 1332 keV is shown for the core in Fig. 6.3 and for all 18 segments in Fig. 6.4.

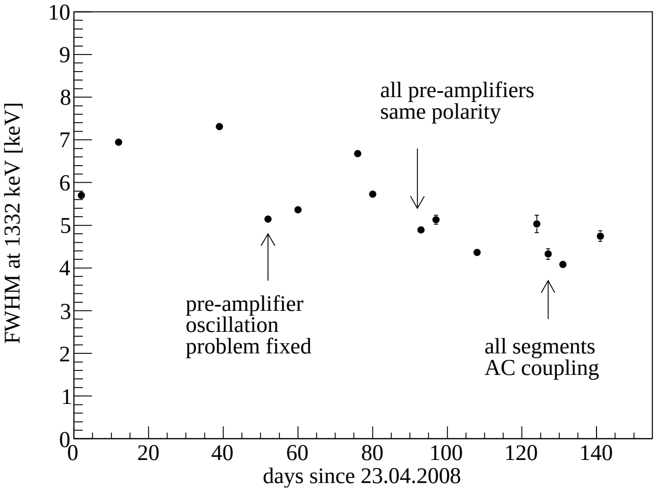

Figure 6.3: Core resolution of Siegfried II during 140 days of operation as determined from fits to the 1332 keV gamma line. The uncertainties on most values are hidden by the size of the dots.

During the first month of operation, all pre-amplifiers were oscillating whenever all 19 channels were read out simultaneously. The oscillations were due to an insufficient grounding scheme for the copper boxes holding and shielding the pre-amplifiers, see Fig. 5.4b. The problem was fixed by adding an extra copper plate inside the box, serving as the common ground for all pre-amplifiers. Afterward, all pre-amplifiers could be read out simultaneously and the core resolution was slightly better.

The second problem which affected the core resolution was related to the pulse polarity of the pre-amplifiers. Three pre-amplifiers (segments 3, 15 and 17) had a negative signal polarity while the rest had a positive one. This induced cross talk between these three pre-amplifiers and the core pre-amplifier. As a result the energy measured by the core for the 1332 keV photon line was 2 keV too low, if the energy was deposited in one of these three segments. These three pre-amplifiers were then replaced, resulting in some improvement in the core resolution as indicated in Fig. 6.3.

In order to decouple the segment potentials from the pre-amplifiers, all segment were AC instead of DC coupled ten days before the first warm-up, using 1 GΩ resistors and 2.2 nF capacitors. This neither influenced the core or segment resolutions.

6.4 Leakage current

The leakage current of Siegfried II at 2000 V was monitored during the 140 days of operation. Two measurement methods were used: (a) a direct measurement using a

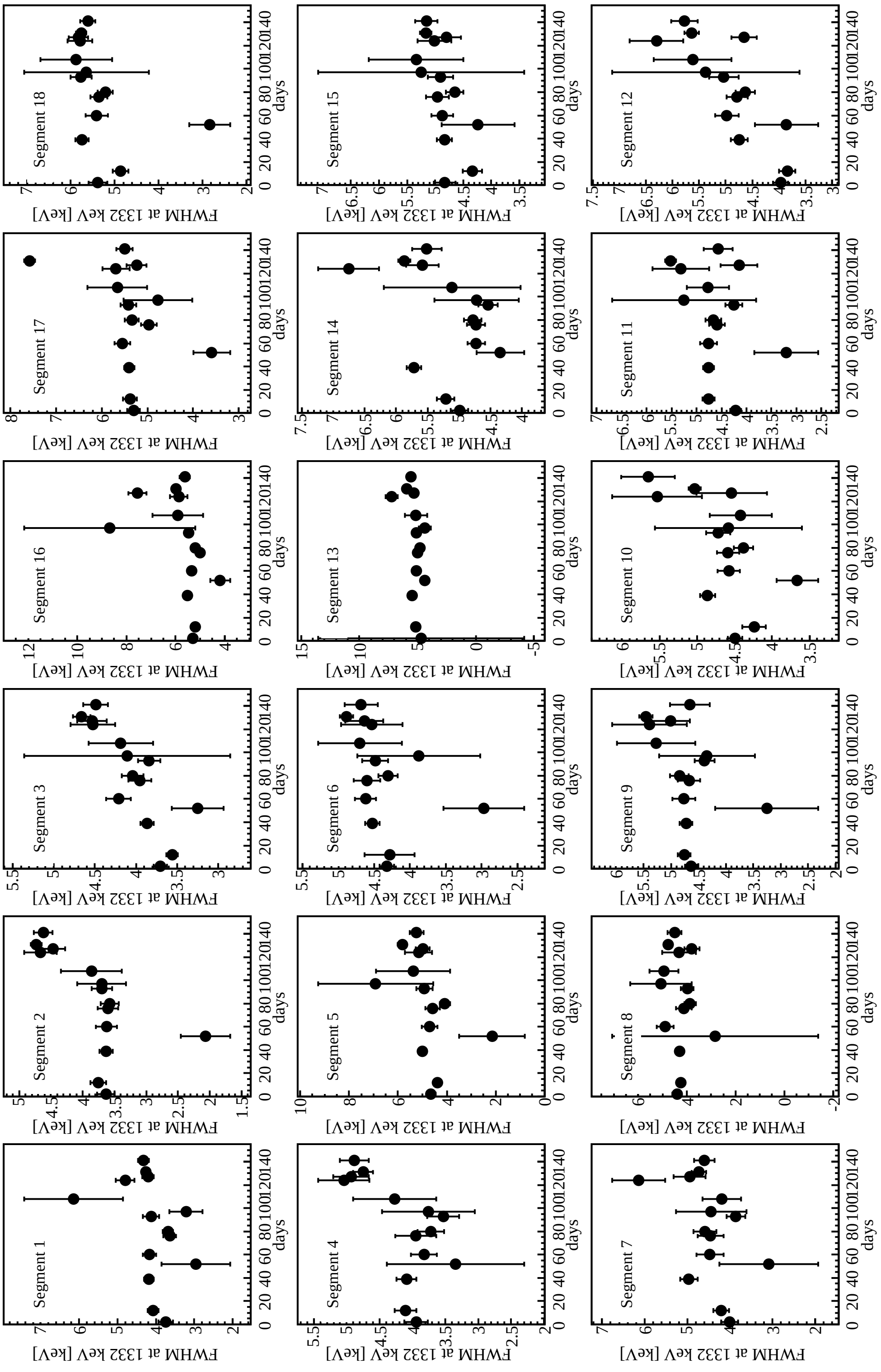

Figure 6.4: Segment resolutions of Siegfried II during 140 days of operation as determined from fits to the 1332 keV gamma line.

picoammeter and (b) an indirect measurement comparing the baselines at 0 V and 2000 V. The results from both methods are shown in Fig. 6.5. The leakage current stayed constant, around 20 pA. The absolute value of the leakage current given by method (b) depends on the relation of the input and output of the preamplifier, which was given by Canberra-France as a rough estimation. This may count for the systematic difference of the results given by the two methods.

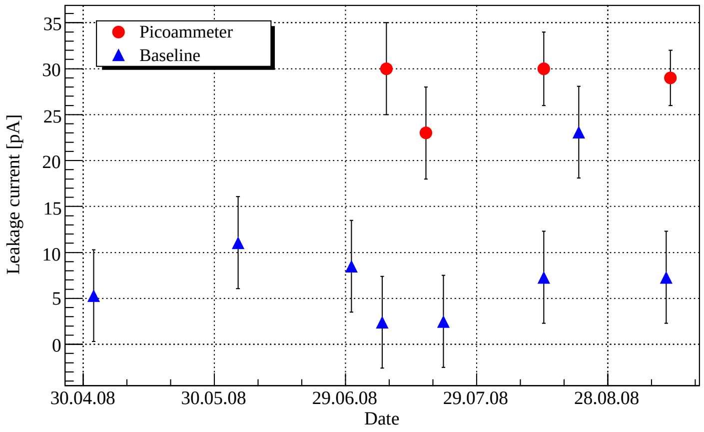

Figure 6.5: Leakage current of Siegfried II at 2000 V. The results from measurements using a picoammeter(dots) and baseline shifts(triangles) are given.

Siegfried I was added to the setup at the middle position in GII after the first warm-up of Siegfried II. Afterward, four cool-down and warm-up cycles were performed. The leakage currents of both detectors at operational voltage after each cool-down are shown in Fig. 6.6 and 6.7, respectively. The current measured for Siegfried I showed a significant increase after the third cool-down. This detector had previously been used to test HV contacts in the core and had to undergo reprocessing; it is known to have an imperfect core contact. The currents measured for Siegfried II immediately after each cool-down showed dramatic increases. However, within 40 minutes they dropped back to their original value. Later investigation revealed an increasingly bad segment contact which could account for the effect.

6.5 Summary

The 18-fold segmented detector Siegfried II was operated in liquid nitrogen for nearly five months. No degradation of the performance was observed. Both the Siegfried I and II detectors underwent four cooling cycles. The increase of the leakage current after each

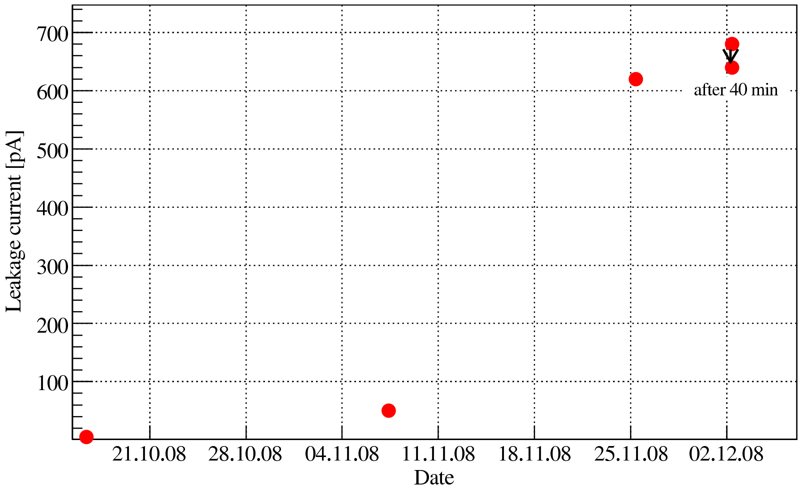

Figure 6.6: Leakage current of Siegfried I at 3000 V right after each cool-down. The currents were measured using a picoammeter.

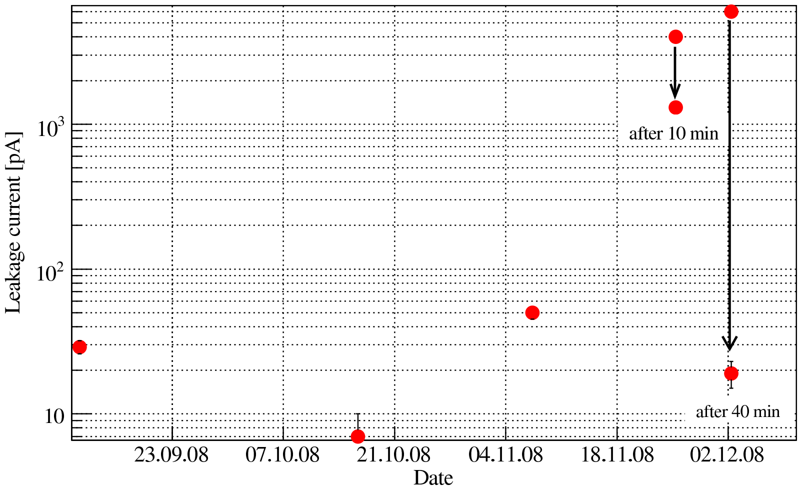

Figure 6.7: Leakage current of Siegfried II at 2000 V after each cool-down. The currents were measured using a picoammeter.

cooling cycle was observed in both detectors. However, there is strong evidence that this is due to the damage of the contacts instead of the detectors during the operation.

Chapter 7

Negative pulse events

During the operation of Siegfried II inside the Gerdalinchen II (GII) test stand (see Chapter 6), a peculiar class of events was observed in significant numbers. The pre-amplifiers and the DAQ system were configured such, that all channels had positive polarity, *i.e.*, all signal pulses had to be positive. About 5% of the events nevertheless had in at least one segment a negative baseline shift that could be interpreted as a "negative pulse".

7.1 An example

Figure 7.1 shows a typical negative pulse event. In this single-segment event all the energy was deposited in segment 1. The neighboring segments all show mirror pulses as expected from the weighting potentials. Almost all other segments, however, show some negative baseline shifts. In the following the phenomenon is investigated and an explanation proposed.

7.2 Selection of negative pulse events

If the energies of both positive and negative pulses are calculated, the sum of the the energies seen in all segments, $\sum E_{\text{segment}}$, is equal to the core energy, E_{core}, within the resolution. As described in Sec.5.2.2, the DAQ system was configured to set the energy of a negative pulse to zero instead of a negative value, and this causes $\sum E^{\text{DAQ}}_{\text{segment}}$ to be larger than E_{core}.

Figure 7.2 shows $\sum E^{\text{DAQ}}_{\text{segment}}$ versus E_{core} of a data sample collected with a ^{228}Th source mounted inside GII on top of Siegfried II. The two solid lines in the plot indicate the $\pm 10\sigma$ range around the core energy. Points above the upper solid line correspond to the negative pulse events, which were selected by requiring $\sum E^{\text{DAQ}}_{\text{segment}} - E_{\text{core}} > 10\sigma$.

There is also a small fraction of events with$\sum E^{\text{DAQ}}_{\text{segment}} < E_{\text{core}}$. This is due to threshold-effects, noise or pile-up; *i.e.*, two pulses are spaced in time such that the DAQ cannot provide a correct estimate of the core and segment energies. As there are quite

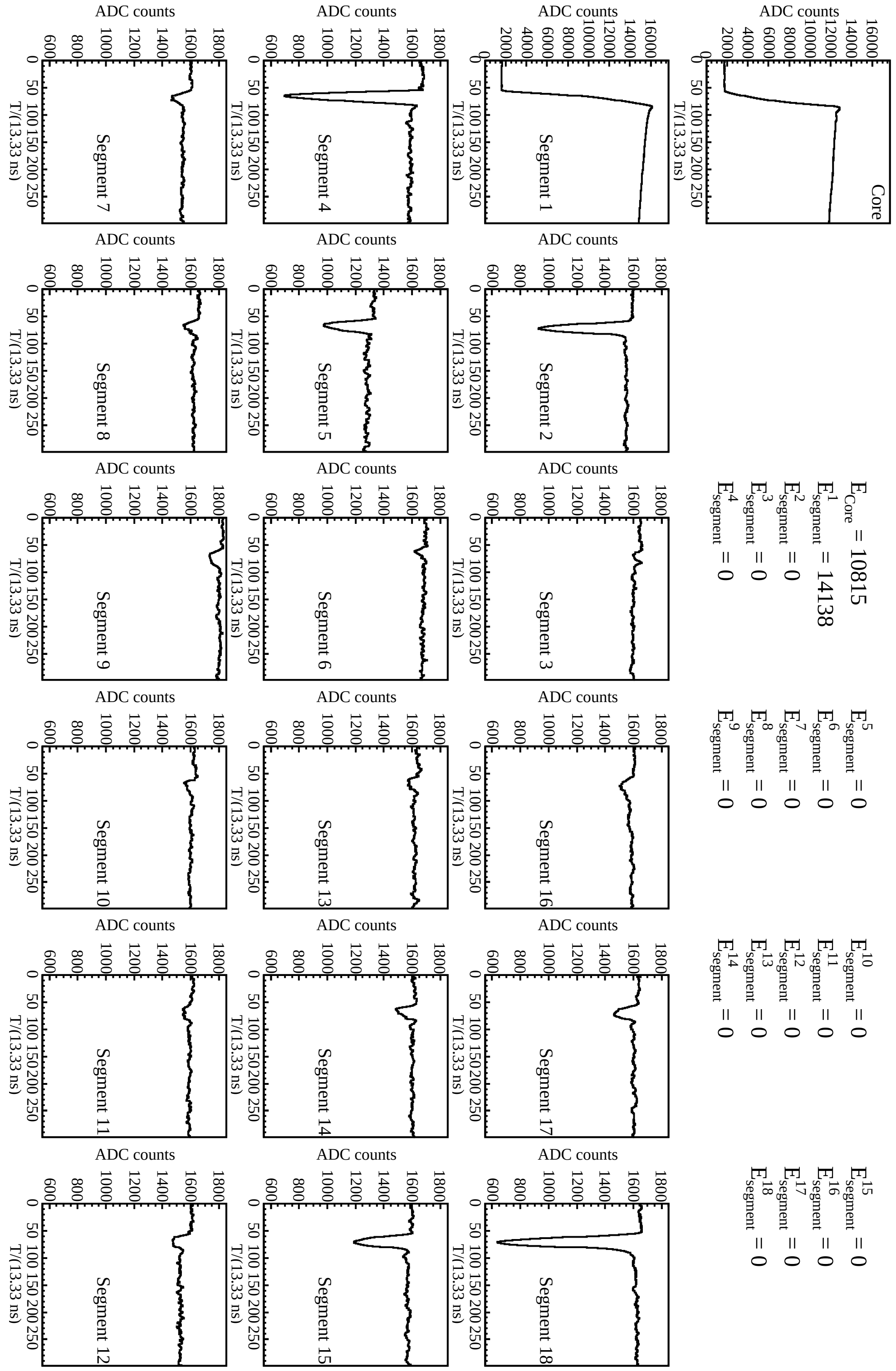

Figure 7.1: An single-segment event with energy deposited in segment 1 showing negative baseline shifts in almost all other segments. Mirror pulses are observed as expected.

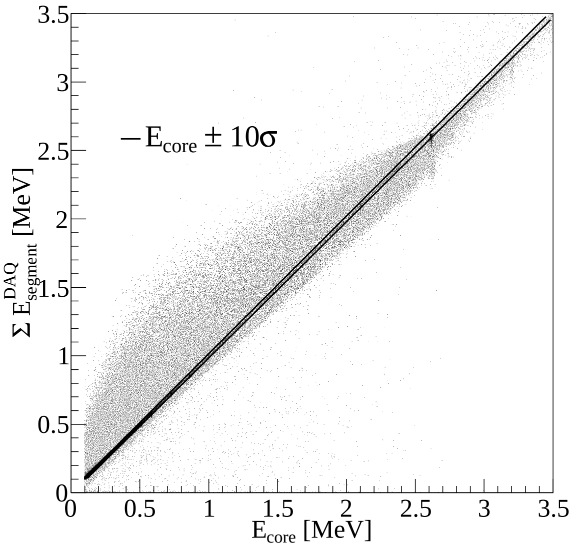

Figure 7.2: Sum of segment energies as determined by the DAQ versus the core energy. The two solid lines indicate the 10σ range around the core energy.

a number of events with an energy beyond 2.6 MeV, the pile-up effects are probably significant.

7.3 Location of negative pulse events

To localize the effect, the individual segment energies were plotted versus the core energy for the selected events. Figure 7.3 shows that predominantly the top and bottom segments feature the case $E^{\mathrm{DAQ}}_{\mathrm{segments}} > E_{\mathrm{core}}$. Very few negative pulse events were found in the segments in the middle of the detector.

Table 7.1 lists for each segment the total number of affected single segment events and the percentage it represents. The position of the source (above the detector) is clearly reflected in the differences of numbers of events between top and bottom segments. The percentage of affected events seems relatively constant for all segments of a layer. The bottom segments have a lower percentage of affected events than the top segments.

To investigate whether the events are concentrated at a particular radius, the risetimes of the events were studied. Figure 7.4 shows the distribution for normal and negative pulse events. The distribution for negative pulse events is significantly shifted toward higher risetimes. However, as the risetimes above ≈ 400 ns are in principle unphysical, this is probably not an indication that the events are located at very large or very small radii, but rather that they are located in regions where the electric field is not at full strength. Such regions can exist close to the top and bottom surfaces of the detector.

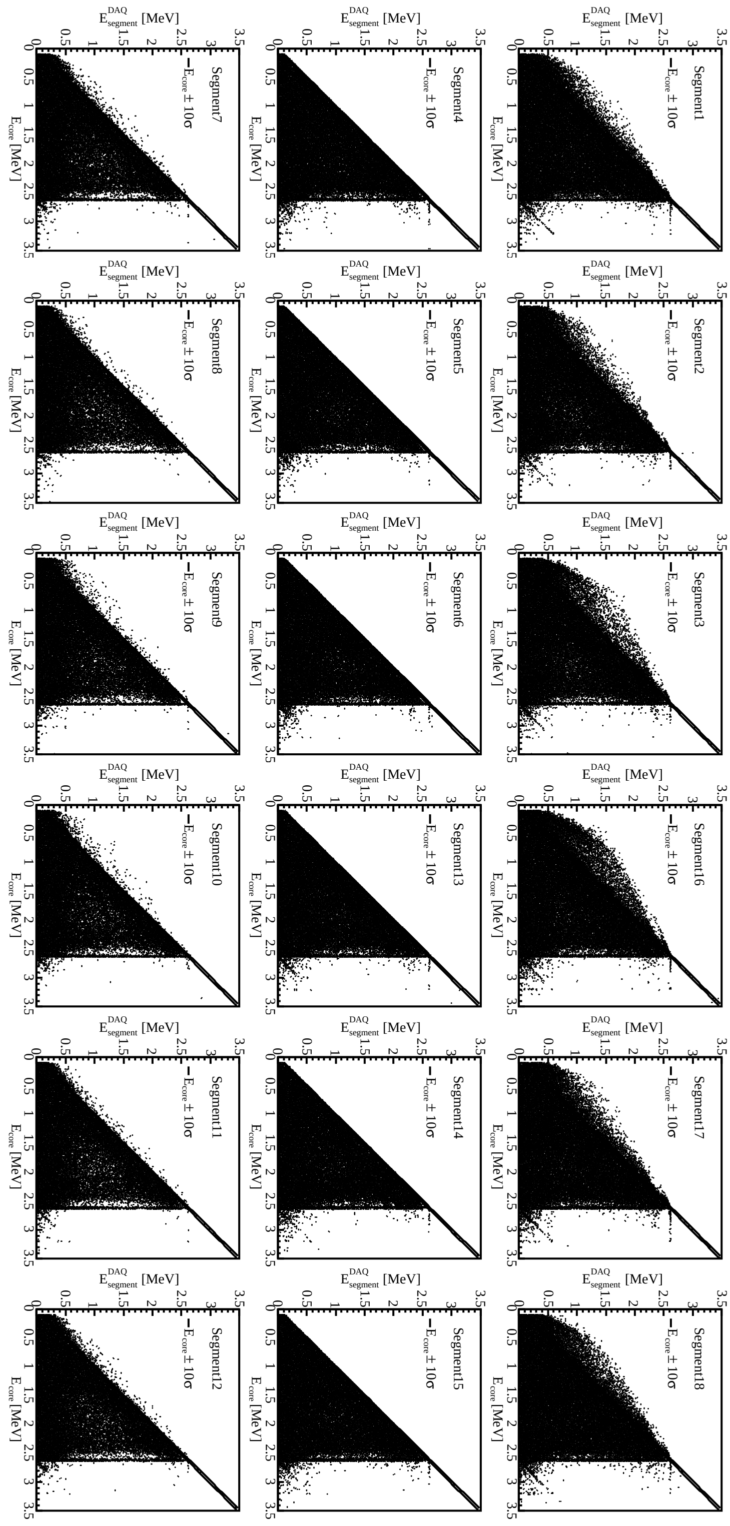

Figure 7.3: Energies of individual segments versus the core energy. All energies were calculated by the DAQ system. The two solid lines in each plot indicate the ±10σ range around the core energy.

Table 7.1: Number of single segment negative pulse events. Given are absolute numbers and the percentage of single segment events they represent.

Top	1	2	3	16	17	18	total
Number (10^3)	88.5 ± 0.3	61.2 ± 0.2	90.7 ± 0.3	133.6 ± 0.4	89.0 ± 0.3	102.7 ± 0.3	565.7 ± 0.8
Percentage (%)	5.34 ± 0.02	5.28 ± 0.02	7.31 ± 0.03	9.24 ± 0.03	5.47 ± 0.02	5.73 ± 0.02	6.34 ± 0.01
Middle	4	5	6	13	14	15	total
Number (10^3)	1.25 ± 0.04	1.15 ± 0.03	0.97 ± 0.03	1.49 ± 0.04	2.15 ± 0.05	1.73 ± 0.04	8.74 ± 0.09
Percentage (%)	0.22 ± 0.01	0.28 ± 0.01	0.21 ± 0.01	0.26 ± 0.01	0.34 ± 0.01	0.24 ± 0.01	0.26 ± 0.01
Bottom	7	8	9	10	11	12	total
Number (10^3)	18.1 ± 0.1	11.5 ± 0.1	15.8 ± 0.1	14.4 ± 0.1	13.2 ± 0.1	17.6 ± 0.1	90.6 ± 0.3
Percentage (%)	3.46 ± 0.03	3.05 ± 0.03	3.69 ± 0.03	2.94 ± 0.02	2.38 ± 0.02	2.79 ± 0.02	3.02 ± 0.01

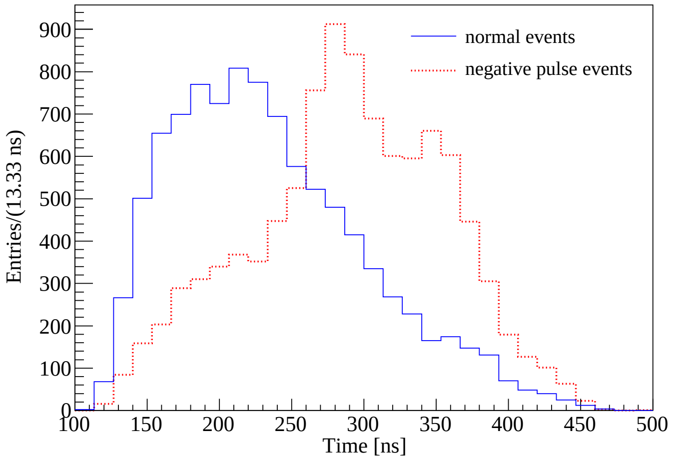

Figure 7.4: Core risetime distribution of normal and negative pulse events.

7.4 Explanation

The end surfaces of true-coaxial detectors have a priori undefined potential. The formation of surface channels [132] and the deformation of the electric field are expected. The charge carriers slow down and might even get trapped near the end surfaces. The trapping of electrons leads to a reduction of the signal both in the core and in the segment containing the hit. However, as the core is mainly sensitive to the drift of the electrons, it is affected stronger than the segment which is mainly sensitive to the drift of holes. As a result a given photon peak in the core energy spectrum would show a large shoulder at lower energies. However, such a shoulder can also occur, if the pulses are just too long, because the DAQ energy filter does not handle extremely long risetimes correctly and calculates an energy slightly smaller than the full energy. Such a shoulder was already observed in data collected with Siegfried I (see Fig. 7.5): the low energy side of the 1332 keV peak from ^{60}Co is significantly higher than in the simulation assuming no field distortion.

If the pulse gets longer and longer; *i.e.*, the field becomes very small, the electrons are effectively trapped and the mirror pulse in a neighboring segment cannot be completed resulting in an effective negative baseline shift; *i.e.*, negative pulse.

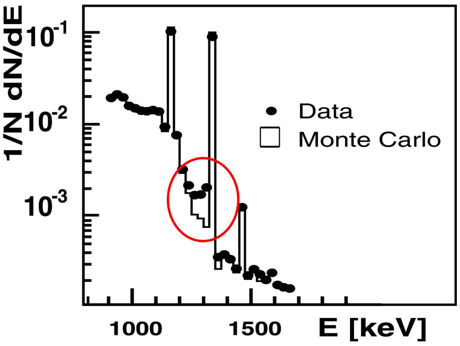

Figure 7.5: A slice of the core energy spectrum around 1332 keV peak taken with Siegfried I. The low energy side of the 1332 keV peak in data is significantly higher than in the simulation.

7.5 Surface investigation

If indeed negative pulse events are located close to the end surfaces of the detector, the low energy part of the spectrum should be especially affected. Figure 7.6 shows the fractions of single segment negative pulse events for all 18 segments versus the core energy as determined by the DAQ system. In all top and bottom segments a rising fraction is seen below 100 keV. Also seen are relatively large fractions just below the 2614 keV photon peak from ^{208}Tl. This would lead to a shoulder in the spectrum as described in the previous section.

The top surface of the detector is illuminated best with low energy photons. The penetration of low energy photons into germanium is shown in Fig. 7.7. Photons with an energy of 20 keV are all absorbed within the first 0.5 mm of the detector. The penetration power of photons increase rapidly with energy. Only about 15% of the 100 keV photons are absorbed there. Thus the fraction of events with negative pulses should rapidly decrease with energy. This is shown in Fig. 7.8 for a top and a middle segment. While the middle segment shows only a very small and statistically uncertain effect the top segment gives a clear indication of a decreasing fraction of events affected. The distribution flattens out at about 100 keV. The fraction of events at this energy is $\approx 5\%$. This corresponds to a penetration of about 200 μm.

Figure 7.9 shows the situation near the ^{208}Tl line at 2614 keV. The negative pulse events show up as a large fraction below the line energy. This enhancement is seen down to about 2400 keV; *i.e.*, up to 200 keV energy can get lost. The fraction of events shifted is about 1%. As the distribution of hits created by 2614 keV photons is basically homogeneous this directly translates into a volume corresponding to a surface layer of $\approx 200\mu$m.

The different approximation indicate that Siegfried II has a surface layer with a thickness of about 200 μm where the electric field is distorted. This is smaller than what was claimed by a previous publication [133]. However, this publication refers to a very different detector. The effect for Siegfried I was much smaller, indicating that it had a thinner layer of field distortion. This is probably due to the fact that Siegfried I has fully metalized segment surfaces while Siegfried II only has relatively small metal contacts.

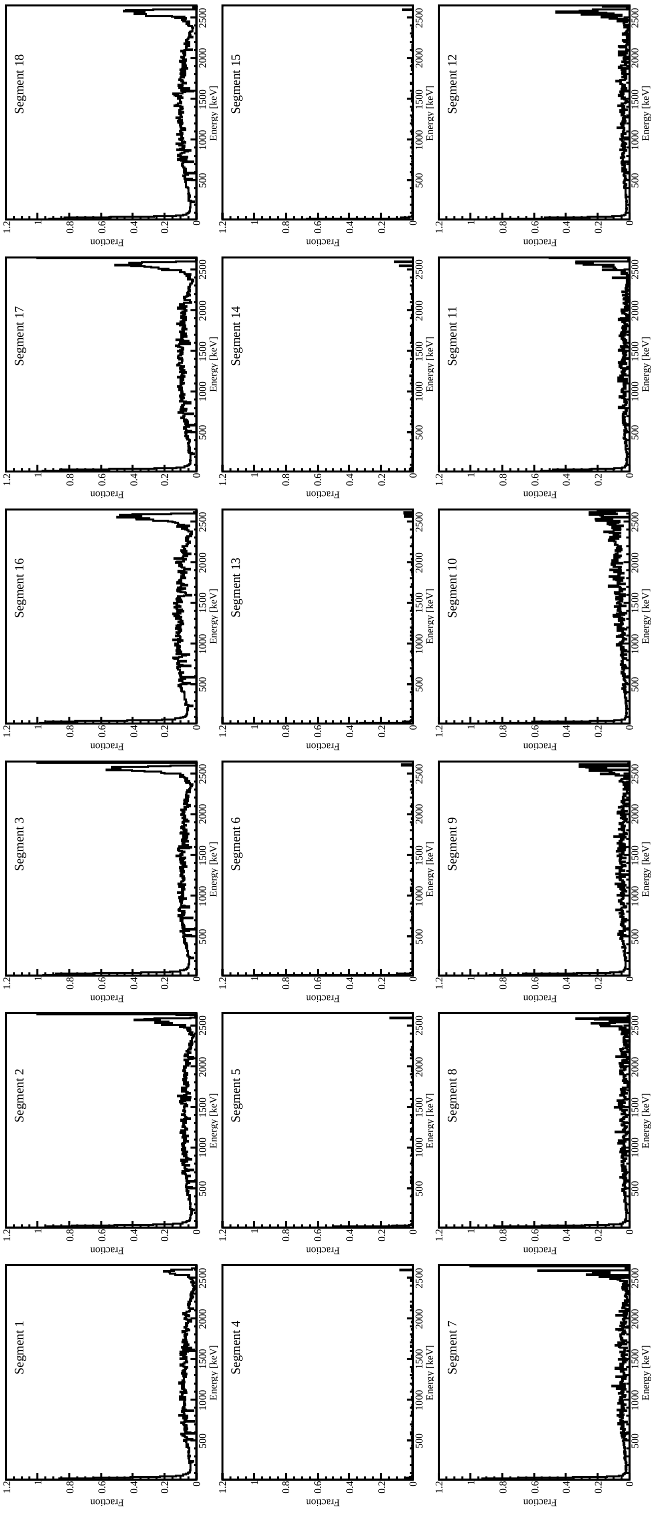

Figure 7.6: Fraction of single segment negative pulse events as a function of core energy in all segments.

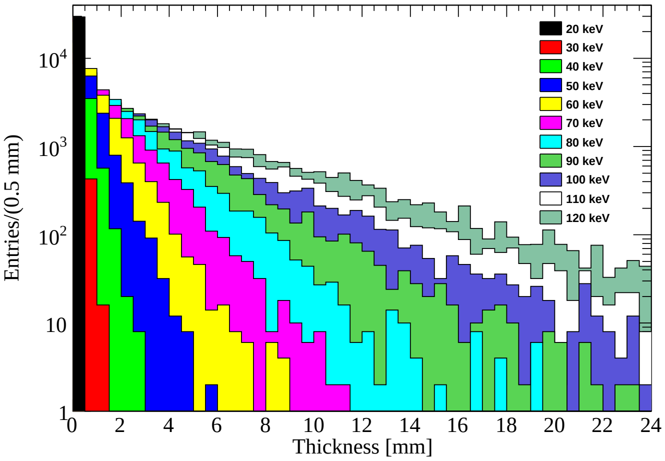

Figure 7.7: Depth distributions of hits created by low energy photons entering the detector from the top.

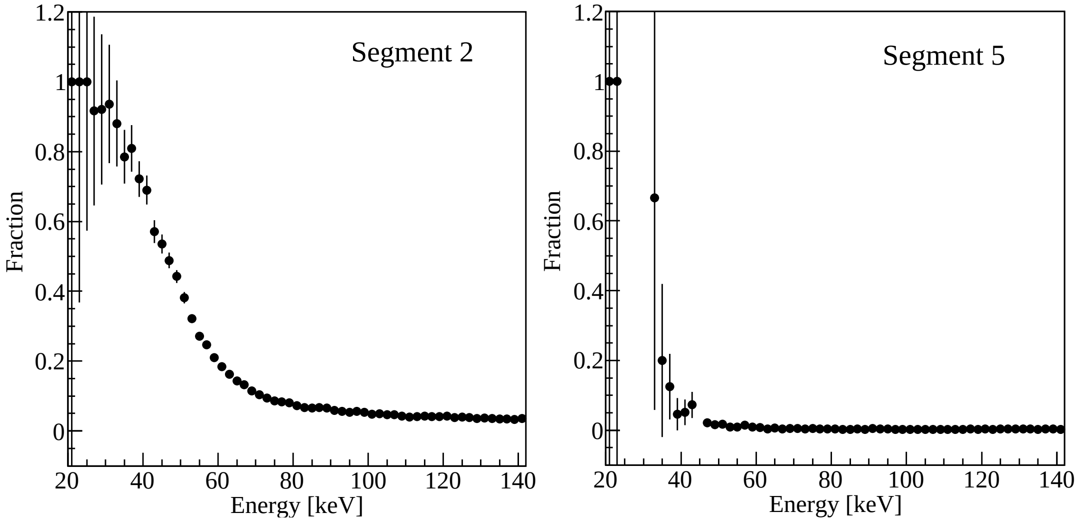

Figure 7.8: Fraction of single segment negative pulse events in the low energy region for segment 2 in the top layer and segment 5 in the middle layer.

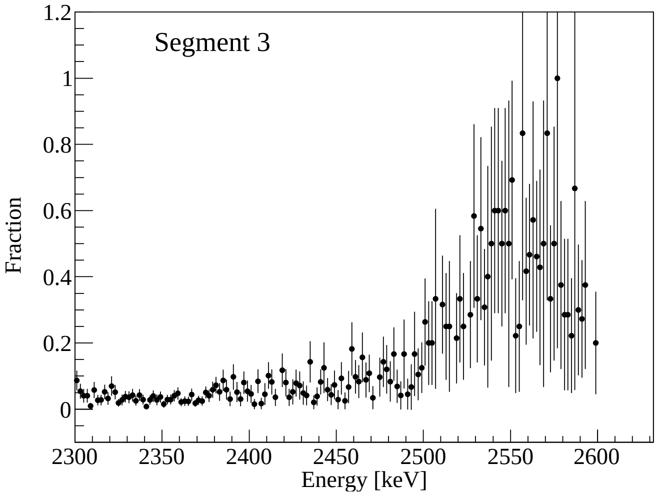

Figure 7.9: Fraction of single segment negative pulse events on the low energy side of 2614 keV peak.

The events can be clearly identified through the pulse shapes. Thus, this can actually be used to define a fiducial volume of the detector and to reject surface events.

7.6 Summary

A special class of events with negative baseline shifts was traced to interactions close to the end surfaces of the detector. The rate of such events for Siegfried II indicates a layer with a distorted electric field of about 200 μm depth. As the events can be clearly identified they can be used to characterize the fiducial volume of a given detector and they can be used to identify surface events. This might be of help in reducing the background from α-sources.

Chapter 8

Photon induced background

Since the $0\nu\beta\beta$ decay of ^{76}Ge has a Q-value of 2.039 MeV, γ-rays with energies larger than 2.039 MeV are the main background source for GERDA. Fortunately, the spatial distribution of photon interactions with germanium differs from electron interactions with germanium, see Sec. 4.1. Segmented germanium detectors are considered for use in GERDA Phase II in order to identify photon induced background. The discrimination power of segmented germanium detectors was examined systematically [134] using the GERDA Phase II prototype detector Siegfried I (see Sec. 3.3.3) and its test stand (see Sec. 5.1.1). The main results are summarized in this chapter.

MaGe [135, 136] is a C++ simulation package co-developed by the Majorana and GERDA collaborations based on Geant4 toolkits [137,138]. It was used for the simulation of GERDA and the detector test facilities in Munich. The predictions for photon induced events were verified to be accurate for a wide range of conditions.

8.1 Event classification

As described in Sec. 4.1.2 a photon with an energy of the order of one MeV has a mean free path of several centimeters in a germanium crystal. It most probably deposits energy in several different places and creates a *multi-site event.* On the other hand, the average range of a 1 MeV electron in germanium is about 0.5 mm (see Sec. 4.1.1). Since the probability for Bremsstrahlung is low, electrons mainly create *single-site events* with most of the energy deposited within a radius of 1 mm. The size of the segments was chosen such that electrons predominantly create *single-segment events* while photons result in *multi-segment events.*

Figure 8.1 depicts four possible event configurations. By requiring anti-coincidence most of the photon induced background events can be rejected. However, there are still some photon induced multi-site events with energy deposits in one segment only, as shown in bottom left corner of Fig. 8.1. This kind of event can be further identified using pulse shape analysis.

A single-site event can also be a multi-segment event if it happens to occur on the boundary of two neighboring segments and induces signals in both segments, as shown in the top right corner of Fig. 8.1. This kind of event will be rejected erroneously by the anti-coincidence requirement, and should also be identified using pulse shape analysis.

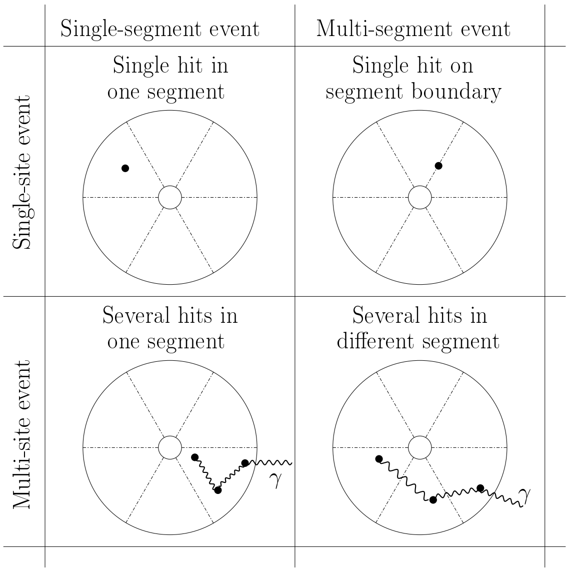

Figure 8.1: Possible event configurations. The cross section of a Siegfried-like detector is depicted. The black dots are hits (energy deposits). The wavy lines indicate γ-rays.

8.2 Background rejection using segmentation

Different data samples were taken using the segmented germanium detector Siegfried I (see Sec. 3.3.3) and its test stand (see Sec. 5.1.1) with ^{228}Th and ^{60}Co γ sources placed 10 cm above the vacuum cryostat (see Fig. 5.1). Figure 8.2 taken from Ref. [134] shows the core energy spectrum of the ^{228}Th data sample for all events (black) and single-segment events (grey). The double escape peak[1] (DEP in short) from ^{208}Tl (1 593 keV) is hardly suppressed since the DEP events are mostly single-segment events; while the ^{212}Bi line (1 620 keV) is suppressed by a factor of 2.85 ± 0.01 since most of the events inside the peak are photon induced multi-segment events.

---

[1] A double-escape-peak event is created as follows: a photon produces a pair of electron and positron inside the detector, the positron losses all its energy and annihilates with another electron resulting in two 511 keV photons, and both of the photons escape from the detector. Since the energy is deposited only by an electron and a positron within a small region, the double-escape-peak event is a single-site event.

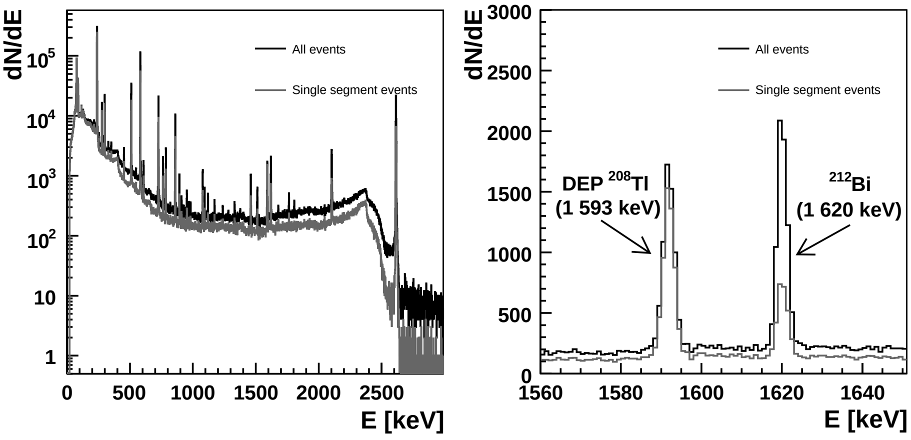

(a) (b)

Figure 8.2: Core energy spectrum of the ^{228}Th source data sample for all events (black) and single-segment events (grey): (a)core spectrum up to 3 MeV and (b) core spectrum around 1.6 MeV.

8.3 Monte Carlo simulation

Monte Carlo (MC) simulations of prototype detectors and their cryostats were performed using MaGe [135, 136], a C++ package co-developed by the Majorana and GERDA collaborations using the Geant4 toolkits [137, 138]. Figure 8.3 shows the geometrical models of the detectors and cryostats implemented in Geant4. Figure 8.3c shows a close-up of Siegfried II. It was modeled in such a way that the details were implemented as close as possible to reality while the speed of simulation did not decrease too much.

The energy deposits of hits in each segment were recorded and the core energy was calculated by adding all segment energies. The segment and core energies were individually smeared according to the energy resolutions of the detectors measured in the individual channels.

The spatial and time information of hits were also recorded and served as parts of the input for the pulse shape simulation package. The geometry of detectors and the voltage bias applied were other input information for the pulse shape simulation. The details of the pulse shape simulation are described in Chapter 10.

8.4 Verification of the Monte Carlo

The simulation of photon interactions was done with Geant4.8.1 patch 2, and verified for (a) the energy spectrum, (b) the occupancy of each segment, namely, the number of events recorded by each segment (see Fig. 8.4 for measurement setup), (c) the multiplicity, namely, the number of segments having signals, and (d) the line suppression factors ($\mathrm{SF_L}$) defined as the ratio of the total number of events to the number of single-segment events

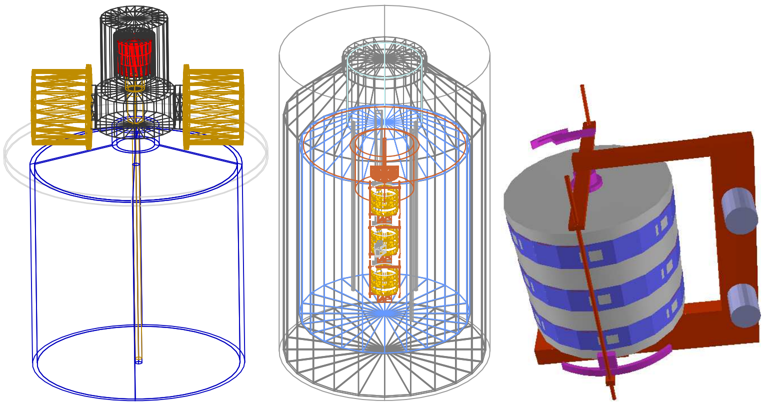
(a) (b) (c)

Figure 8.3: Geant4 models for detectors and their test stands: (a) wire drawing of Siegfried I and its cryostat, (b) wire drawing of GII, and (c) a close-up of Siegfried II with the copper frame as used in GII.

within the energy window $[E_\gamma - 3\sigma, E_\gamma + 3\sigma]$, where E_γ is the central energy of the gamma line and σ is the energy resolution of the line.[2] The simulated distributions of (a), (b) and (c) were added to the background distribution measured, and then compared to the data as shown in Fig. 8.5a, b and c. The line suppression factors were calculated for data and MC, respectively, and then compared to each other as shown in Fig. 8.5d.

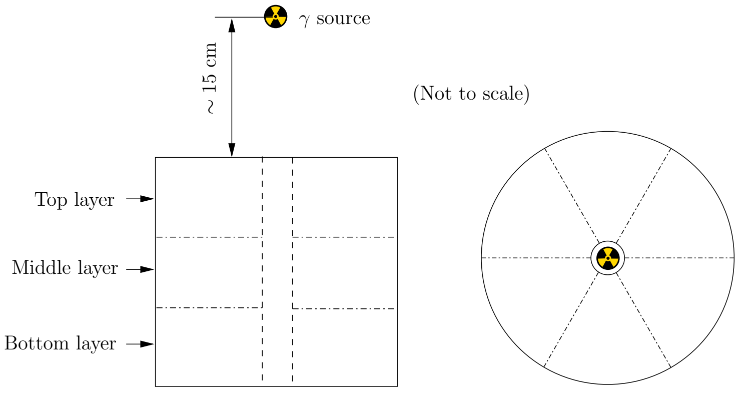

(a) Side view (b) Top view

Figure 8.4: Schematic of experimental setup for occupancy measurement.

The MC simulation agrees very well with the data in general. However, there are some discrepencies observed in different aspects.

---

[2] The suppression factors were calculated after the background was subtracted.

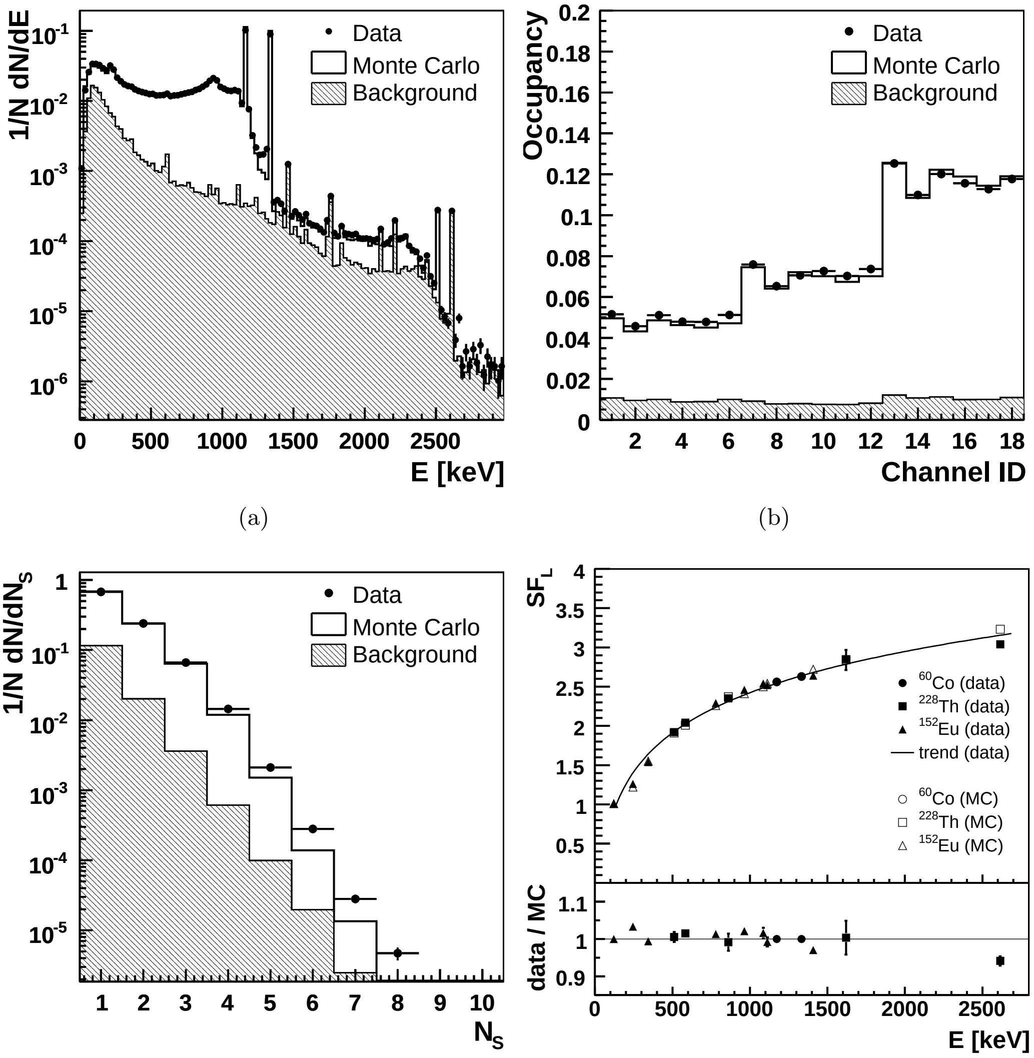

(a) (b)

(c) (d)

Figure 8.5: Comparison between data (dots with error bars) and MC (open histogram) plus background (hatched histogram) for several quantities under study: (a) core energy spectrum, (b) occupancy of all segments, (c) segment multiplicity and (d) suppression factors. Plots are taken from Ref. [134].

As shown in Fig. 8.5a, the low energy side of the 1332 keV peak in the data is significantly higher than in MC. This could be due to the surface channel effect as described in Sec. 7.4.

The occupancy distribution as shown in Fig. 8.5b was measured with the experimental setup shown in Fig. 8.4. The γ source was placed above the center of the detector. Naturally, the top layer of the detector (segment No. 13 - 18[3]) had the highest event rates, the bottom layer (segment No. 1 - 6) had the lowest event rates. The event rates of different segments in the same layer should have been equal because the distance between the source and any of the segments was the same (see Fig. 8.4b). However, this is not the case as shown in Fig. 8.5b. This is because the drift of charge carriers is affected by the structure of the germanium crystal; the drift trajectories do not exactly follow the electric field lines. This effect cannot be simulated using Geant4. An effective model was used to tune the simulated distribution in order to minimize the discrepancy between MC and data. The development of a full simulation of the drift of the charge carriers in germanium detectors is described in Chapters 10 and 11.

There is a deviation of 5% between data and Monte Carlo plus background data for multiplicities up to three. For higher multiplicities the data exceeds the Monte Carlo with increasing multiplicity. This may due to the fact that a hit close to the segment boundary is always assigned to one segment in simulation while in reality it may induce signals in several segment nearby.

---

[3] The segment naming scheme used here is different from that shown in Fig. 3.7 so that segments in the same layer can be plotted aside each other.

Chapter 9

Neutron induced background

Neutrons produced near the germanium detectors by penetrating cosmic-ray muons can induce background events. In addition, neutrons from (α, n) reactions in the surrounding rock are also a potential source of background. The study of neutron interactions with germanium isotopes as well as the surrounding materials is thus of great interest.

It was shown in the previous chapter that segmented germanium detectors are powerful tools to identify photon induced background. In this chapter an investigation whether segment information can also help to identify neutron induced background is presented. It was also shown in the previous chapter that MaGe [135, 136] simulates photon induced background well. The verification of MaGe with respect to neutron interactions is presented in this chapter.

The first GERDA Phase II prototype detector Siegfried I (see Sec. 3.3.3) was exposed to neutrons from an AmBe source to obtain the necessary data.

9.1 Experimental setup and data sets

The schematic of the experimental setup is shown in Fig. 9.1. The detector Siegfried I (see Sec. 3.3.3) was operated in the vacuum cryostat introduced in Sec. 5.1.1. It was exposed to an AmBe neutron source encased in a cylindrical paraffin collimator. The center of the collimator was vertically aligned to the center of the detector and the distance between source and detector center was about 1 m.

The AmBe neutron source had an activity of 1.1 GBq. The energy spectrum of neutrons emitted from $^{9}\mathrm{Be}(\alpha, n)^{12}\mathrm{C}^{*}$ nuclear reaction extends to 12 MeV. High resolution measurements of such neutron energy spectra are presented in Ref. [139, 140]. The emittance of photons from the de-excitation of $^{12}\mathrm{C}^{*}$ is described in Ref. [140].

The front-end electronics and the DAQ system were described in Sec. 5.2.1 and Sec. 5.2.2, respectively. The DAQ system was configured such that if two pulses occurred within 240 ns they were added up to a single signal; if the second pulse occurred 240 ns to 8 μs after the first one, both of them were disregarded. Two different gain factors were chosen for four different measurements. The low gain factor was chosen so that the energy range

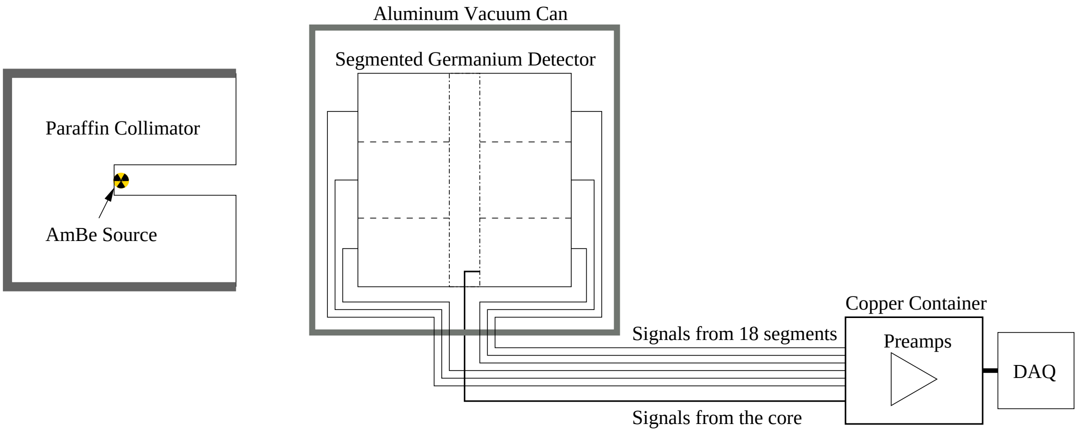

Figure 9.1: Schematic of experimental setup (not to scale).

up to $\sim$ 11 MeV was covered. The high gain factor was chosen for measurements up to $\sim$ 3 MeV. Two measurements were performed with the AmBe source present. They are referred to as HGdat (High Gain data) and LGdat (Low Gain data). In order to determine the background from the laboratory environment two more measurements without the source were performed. They are referred to as HGbg (High Gain background) and LGbg (Low Gain background). The data samples with different gains were combined below 3 MeV. The data sets are listed in Table 9.1.

Table 9.1: Data sets recorded with and without source.

	With AmBe Source		Without AmBe Source	
DAQ Gain	High	Low	High	Low
E_{max} [MeV]	~ 3.5	~ 11	~ 3.5	~ 11
No. of Events	7.1 M	4.7 M	1.5 M	4.7 M
Name	HGdat	LGdat	HGbg	LGbg

9.2 Core spectra

The total energy deposited in the germanium crystal was read out through the core electrode of the detector. Figure 9.2 shows the core energy spectra for data and background in the range of [0.08, 3] MeV. The trigger thresholds were set such that the spectra above 100 keV were not affected.

Figure 9.3 shows the spectra in the range of [3, 10.2] MeV. In this energy range the background is small, as there are hardly any radioactive elements producing photons with such high energies.

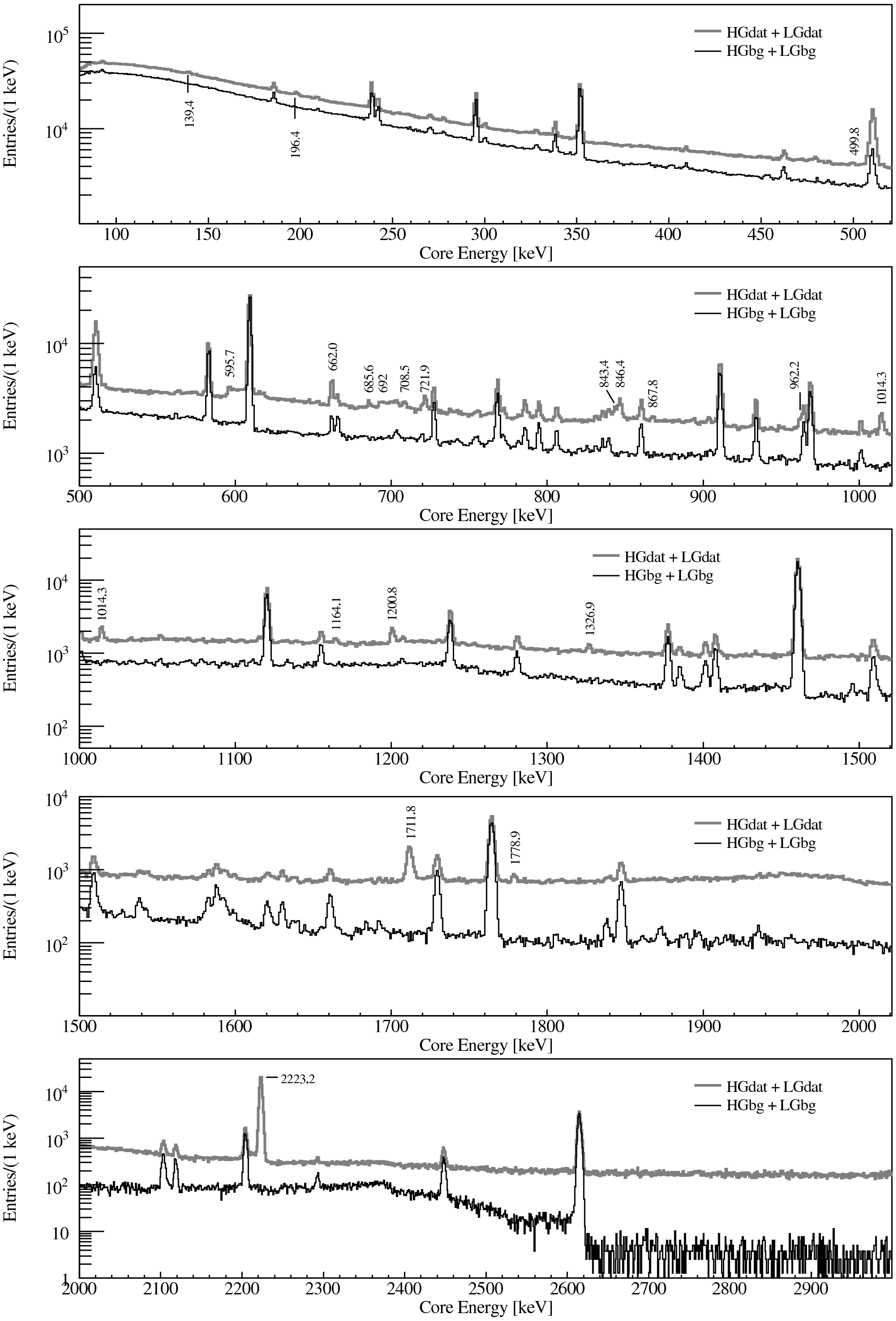

Figure 9.2: Core energy spectra with and without source. The normalization procedure is described in the text. The energy range is [0.08, 3] MeV. Peaks induced by the AmBe source are indicated with their energies in keV.

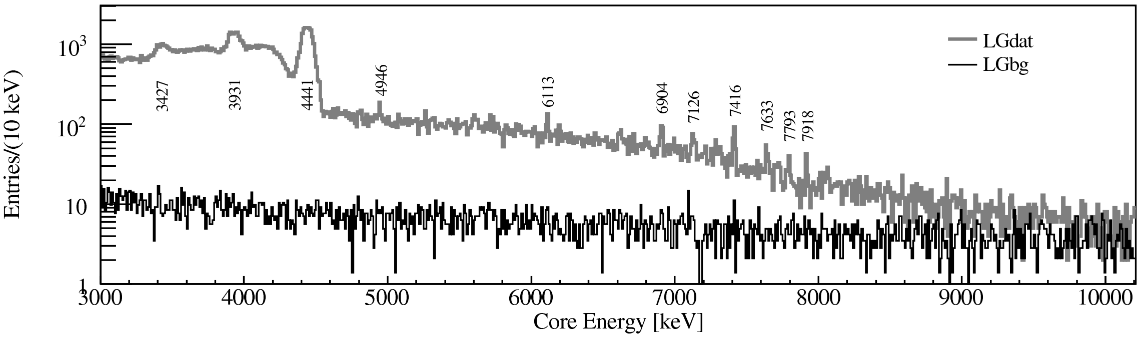

Figure 9.3: Core energy spectra with and without source. The normalization procedure is described in the text. The energy range is [3, 10.2] MeV. Peaks induced by the AmBe source are indicated with their energies in keV.

For Figs. 9.2 and 9.3 the background was normalized using eight photon peaks associated with the decays of ^{214}Pb (352 keV), ^{214}Bi (609 keV, 1120 keV, 1764 keV, 2448 keV), ^{228}Ac (911 keV), ^{40}K (1461 keV), and ^{208}Tl (2615 keV). A Gaussian function plus a first-order polynomial was fitted to each peak in data and background. The ratios of numbers of events in each peak from data and background was taken as scaling factors. The average, 1.279 ± 0.003, was taken as an overall scaling factor to normalize the background spectrum.

To illustrate the neutron interactions more clearly the normalized background was subtracted from the data. The resuling spectrum is shown in Fig. 9.4. Some of the less prominent structures were washed out, since a larger bin width was chosen for statistical reasons.

9.3 Neutron interactions as seen by the core

The main interaction mechanisms of neutrons with energies less than 12 MeV are thermal capture, inelastic and elastic scattering. Elastic scattering does not induce identifiable peaks in the spectrum, because there is no photon emitted and the recoil energy distribution is too broad.

The identification of the observed peaks is complex. Not only is the production mechanism of the excited nucleus important, but the de-excitation mechanism also has to be taken into account. In most cases the nucleus de-excites instantaneously with the emission of one or more photons. However, it can also undergo internal conversion, in which case an electron from a lower shell is emitted instead of a photon. The excited nucleus can also be meta-stable and not de-excite instantaneously.

Table 9.2 lists the processes identified in the core energy spectrum. If inelastic scattering happens inside the germanium crystal, the nuclear recoil energy is recorded as well as the energies from some of the prompt photons. In case of instantaneous de-excitation they are summed up: $E_{inelastic} = E_\gamma + E_{recoil}$. This causes an asymmetric peak with a

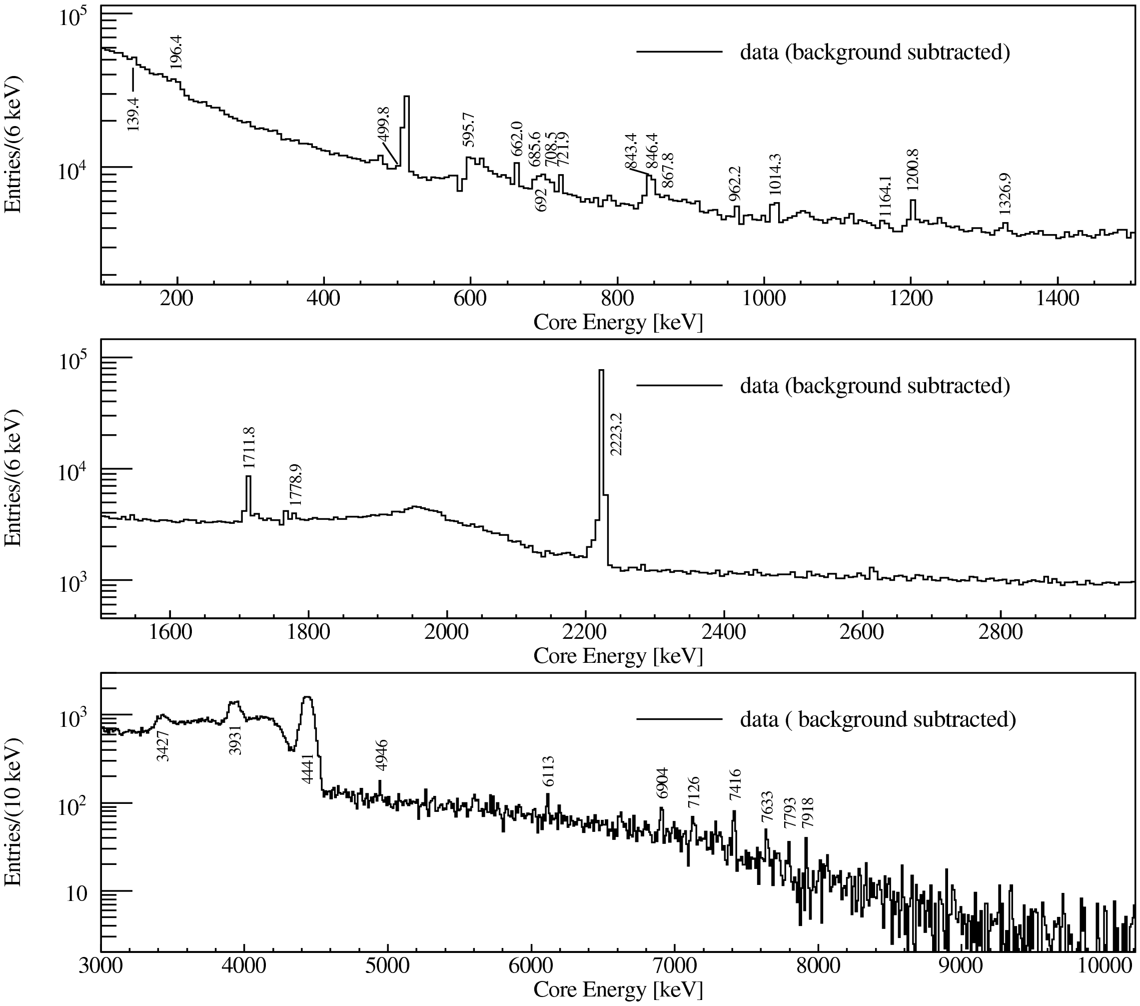

Figure 9.4: Core energy spectra with background subtracted.

long recoil tail on the high energy side. Internal conversions only create identifiable peaks if they occur inside the crystal, otherwise the emitted electrons do not reach the detector.

Table 9.3, 9.4 list all the peaks observed in the core energy spectrum due to neutron interactions within the germanium crystal as well as within the surrounding materials: H, C, Cl in the paraffin collimator, Al, Ce in the aluminum vacuum can and Fe, Cu in the support and the detector and electronics infrastructure.

Purely photon induced peaks were fitted with a Gaussian function plus a first-order polynomial to get the mean energies, FWHMs and the numbers of events in the peaks. The 596 keV peak from ^{74}Ge$(n, n'\gamma)$ inelastic scattering does not have a Gaussian distribution. The treatment of this peak is described in section 9.4. The 662 keV peak associated with ^{140}Ce has a significant background contribution from ^{137}Cs. This was subtracted. The 692 keV peak from ^{72}Ge$(n, n'e)$ is hard to fit because it is asymmetric and broad. It is also

Table 9.2: Types of neutron processes identified in the core energy spectrum.

Production	De-excitation	Symbolic Notation	Short Form
thermal	instantaneous	n+^{A}Z→$^{(A+1)}$Z+γ	^{A}Z(n,γ)
capture	meta-stable	n+^{A}Z→$^{(A+1)m}$Z, $^{(A+1)m}$Z→$^{(A+1)}$Z+γ	^{A}Z(n,γ^{m})
inelastic	instantaneous	n+^{A}Z→^{A}Z+$n' + \gamma$	^{A}Z$(n,n'\gamma)$
scattering	internal conversion	n+^{A}Ge→^{A}Ge$^{+} + n' + e^{-}$	^{A}Ge$(n,n'e)$

contaminated by other peaks nearby. The number of events in this peak was estimated by integration.

The 4.4 MeV peak is due to photons from the de-excitation of ^{12}C* created in the AmBe source by the interaction, ^{9}Be$(\alpha,n)^{12}$C*. It is Doppler broadened because of the movement of the ^{12}C* nuclei. The width of this peak listed in Table 9.4 was determined by the fit. Because of low statistics the widths of most of the peaks above 6 MeV had to be fixed in the fitting procedure according to the detector resolution around these energies. The peaks that are not identified are marked with a question mark.

9.4 Neutron interactions as seen by the segments

The segment energies read out individually provide more information about the interactions inside the germanium crystal than the core signal alone.

9.4.1 Neutron inelastic scattering

A special characteristic of neutron inelastic scattering in a germanium detector is, that not only the photon energy, but also the recoil energy is recorded. The associated peak in the core spectrum has a high energy recoil tail and, hence, is much less significant than a pure photon peak with the same number of events, see Fig. 9.2. It is possible to partially separate out the recoil energy distribution using information from the individual segments. This is due to the way a segmented detector can provide information about event topologies.

Figure 9.5 shows the three types of events contributing to inelastic scattering peaks in the core spectrum. In all cases the scattered neutron escapes:

1. the nuclear recoil energy and the prompt photon energy are deposited in the same segment;

2. the nuclear recoil energy is deposited within one segment, the prompt photon deposits its energy in several other segments;

Table 9.3: Peaks observed in the core energy spectrum below 3 MeV (see Fig. 9.2) due to neutron interactions.

Fitted Energy [keV]	Fitted FWHM [keV]	Interaction Type	Number of Events
139.4	1.6 ± 0.2	^{74}Ge(n, γ^m)	3377 ± 520
197.9	1.9 ± 0.2	^{70}Ge(n, γ^m)	3306 ± 503
499.8	1.9 ± 0.7	^{70}Ge(n, γ)	503 ± 186
595.7[a]	-	^{74}Ge$(n, n'\gamma)$	$(18.4 \pm 2.5) \times 10^3$
662.0[b]	1.9 ± 0.1	^{140}Ce(n, γ)	2802 ± 188
685.6	1.4 ± 0.2	?[c]	628 ± 111
692[d]	-	^{72}Ge$(n, n'e)$	~ 7000
708.5	2.4 ± 0.5	^{35}Cl(n, γ), ^{36}Cl$\rightarrow^{36}$Ar	782 ± 197
721.9	1.9 ± 0.2	?[c]	3502 ± 148
843.4	2.4 ± 0.5	^{27}Al$(n, n'\gamma)$	1558 ± 202
846.6	2.4 ± 0.2	^{56}Fe$(n, n'\gamma)$	2802 ± 196
867.8	1.9 ± 0.5	^{73}Ge(n, γ)	425 ± 129
962.2	2.4 ± 0.2	^{63}Cu$(n, n'\gamma)$	1041 ± 129
1014.3	2.4 ± 0.2	^{27}Al$(n, n'\gamma)$	1958 ± 123
1164.1	2.6 ± 0.5	^{35}Cl(n, γ)	646 ± 140
1200.8	2.8 ± 0.2	DEP[e] of 2223	2318 ± 122
1326.9	2.4 ± 0.2	^{63}Cu$(n, n'\gamma)$	711 ± 91
1711.8	3.8 ± 0.1	SEP[e] of 2223	5555 ± 133
1778.9	2.6 ± 0.2	^{27}Al(n, γ), ^{28}Al$\rightarrow^{28}$Si	469 ± 73
2223.2	3.8 ± 0.1	^{1}H(n, γ)	79349 ± 300

---

[a] The fitting of the 596 keV peak is described in a later section.

[b] The background contribution to the 662 keV peak was subtracted.

[c] Unidentified peaks are marked with a question mark.

[d] The number of events in the 692 keV peak was determined by integration.

[e] SEP, DEP stand for Single Escape Peak and Double Escape Peak, respectively.

3. the nuclear recoil energy is deposited within one segment while the prompt photon deposits its total energy within another segment.

In the first case, only one segment has a signal. The energies recorded by the core and the segment are the same, i.e. $E_{core} = E_{seg} = E_\gamma + E_{recoil}$. Segmentation cannot help to disentangle the two energies. In the second case, the recoil energy can be observed in one segment. As the photon energy is shared between several segments, there is no peaked distribution in any single segment. This could partially be recovered by segment energy summation. In the third case, the recoil energy is observed in one segment, while the photon is observed in another segment. To disentangle the photon peak from the

Table 9.4: Peaks observed in the core energy spectrum above 3 MeV (see Fig. 9.3) due to neutron interactions.

Fitted Energy [keV]	Fitted FWHM [keV]	Interaction Type	Number of Events
3427	85 ± 7	DEP[a] of 4441	2354 ± 263
3931	87 ± 5	SEP[a] of 4441	5873 ± 368
4441	92 ± 2	$^{9}\mathrm{Be}(\alpha, n)^{12}\mathrm{C}^{*}$	14672 ± 297
4946	4.9 ± 1.4	$^{12}\mathrm{C}(n, \gamma)$	68 ± 15
6113	7[b]	$^{35}\mathrm{Cl}(n, \gamma)$	75 ± 12
6904	7[b]	SEP[a] of 7416	60 ± 10
7126	7[b]	?[c]	38 ± 9
7416	7[b]	$^{35}\mathrm{Cl}(n, \gamma)$	70 ± 10
7633	7[b]	$^{56}\mathrm{Fe}(n, \gamma)$	18 ± 10
7793	7.1 ± 2.1	$^{35}\mathrm{Cl}(n, \gamma)$	21 ± 8
7918	6.8 ± 1.4	$^{63}\mathrm{Cu}(n, \gamma)$	29 ± 8

---

[a] SEP, DEP stand for Single Escape Peak and Double Escape Peak, respectively.

[b] The widths were fixed during the fit.

[c] Unidentified peaks are marked with a question mark.

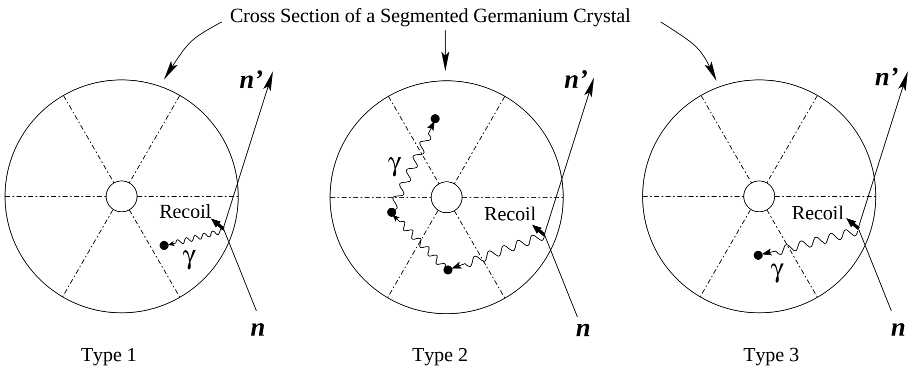

Figure 9.5: Three topologies of neutron inelastic scattering inside a germanium crystal.

recoil energy distribution, 18 energy spectra of all 18 segments are added together[1] to get a spectrum of the energy deposited in *any segment*. In this spectrum, the type 1 events produce the same distribution as in the core spectrum and type 2 events form a flat distribution. Type 3 events, however, create a sharp photon peak and an enhancement in the low energy region from the recoil energy distribution.

Figure 9.6 shows the *any segment* spectrum (black) together with the core spectrum (grey) in the relevant energy ranges. Three peaks at 596 keV, 834 keV and 1039 keV, associated with inelastic scattering, ^{74}Ge$(n, n'\gamma)$, ^{72}Ge$(n, n'\gamma)$ and ^{70}Ge$(n, n'\gamma)$, respectively, are clearly visible in the *any segment* spectrum. The latter two are not observable in the core spectrum.

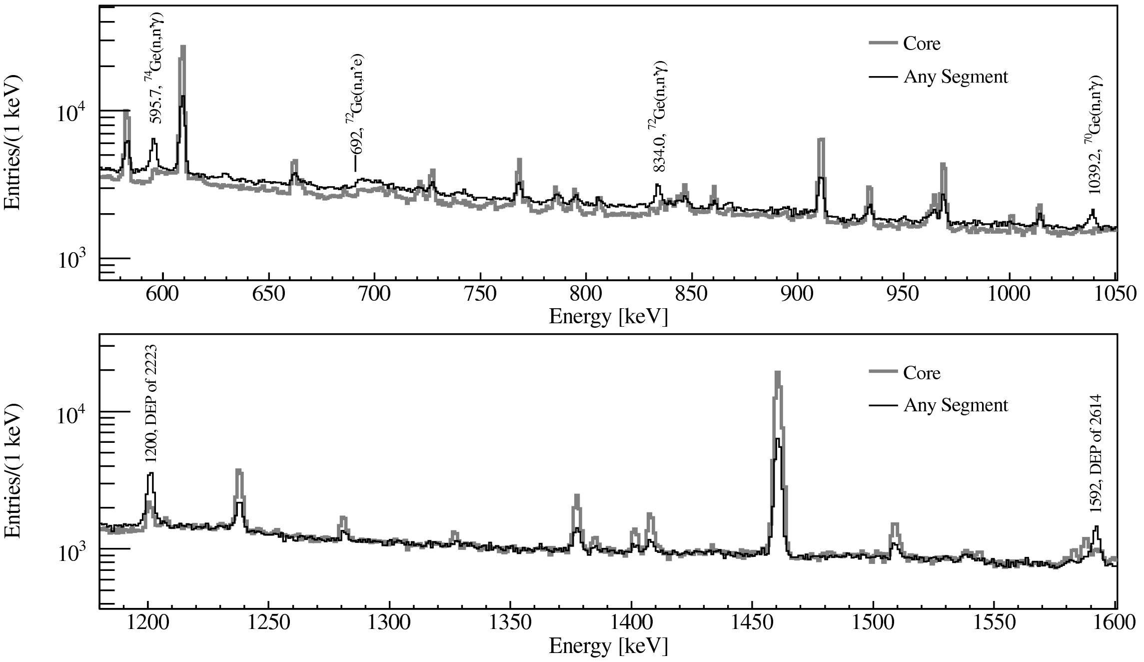

Figure 9.6: The *any segment* spectrum (black) and the core spectrum (grey) in the relevant energy ranges. The disentangled photon peaks are much more significant than the original peaks.

It is possible to extract the number of each type of events in the 596 keV peak. The total number of events, N_{total} was determined from the core spectrum. An exponential function was fitted to the shoulder of the peak associated with the nuclear recoil energy distribution. A Gaussian function was fitted to the 609 keV background photon peak on the shoulder simultaneously. The background below the recoil structure was obtained from interpolating the spectrum below and above the shoulder. The total number of events is the difference between the fitted exponential and the background. The error was estimated

---

[1] Each of the segment provides an energy spectrum. It is the spectra that are added NOT the energies from the segments.

by assuming different levels and shapes of the background. The fit is shown in Fig. 9.7.

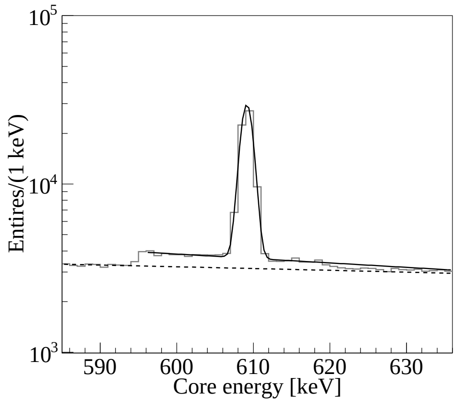

Figure 9.7: Close-up of the 596 keV peak in the core spectrum. The dashed line represents the background, the solid line shows the exponential plus Gaussian function from the background peak at 609 keV. The description of the fitting is given in the text.

The number of type 3 events, N_{type3}, was obtained by fitting a Gaussian function plus a first-order polynomial to the 596 keV peak in the *any segment* spectrum. The small shoulder caused by the contamination with type 1 events does not change the results of the fit significantly.

In principle, the number of type 1 events can be determined by fitting the 596 keV peak in the *single segment* spectrum obtained by requiring only one segment showing a signal. However, a trigger threshold of 5 keV had to be used for each segment in order to avoid electronic noise. Because the recoil energy is often smaller than 5 keV, a lot of type 3 events are recorded as type 1 events. Thus, the 596 keV peak in the *single segment* spectrum contains all the type 1 events and a large part of type 3 events.

Another way to determine the number of type 1 events requires the study of the peaks purely induced by photons. This provides the probability that a de-excitation photon deposits its energy in exactly one or in multiple segments. The relative strength of the peaks in the core and any segment spectrum, that is, $\mathcal{R}(E_\gamma) = N_{core}(E_\gamma)/N_{seg}^{any}(E_\gamma) = (N_{SSE} + N_{MSE})/N_{SSE}$, directly translates to the relative rate of the total number of inelastic scattering events to the sum of type 1 and type 3 events, that is, $\mathcal{R}(E_\gamma^{inelastic}) = N_{total}/(N_{type1} + N_{type3})$.

A Gaussian function plus a first-order polynomial were fitted to eleven of the most prominent photon induced background peaks in the core and *any segment* spectra, respectively. The numbers of events in the peaks from the fits were used to calculate the ratio, $\mathcal{R}(E_\gamma)$, see Fig. 9.8. A second-order polynomial was fitted to get an estimate of the ratio at any energy, $\mathcal{R}(E)$. The number of type 1 events can be calculated as $N_{type1} = N_{total}/\mathcal{R}(E_\gamma^{inelastic}) - N_{type3}$.

The number of type 2 events can then be calculated as $N_{type2} = N_{total} - N_{type1} - N_{type3}$. The results concerning event topologies in the 596 keV peak are listed in the second row of Table 9.5. The percentage of single-segment events, that is, N_{type1}, out of the total number of events is $\mathcal{P} = N_{type1}/N_{total} \approx 5\%$; *i.e.*, most events induced by neutron inelastic scattering with the detector are multi-segment events and can be rejected by requiring only

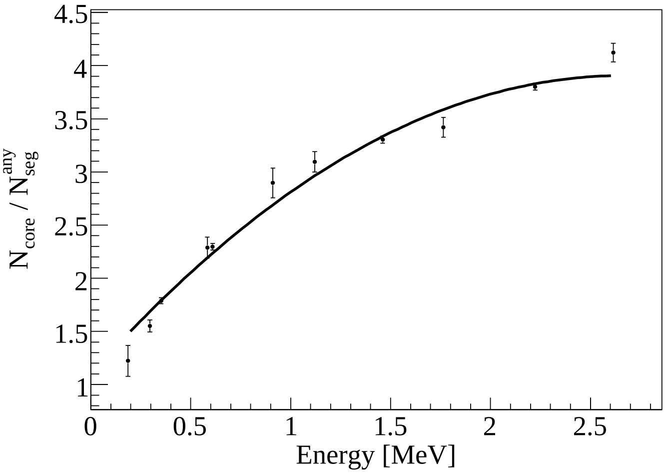

Figure 9.8: The "core to any segment ratio" at the energies of various photon induced peaks. The errors were taken from the fitting of the photon peaks. The line is a second-order polynomial fitted to the data points.

one segment to show energy.

Table 9.5: Numbers of events for different event topologies in the 596 keV, 834 keV and 1039 keV peaks. Two numbers in square brackets indicate the ranges of numbers of events in the 834 keV and 1039 keV peaks.

Energy [keV]	N_{type1}	N_{type2}	N_{type3}	N_{total}
595.8	1000 ± 1000 [a]	$(10 \pm 3) \times 10^3$	7285 ± 218	$(18.4 \pm 2.5) \times 10^3$
834.0	[0, 380]	[4100, 4700]	2592 ± 186	[6700, 7700]
1039.2	[0, 240]	[2700, 3100]	1429 ± 182	[4100, 4800]

[a] The very large error is due to the propagation of errors of N_{type3}, N_{total} and $\mathcal{R}$ according to the relation $N_{type1} = N_{total}/\mathcal{R} - N_{type3}$.

The numbers of type 3 events in the 834 keV and 1039 keV peaks were obtained by fitting the *any segment* spectrum. Since there is no peak at these two energies in the core spectrum, it is impossible to get N_{total} from a fit. However, since the percentage $\mathcal{P} = N_{type1}/N_{total}$ decreases with energy, $\mathcal{P}$ at 834 keV and 1039 keV should be in the range of [0, $\mathcal{P}$(596 keV)]. Taking into account the relation, $N_{type1} = N_{total}/\mathcal{R} - N_{type3}$, the ranges of numbers of events in different topologies in the 834 keV and 1039 keV peaks were calculated.[2] They are listed in Table 9.5 as well.

Special events were selected to disentangle the recoil energy, E_{recoil}, spectrum from

---

[2] The lower and upper limits in the square brackets in Table 9.5 are calculated with $\mathcal{P} = 0$ and $= \mathcal{P}$(596 keV), respectively

the photon of energy, E_γ, spectrum:

1. Exactly two segments with an energy deposit above 10 keV were required.
2. If one segment had an energy deposit in the range $[E_\gamma - 3\sigma, E_\gamma + 3\sigma]$, where σ was the detector energy resolution, the energy deposited in the other segment was used.

The following steps produced the background to the recoil spectra:

1. Exactly two segments with an energy deposit above 10 keV were required.
2. Two energy side-bands, $[E_\gamma - 6\sigma, E_\gamma - 3\sigma]$ and $[E_\gamma + 3\sigma, E_\gamma + 6\sigma]$ were defined.
3. If one segment had an energy deposit in the side-bands, the energy deposited in the other segment was used.

Figure 9.9 shows the disentangled recoil spectra related to the 596 keV, 834 keV and 1039 keV photon peaks. The histograms start at 10 keV. Below, the spectra are dominated by electronic noise. The recoil spectra extending to $\approx$ 100 keV are clearly visible above the background.

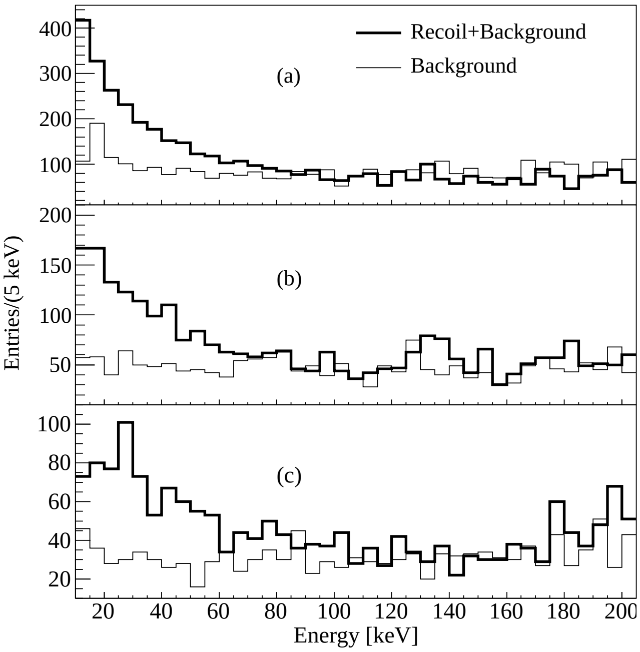

Figure 9.9: Measured recoil energy spectra of inelastic neutron scattering with prompt photons of energies of (a) 596 keV, (b) 834 keV and (c) 1039 keV.

9.4.2 Internal conversion

If the excited state of a nucleus has the same spin as the ground state, internal conversion [141, 142] is the predominant mode of the de-excitation. Since the mean free path of an electron emitted from internal conversion is about 1 mm in germanium, the energy of the electron and the recoil of the nucleus are deposited in the same segment. The core and the *any segment* spectra are the same. This is demonstrated in Fig. 9.6. The 692 keV peak from internal conversion, $^{72}\mathrm{Ge}(n, n'e)$, is neither changed nor suppressed in the *any segment* spectrum.

9.4.3 Double escape peaks

The photons from neutron induced interactions can subsequently induce double escape events in pair production. The double escape peaks are enhanced in the *any segment* spectrum, because many events from the single escape and full energy peaks in the core spectrum move to this peak. Two enhanced double escape peaks at 1200 keV and 1592 keV are clearly visible in Fig. 9.6. The peak at 1200 keV originates from the 2223 keV peak of $^{1}\mathrm{H}(n, \gamma)$ thermal capture. The 1592 keV peak originates from the 2614 keV peak of $^{208}\mathrm{Tl}$; This is not a neutron induced interaction.

9.5 Verification of simulation

The Geant4 [137, 138] based simulation package MaGe, as described in Sec. 8.3, was used to simulate the experiment. The version Geant4 8.2 with patch-01 was used.

9.5.1 Generator, geometry and physics processes

The neutron spectrum of an AmBe source taken from Fig. 5 in Ref. [139] was normalized to a probability density function and used in the neutron generator to assign energies to the outgoing neutrons. The generator also produced 4.4 MeV photons from the $^{12}\mathrm{C}^*$ de-excitation inside the AmBe source. The Doppler broadening of the 4.4 MeV peak was simulated by Gaussian smearing with the observed widths taken from Table 9.4.

The geometry of the experiment was implemented according to the technical drawings. Approximations up to several centimeters had to be made regarding

- the shape and size of the AmBe source and how it was held inside the paraffin collimator,
- the exact relative positions of the crystal and the paraffin collimator,
- the exact geometry of the components inside the cryostat.

Geant4 provides high precision models for the simulation of interactions of neutrons with energies below 20 MeV [137, 138]. The models rely on the "evaluated neutron data library" (G4NDL) for cross sections, angular distributions and final state information. The version G4NDL3.10 was used.

9.5.2 Core spectrum

Figure 9.10 shows the simulated core energy spectrum. The threshold effects below 100 keV were not taken into account in the simulation. Figure 9.11 compares the simulation with the measurement in the range of [0.1, 3] MeV. The background was normalized to data as described in section 9.2. The simulation was normalized to data according to the relation, $N_{data} = N_{background} + N_{signal} = N_{background} + N_{simulation}$, where the Ns are the event numbers in the data, background and simulated spectra. Figure 9.12 shows the same spectra in the range of [3, 10.2] MeV.

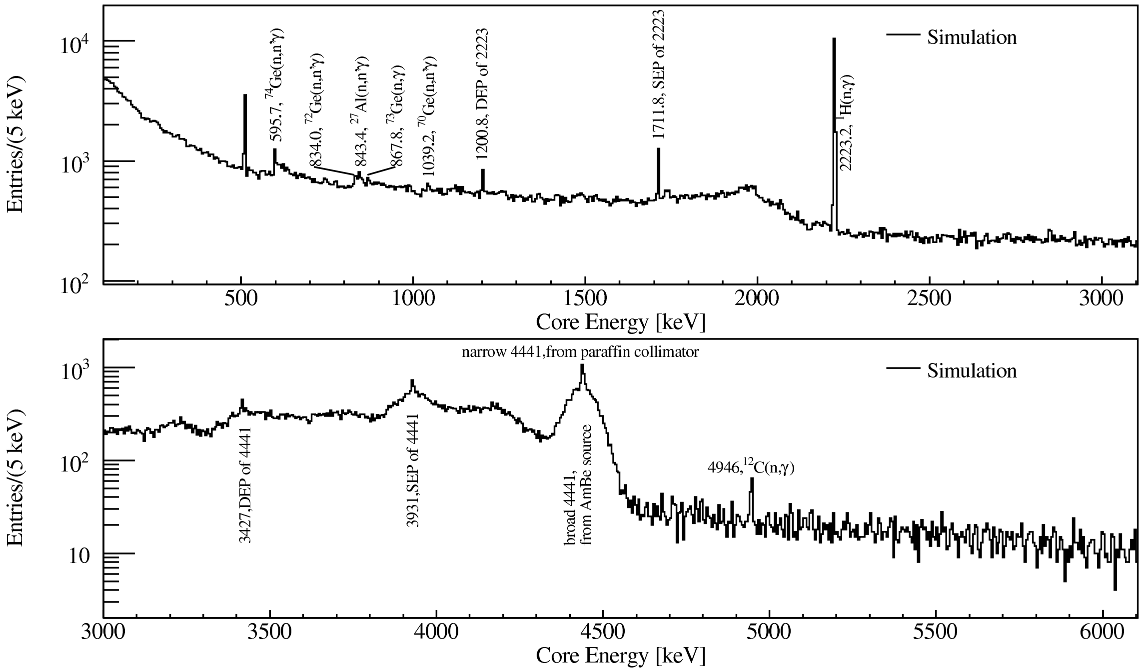

Figure 9.10: Simulated core energy spectrum from 0.1 MeV to 6.1 MeV.

9.5.3 Discrepancies between data and simulation

In general the simulation describes the data very well. Some discrepancies are discussed here.

The shapes of the continuous spectra from the simulation and data above ≈ 1.5 MeV deviate due to the poor knowledge of the exact material and geometry of components between the source and the crystal.

There is a known bug [143] in Geant4 concerning neutron inelastic scatterings. The secondary particles are not boosted back to the laboratory frame after the calculations in the center of mass frame are completed. This causes two problems:

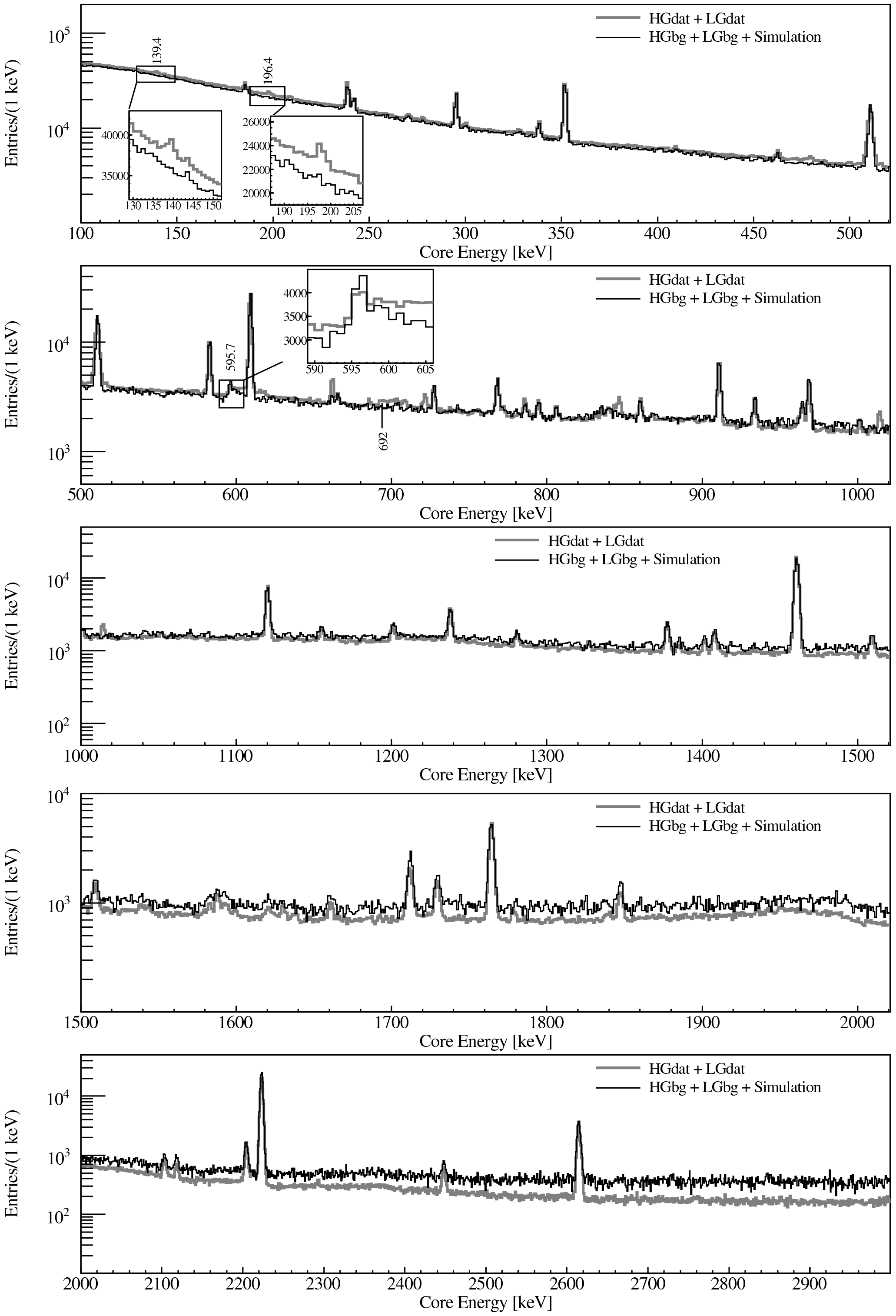

Figure 9.11: Comparison of the neutron core energy spectrum from 0.1 MeV to 3 MeV between data and simulation plus measured background.

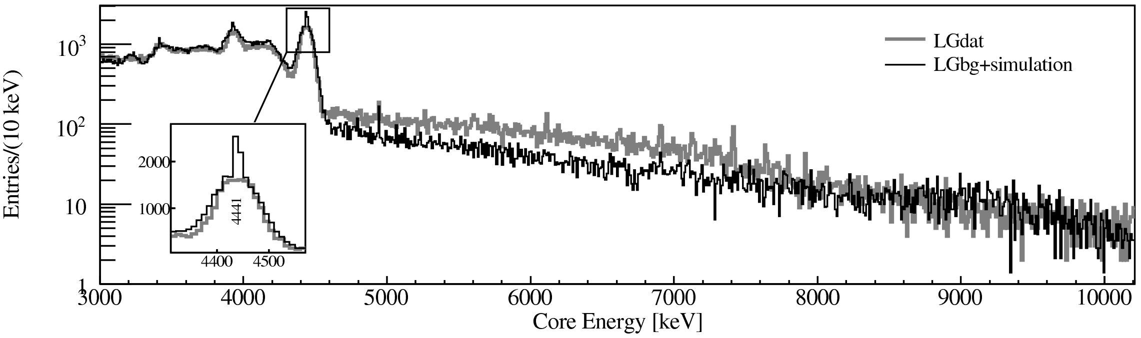

Figure 9.12: Comparison of the neutron core energy spectrum from 3 MeV to 10.2 MeV between data and simulation plus measured background.

- The simulated recoil energies of the germanium nuclei are wrong.
- The photon peaks from these interactions are not broadened.

The first effect is demonstrated in the third inset of Fig. 9.11. The measured 596 keV peak from ^{74}Ge$(n, n'\gamma)$ has a long tail on the high energy side due to the nuclear recoil while the simulated peak misses this feature.

The second effect is demonstrated by the inset of Fig. 9.12. The simulation generates a broad and a narrow peak, both at 4.4 MeV. The broad peak is due to the de-excitation of ^{12}C* created in the source. The generator was adjusted to describe the data. The narrow one is due to neutron inelastic scattering on carbon atoms in the paraffin collimator, ^{12}C$(n, n'\gamma)$. In reality, the carbon atom can gain a velocity of up to $0.02c$ causing a Doppler broadening of the order of 50 keV-100 keV. This is comparable to the broadening in the ^{12}C* de-excitation peak, and can, thus, not be resolved in the measured spectrum.

Another problem was observed in connection with the ^{1}H(n, γ) photon peak of 2223 keV. The mean value from a Gaussian fit to this peak is (2223.24 ± 0.01) keV. The simulated peak centers at (2224.61 ± 0.01) keV. This shifted value comes from the evaluated neutron data library. The problem was reported to the Geant4 Problem Tracking System [144]. It was fixed for our studies by correcting the value in the database. The result is shown in Fig. 9.13.

The 139 keV and 196 keV photon peaks from the meta-stable states of ^{75}Ge and ^{71}Ge produced by neutron capture are missing in the simulated neutron spectrum, see the first two insets of Fig. 9.11. This problem has been reported to the Geant4 Problem Tracking System [145].

The 692 keV peak from internal conversion, ^{72}Ge$(n, n'e)$, is also missing in the simulation, see Fig. 9.11. Again, this was reported [146].

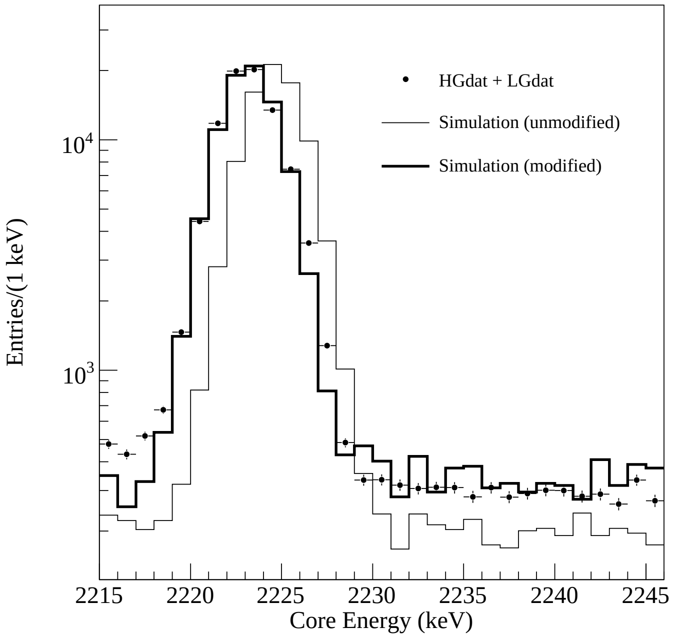

Figure 9.13: The 2223 keV photon peak from ^{1}H(n, γ) in data and simulation. The spectra were normalized according to the numbers in the photon peaks. The simulated peak was shifted to 2224.6 keV before the modification described in the text.

9.6 Summary

The 18-fold segmented germanium detector, Siegfried I, was exposed to an AmBe neutron source and spectra were taken. A number of peaks from neutron interactions on germanium isotopes as well as the surrounding materials were identified. It was proven that neutron inelastic scattering mainly produces multi-segment events which can be rejected by requiring only one segment showing energy. The segment information was proven to be very helpful in identifying peaks induced by neutron inelastic scattering, hence can be used to improve our understanding of the background for GERDA.

The Geant4 based simulation package, MaGe, was used to simulate the experiment. While the description was in general very good, several discrepancies between data and MC were found. Most of them were corrected. Some further verification and improvement of the related Geant4 codes are needed.

Chapter 10

Pulse shape simulation

How segmentation can be used to distinguish between single- and multi-segment events and how to use this information was described in chapters 8 and 9. However, as was shown in Fig. 8.1, (1) there are some multi-site events which are confined to one segment and (2) there are some single-site events that happen on the boundary between two segments. If the signal is identified with single-segment events, events from category (1) are counted erroneously as signal and events from category (2), *boundary events*, are rejected erroneously, because the energy deposited is shared between segments.

The analysis of the electrical pulses associated with the events (pulse shape analysis) can help with both problems[1]. For category (1) the time development of the pulse can reveal a multi-site event while for events in category (2) a close to equal strength and time development of the two pulses can reveal its true single-site structure. Concerning (1), previous studies [119] indicate that pulse shape analysis can provide an extra suppression factor of 1.3 beyond the suppression achieved through segment information alone. These studies were limited by the lack of knowledge about the development of the pulses in the detector and the electronic system.

Pulses resembling the ones expected for the $0\nu\beta\beta$ signal are usually collected using photon induced events with a similar event topology. Two data samples commonly used are (A) double escape peak (DEP) events and (B) single Compton scattering events [149]. However, the double escape peaks are normally not located near the Q-value of ^{76}Ge $0\nu\beta\beta$ decay. In addition, the events from the peak are not uniformly distributed throughout the detector crystal [150]. Events from single Compton scattering could, in principle, be selected to overcome these restrictions. However, it is intrinsically difficult to collect large such samples. Therefore, it is essential to supplement the data with simulated pulses from a reliable simulation.

The physics models used for the drift of electrons and holes inside germanium crystals were established by L. Mihailescu *et al.* [153] and B. Bruyneel *et al.* [156], respectively. The implementation of these models for Siegfried-like detectors is described in detail in

---

[1] Pulse shape analysis can also help with several other aspects: rejection of background from α-particle and neutron interactions with detectors, Compton continuum suppression [147], detection of crystal structure [148], etc.

this chapter.

10.1 Procedure

The procedure to simulate pulse shapes [148] is as follows:

1. Simulate the interactions of particles with germanium using Geant4 to get the spatial distribution and the energy deposits of the interactions (hits);
2. Group hits if they are closer to each other than 1 mm. The position of the new hit is the barycenter of the energies of the original hits. The energy of the new hit is the sum of the energies of the original hits.
3. Calculate the number of electron-hole pairs, n, created by the hit with energy E_{hit}: $n = E_{\mathrm{hit}}/E_{\mathrm{pair}}$, where the pair energy $E_{\mathrm{pair}} = 2.95$ eV;
4. Get the electric field and the weighting potentials by interpolating values at the neighboring grid points. The grid is calculated once beforehand according to the high voltage applied and the spatial distribution of the impurity. [127, 128, 129]
5. Calculate the drift velocities of the charge carriers taking into account the effect of the crystal structure;
6. Calculate the trajectory of the drift from the interaction point to the boundary of the crystal;
7. Calculate the time development of the charges induced in the electrodes, namely, the pulses [151]. A dominant pulse is seen in the electrode of the segment hit. However, other electrodes also show pulses, so called mirror pulses, which also have to be simulated.
8. Add to the simulated pulses the effects from the electronics such as noise, bandwidth limit, and shaping, etc.

MaGe, the object-oriented simulation package co-developed by the GERDA and Majorana MC groups described in Sec. 8.3 covers the complete procedure. Step 5-7 were developed as part of this thesis. The calculation of the electric fields and potentials is described in Sec. 10.2, the calculation of the drift velocities of the charge carriers in Sec. 10.3.

10.2 Electric and weighting fields

The electric field $\mathbf{E}$ could, in principle, be calculated by solving analytically Poisson's equation $\nabla \cdot \mathbf{E} = \frac{\rho}{\epsilon}$ as described in Sec. 4.3.2. It is more practical to numerically calculate the potential field φ. The electric field $\mathbf{E}$ is then obtained using $\mathbf{E} = -\nabla\varphi$. Since true coaxial detectors are used, it is convenient to use cylindrical coordinates, r, ϕ, z:

$$\frac{1}{r}\frac{\partial\varphi}{\partial r} + \frac{\partial^2\varphi}{\partial r^2} + \frac{1}{r^2}\frac{\partial^2\varphi}{\partial\phi^2} + \frac{\partial^2\varphi}{\partial z^2} = -\frac{1}{\epsilon_0\epsilon_R}\rho, \tag{10.1}$$

where φ and ρ are functions of r, ϕ, z; ϵ_0 and ϵ_R are the dielectric constants in vacuum and germanium, respectively.

The electric field distribution inside the germanium crystal is quite sensitive to the impurity density. Figure 10.1 shows the strength of the electric field as a function of r with the bias voltage fixed at 3 kV. A change of the impurity density by one order of magnitude changes the electric field dramatically. Even a factor three difference, usually allowed between top and bottom for a commercial detector, has a very significant effect.

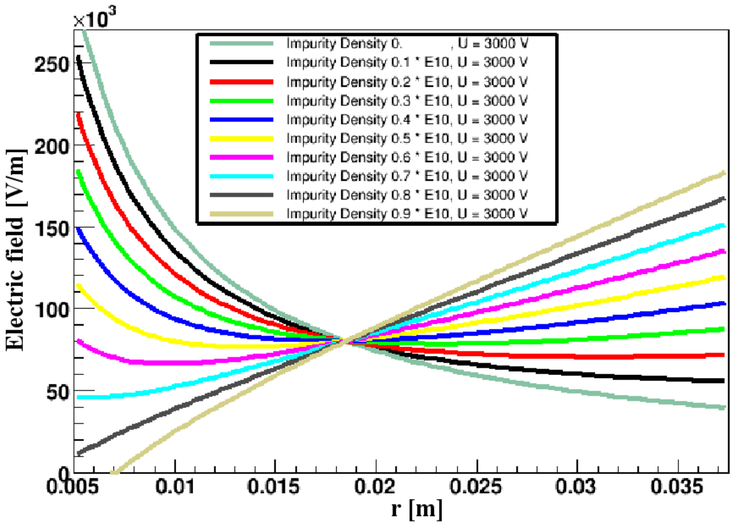

Figure 10.1: Strength of the electric field as a function of the cylindrical coordinate r for impurity densities between 0 and $0.9 \times 10^{-10}/\mathrm{cm}^3$.

The weighting fields and potentials are calculated in the same way to determine the signals induced in the electrodes using Shockley-Ramo's Theorem [127,128,129] as described in Sec. 4.4.

10.3 Drift of charge carriers

10.3.1 Mobility

The electrons and holes drift to the electrodes of the detector. The mobilities of electrons μ_e and holes μ_h as defined in Sec. 4.3.3 change with the temperature of the germanium crystal. If the temperature of electrons and holes[2] do not differ much from the temperature of the crystal lattice, the drift velocity $\mathbf{v}_{e/h}$ is simply proportional to the electric field and the crystal structure has no influence. The mobility in this case is just a number,μ_0. As germanium detectors are operated at ≈ 100 K, the electrons and holes are hotter than

---

[2] If the velocities of a group of electrons or holes follow a Maxwell-Boltzmann distribution, their temperature is defined as the temperature of that distribution.

the crystal lattice. The mobility in this case depends on the crystal orientation and is a complex tensor. The drift trajectory, hence, is not always parallel to the electric field.

Germanium has the same crystalline structure as silicon and diamond, *i.e.* a face-centered cubic (FCC) structure: each atom is at the center of a regular tetrahedron and is surrounded by four atoms as shown in Fig. 10.2. Also shown is the definition of crystal axes in terms of the Miller index.

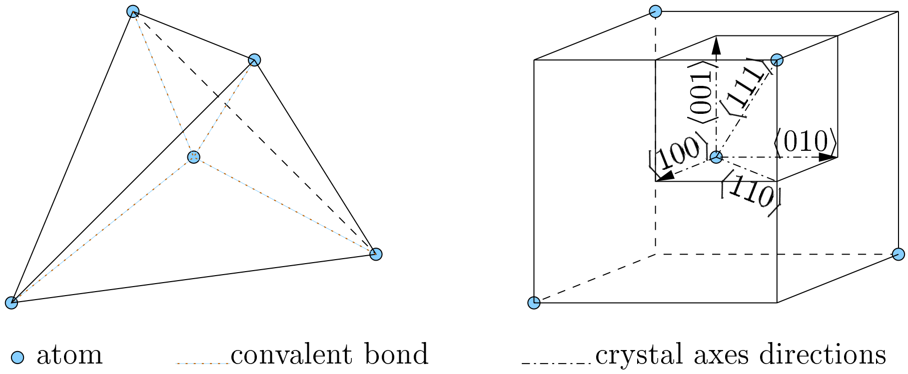

Figure 10.2: Structure of germanium crystals: (a) basic configuration and (b) definition of crystal axes.

If the electric field lines are parallel to any of the three principal crystallographic axes ⟨100⟩, ⟨110⟩ and ⟨111⟩, the charge carriers will drift along the electric field because of the symmetric structure of the germanium crystal. In this case the drift velocity only depends on the strength of the electric field. Measurements of the drift velocities along the axes ⟨100⟩ and ⟨111⟩ with electric field parallel to them were performed and the data can be fitted well by the following parametrization [152]:

$$v = \frac{\mu_0 E}{[1 + (\frac{E}{E_0})^{\beta}]^{1/\beta}} - \mu_n E, \tag{10.2}$$

where E, v are the magnitudes of the electric field and drift velocity, respectively, μ_0, μ_n, E_0 and β are parameters to be determined by fitting. The parameter μ_0 represents a simple linear relation between v and E. A deviation from this linear relation occurs at low temperatures (≈100 K). It is modeled through the parameters E_0 and β. Mihailescu *et al.* [153] added the term $\mu_n E$ for electric fields stronger than 300 V/mm to account for the *Gunn effect* observed by Ottaviani *et al.* [154]. This effect is irrelevant here as our detectors are operated at field strengths well below 300 V/mm. The values of the parameters of the fit to the experimental data are listed in Table 10.1. They are an important input for the simulation presented here.

Figure 10.3 shows the drift velocities of electrons (a, c) and holes (b, d) along the principal crystal axes as functions of electric field in the range of [7,500] V/mm. The drift velocities along the ⟨100⟩ and ⟨111⟩ axes were calculated according to Eq. 10.2. The input

Table 10.1: Parameters for the experimental drift velocities in the ⟨111⟩ and ⟨100⟩ directions (taken from Ref. [156]).

Reference	Carrier	Direction	$\mu_0 \left[\frac{\text{cm}^2}{\text{V}\cdot\text{s}}\right]$	$E_0 \left[\frac{\text{V}}{\text{mm}}\right]$	β	$\mu_n \left[\frac{\text{cm}^2}{\text{V}\cdot\text{s}}\right]$
Ref. [153]	Electrons	⟨111⟩	42420	25.1	0.87	62
		⟨100⟩	40180	49.3	0.72	589
Ref. [155]	Holes	⟨111⟩	107270	10.0	0.58	0
		⟨100⟩	66333	18.1	0.744	0
Ref. [156]	Electrons	⟨111⟩	38536	53.8	0.641	510
		⟨100⟩	38609	51.1	0.805	-171
	Holes	⟨111⟩	61215	18.2	0.662	0
		⟨100⟩	61824	18.5	0.942	0

parameters provided in Ref. [153] and [155] ([156]) were used for Fig. 10.3a and b (c and d). The drift velocity in any direction can be derived from the velocities along the ⟨100⟩ and ⟨111⟩ axes. The details of the calculation are described in the following sections.

10.3.2 Coordinate systems

Two different coordinate systems are important for the calculation. The first one is defined by the crystal axes ⟨100⟩, ⟨010⟩ and ⟨001⟩. The second one, indicated as xyz in Fig 10.4, is used in Geant4. The cylindrical detectors are produced with their geometrical middle axis, z, aligned to the crystal axis ⟨001⟩. The transformation between the two coordinate system, hence, only depends on the angle between the ⟨110⟩ and the y-axis, ϕ_{110}.

10.3.3 Electron drift velocity

The conduction band in a germanium crystal reaches its minimal potential in regions around the four equivalent ⟨111⟩ axes. The equipotential surfaces in these regions have ellipsoidal shapes as shown in Fig 10.5. These regions are characterized by valleys in the conduction band which can easily be populated by free electrons. The electrons have a high mobility and are strongly accelerated by the electric field applied. The probability density of conduction band electrons in other regions is very small. If it is neglected, the dependence of the electron drift velocity $\mathbf{v}_e$ on the applied electric field $\mathbf{E}$ can be written as

$$\mathbf{v}_e(\mathbf{E}) = \mathcal{A}(E) \sum_j \frac{n_j}{n} \frac{\gamma_j \mathbf{E_0}}{\sqrt{\mathbf{E_0}^T \gamma_j \mathbf{E_0}}}, \text{ with } j = 1, 2, 3, 4, \tag{10.3}$$

where the coefficient $\mathcal{A}$ is a function of $E = |\mathbf{E}|$ and the temperature; $\mathbf{E_0}$ is the normalized electric field vector; n_j/n is the fraction of the carriers (in this case, electrons) in the j-th ⟨111⟩ valley and γ_j is the effective mass tensor for the electrons in the j-th ⟨111⟩ valley.

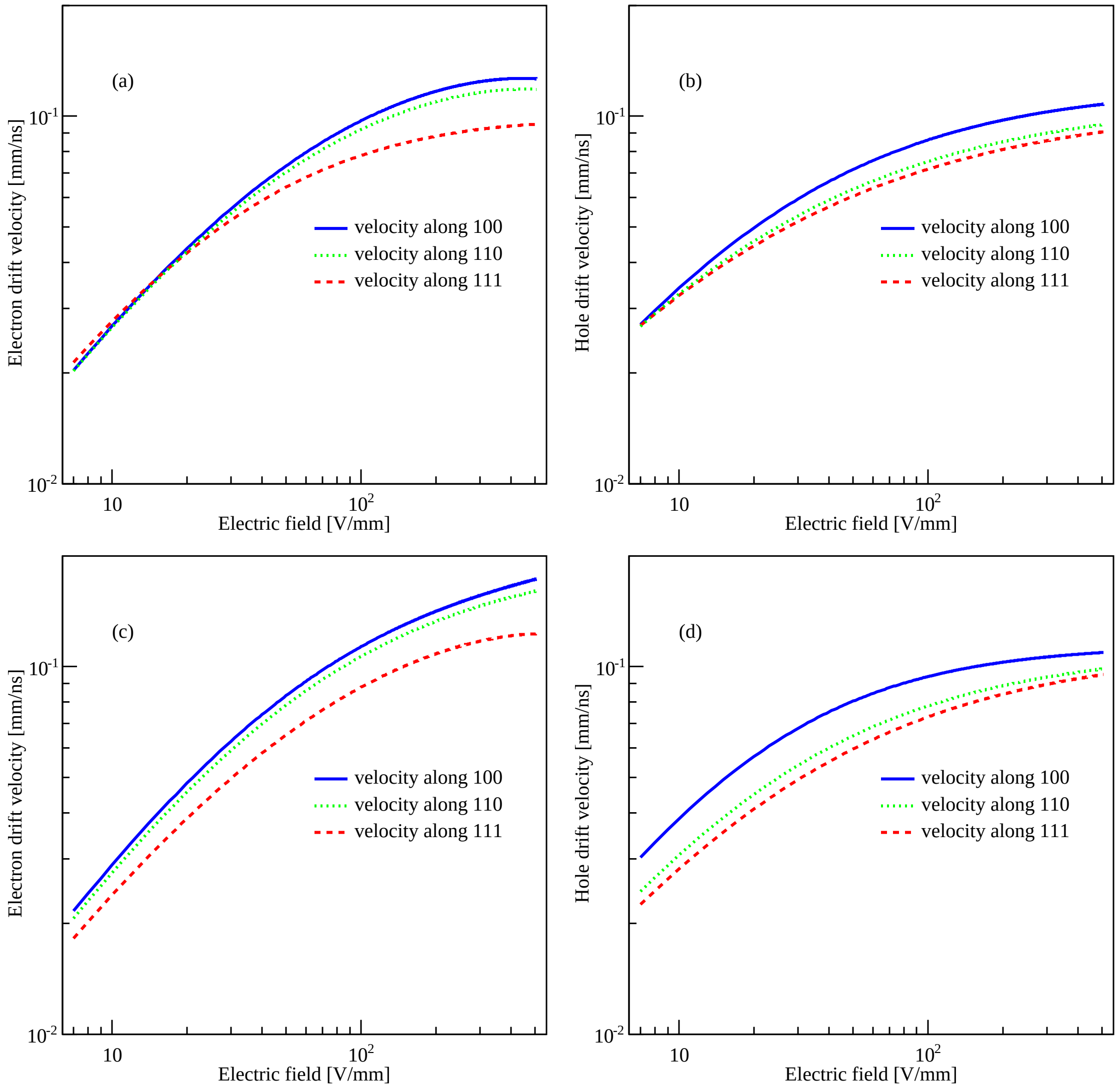

Figure 10.3: Drift velocities of electrons (a, c) and holes (b, d) along the principal crystal axes as functions of electric field in the range of [7,500] V/mm. Velocities along the axes $\langle 100\rangle$ and $\langle 111\rangle$ were calculated according to Eq. 10.2: (a) and (b), the input parameters provided in Ref. [153] and [155] were used; (c) and (d), the input parameters provided in Ref. [156] were used. The velocities along the $\langle 110\rangle$ axis are predicted according sections 10.3.3 and 10.3.4.

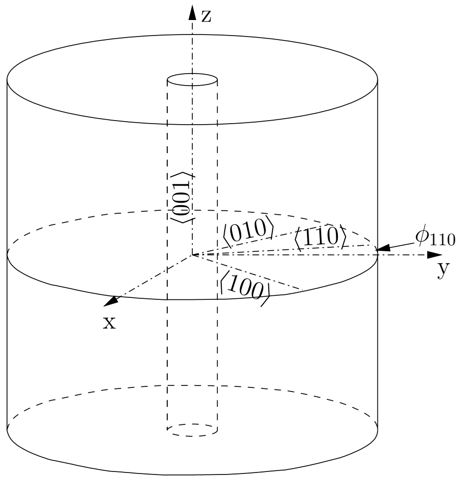

Figure 10.4: The relation between the coordinates xyz used in Geant4 and the crystal axes $\langle 100\rangle$, $\langle 010\rangle$ and $\langle 001\rangle$.

Local coordinates, $x'y'z'$, are defined as shown in Fig. 10.6. The effective mass tensor, γ_0, in $x'y'z'$ coordinates has a very simple expression:

$$\gamma_0 \equiv \begin{pmatrix} m_t^{-1} & 0 & 0 \\ 0 & m_l^{-1} & 0 \\ 0 & 0 & m_t^{-1} \end{pmatrix}, \tag{10.4}$$

where $m_t = 1.64 m_e$ is the transverse effective electron mass and $m_l = 0.0819 m_e$ is the longitudinal effective electron mass, with m_e denoting the free electron mass. Since it is convenient to simulate the interactions and the pulse shape development in the xyz coordinates, the expression of the mass tensor has to be transformed from $x'y'z'$ to xyz coordinates:

$$\gamma_j = R_j^{-1}\gamma_0 R_j = R_j^T \gamma_0 R_j, \tag{10.5}$$

where

$$R_j = R_{x'}(\arccos(\sqrt{2/3}))R_z(\phi_{110} + (j-1)\pi/2) \tag{10.6}$$

is the rotation matrix which aligns one of the four $\langle 111\rangle$ axes to the y-axis. $R_a(\alpha)$ indicates a counter-clockwise rotation around the axis a with rotation angle α.

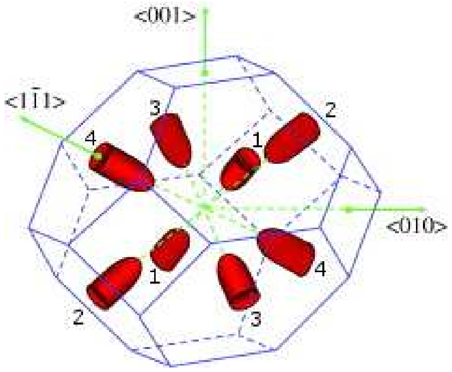

Figure 10.5: Minimal potential regions in the conduction band along four equivalent $\langle 111\rangle$ axes, where the probability density of electrons is dominant (taken from Ref. [156]).

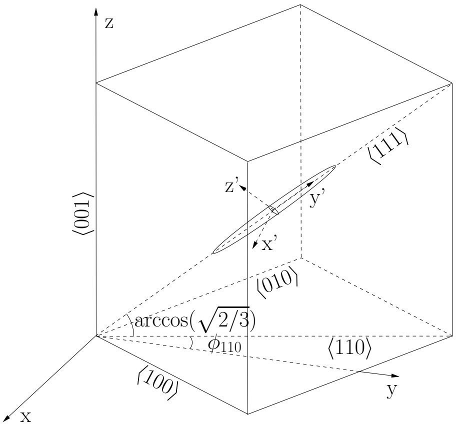

Figure 10.6: Relation between the local coordinates $x'y'z'$ in one of the four ellipsoidal regions with conduction band valleys and the Geant4 coordinates xyz. The x' axis is perpendicular to the plane defined by ⟨111⟩ and ⟨001⟩.

The deviation from an equal population , i.e. n_e/n=1/4, of electrons is assumed to depend on the electric field like:

$$\frac{n_j}{n} = \mathcal{R}(E)\left[\frac{\sqrt{\mathbf{E_0}^T\gamma_j\mathbf{E_0}}}{\sum_i\sqrt{\mathbf{E_0}^T\gamma_i\mathbf{E_0}}} - \frac{n_e}{n}\right] + \frac{n_e}{n}, \tag{10.7}$$

where the coefficient $\mathcal{R}$ is a function of $E = |\mathbf{E}|$ and the temperature.

An electric field applied along the ⟨100⟩ direction, *i.e.* $\mathbf{E_0} = (\sqrt{1/2}, \sqrt{1/2}, 0)^T$ in xyz coordinates with $\phi_{110} = 0$[3] affects the population of the electrons in all ⟨111⟩ valleys equally, hence $n_j/n = 1/4$. Using the drift velocity $v_e^{100}(E)$ according to Eq. 10.2, the absolute value of $\mathcal{A}(E)$ can be expressed as

$$|\mathcal{A}(E)| = \frac{v_e^{100}(E)}{\sum_j \frac{1}{4}\frac{\gamma_j\mathbf{E_0}}{\sqrt{\mathbf{E_0}^T\gamma_j\mathbf{E_0}}}}, \text{ with } \mathbf{E_0} = \begin{pmatrix}\sqrt{1/2}\\ \sqrt{1/2}\\ 0\end{pmatrix}. \tag{10.8}$$

If the electric field vector is oriented along one of the four ⟨111⟩ axes, *i.e.* $\mathbf{E_0} = (0, \sqrt{2/3}, \sqrt{1/3})^T$ in xyz coordinates with $\phi_{110} = 0$, there is an uniform population of the electrons among the other three ⟨111⟩ axes, *i.e.*

$$\frac{n_2}{n} = \frac{n_3}{n} = \frac{n_4}{n}. \tag{10.9}$$

Since

$$\sum_j \frac{n_j}{n} = 1, \tag{10.10}$$

we have

$$\frac{n_1}{n} + 3\frac{n_2}{n} = 1. \tag{10.11}$$

---

[3] Since the values of $\mathcal{A}$ and $\mathcal{R}$ are independent of ϕ_{110}, ϕ_{110} can be set to zero during the determination of $\mathcal{A}$ and $\mathcal{R}$ so that the calculation can be simplified.

Using the drift velocity $v_e^{111}(E)$ for an applied electric field E in the $\langle 111 \rangle$ direction at a specific temperature according to Eq. 10.2, another relation between n_1/n and n_2/n is obtained:

$$v_e^{111}(E) = \mathcal{A}(E)\left(\frac{n_1}{n}\frac{\gamma_1 \mathbf{E_0}}{\sqrt{\mathbf{E_0}^T \gamma_1 \mathbf{E_0}}} + 3\frac{n_2}{n}\frac{\gamma_2 \mathbf{E_0}}{\sqrt{\mathbf{E_0}^T \gamma_2 \mathbf{E_0}}}\right). \tag{10.12}$$

The values of n_1/n and n_2/n can be obtained by solving the equations 10.11 and 10.12. Then $\mathcal{R}(E)$ can be calculated as

$$\mathcal{R}(E) = \left(\frac{n_1}{n} - \frac{n_e}{n}\right) / \left(\frac{\sqrt{\mathbf{E_0}^T \gamma_1 \mathbf{E_0}}}{\sum_j \sqrt{\mathbf{E_0}^T \gamma_j \mathbf{E_0}}} - \frac{n_e}{n}\right), \text{ with } \mathbf{E_0} = \begin{pmatrix} 0 \\ \sqrt{2/3} \\ \sqrt{1/3} \end{pmatrix}. \tag{10.13}$$

After the determination of the coefficients $\mathcal{A}$ and $\mathcal{R}$ the drift velocity can be calculated for any direction and any strength of the electric field. Figures 10.3a and c present the calculated electron drift velocities along the $\langle 110 \rangle$ axis. The velocities are between the ones for the other axes.

10.3.4 Hole drift velocity

The model used to calculate the hole drift velocity is taken from Ref. [156]. In this model only the *heavy hole valence band* is responsible for the anisotropy of the mobility. All other effects are neglected. A hole is accelerated by the electric field until its energy becomes 0.037 eV. At this point it is very likely to emit an optical phonon and lose most of its energy, after which acceleration in the field direction resumes and a new cycle starts.

The probability of finding a heavy hole in a specific momentum state $\mathbf{k}$ is maximal in the direction parallel to the electric field. The mean wave vector $\mathbf{k}_0(k_0, \theta_0, \phi_0)$ is then assumed to be aligned with the electric field $\mathbf{E}(E, \theta, \phi)$, namely, $\theta_0 = \theta, \phi_0 = \phi$, where θ, ϕ are the polar and azimuthal angles with respect to the coordinate system defined by the $\langle 100 \rangle$, $\langle 010 \rangle$ and $\langle 001 \rangle$ axes as shown in Fig. 10.7.

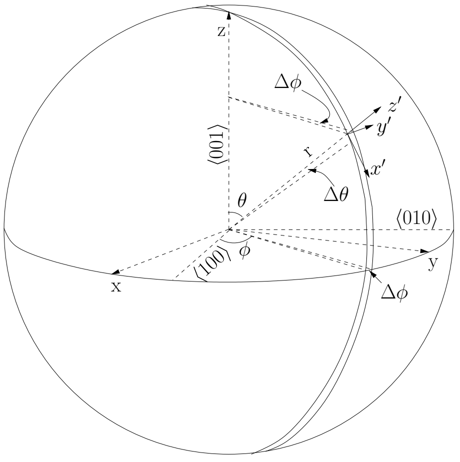

Figure 10.7: Relation between the crystal axes $\langle 100 \rangle$, $\langle 010 \rangle$ and $\langle 001 \rangle$, and the coordinates xyz used in Geant4, and the local coordinates $x'y'z'$.

The three components $(v_{x'}, v_{y'}, v_{z'})^T$ of the hole drift velocity $\mathbf{v}$ in the local coordinates, $x'y'z'$, at any position (r, θ, ϕ) (as shown in Fig. 10.7) can be expressed as:

$$\begin{array}{rcl} v_{x'} = v_r & = & v_h^{100}(E)[1 - \Lambda(k_0)(\sin(\theta)^4 \sin(2\phi)^2 + \sin(2\theta)^2)], \\ v_{y'} = v_\theta & = & v_h^{100}(E)\Omega(k_0)[2\sin(\theta)^3 \cos(\theta)\sin(2\phi)^2 + \sin(4\theta)], \\ v_{z'} = v_\phi & = & v_h^{100}(E)\Omega(k_0)\sin(\theta)^3 \sin(4\phi), \end{array} \tag{10.14}$$

The mean wave number k_0 can be expressed as a function of $v_{rel} = v_h^{111}(E)/v_h^{100}(E)$:

$$k_0(v_{rel}) = 9.2652 - 26.3467v_{rel} + 29.6137v_{rel}^2 - 12.3689v_{rel}^3, \tag{10.15}$$

where $v_h^{111}(E)$ and $v_h^{100}(E)$ are the drift velocities along the $\langle 111\rangle$ and $\langle 100\rangle$ axes. They can be calculated using Eq. 10.2. The magnitude of the anisotropies, Λ and Ω, can be expressed as

$$\Lambda(k_0) = -0.01322k_0 + 0.41145k_0^2 - 0.23657k_0^3 + 0.04077k_0^4, \tag{10.16}$$

$$\Omega(k_0) = 0.006550k_0 - 0.19946k_0^2 + 0.09859k_0^3 - 0.01559k_0^4. \tag{10.17}$$

The three components $(v_x, v_y, v_z)^T$ of the hole drift velocity $\mathbf{v}$ in xyz coordinate (as shown in Fig. 10.7) become:

$$\begin{pmatrix} v_x \\ v_y \\ v_z \end{pmatrix} = R_z(\phi + \frac{\pi}{4} + \phi_{110})R_{y'}(\theta) \begin{pmatrix} v_{x'} \\ v_{y'} \\ v_{z'} \end{pmatrix}, \tag{10.18}$$

where $R_a(\alpha)$ indicates the counter-clockwise rotation around the axes a by the angle α. Figures 10.3b and d present the calculated hole drift velocities along the $\langle 110\rangle$ axis. The velocities are between the ones along the other axes.

10.4 Drift trajectories

The trajectories are calculated iteratively. The displacement vector $\Delta\mathbf{r}$ by which a charge carrier drifts within a short time interval Δt can be calculated once the drift velocity vector $\mathbf{v}_i$ in the original position $\mathbf{r}_i$ is calculated using the method described in the previous two sections. The new position $\mathbf{r}_{i+1}$ is then

$$\mathbf{r}_{i+1} = \mathbf{r}_i + \Delta\mathbf{r} \quad (i = 0, 1, ...), \text{ with } \Delta\mathbf{r} = \mathbf{v}_i\Delta t. \tag{10.19}$$

The iteration continues until the charge carriers reach the boundary of the crystal. The series of position vectors $\mathbf{r}_i$ from $\mathbf{r}_0$ to $\mathbf{r}_{\text{boundary}}$, $(\mathbf{r}_0, \mathbf{r}_1, ..., \mathbf{r}_i, ..., \mathbf{r}_{\text{boundary}})$, represents the trajectory.

Two different numerical methods were used to calculate the trajectory, the Euler method and the 4^{th} Runge-Kutta method. The Euler method is less computer time intensive, but is also less precise. However, for time intervals $\Delta t < 1$ ns, the output of the two methods does not differ significantly. The results presented here were obtained with the Runge-Kutta method.

Figure 10.8 shows the drift trajectories projected on an x-y cross sections of a Siegfried-like detector. The crystal axis $\langle 110 \rangle$ is assumed to be parallel to the x-axis (i.e., ϕ_{110} as shown in Fig. 10.4 is set to zero). The left plot shows the inward drift of electrons starting at the outer surface of the detector. The starting points are distributed equidistantly on the outer circle. The right plot shows the outward drift of holes starting at the inner surface. The starting points are distributed equidistantly on the inner circle. The bias voltage was set to 3000 V. The time interval was 1 ns. The time window for the calculation was 400 ns. All electrons reach the inner surface within this time window, but not all holes reach the outer surface. This is because electrons drift faster than holes. Holes drift slowest along the $\langle 110 \rangle$ direction, as also shown in Fig. 10.3.

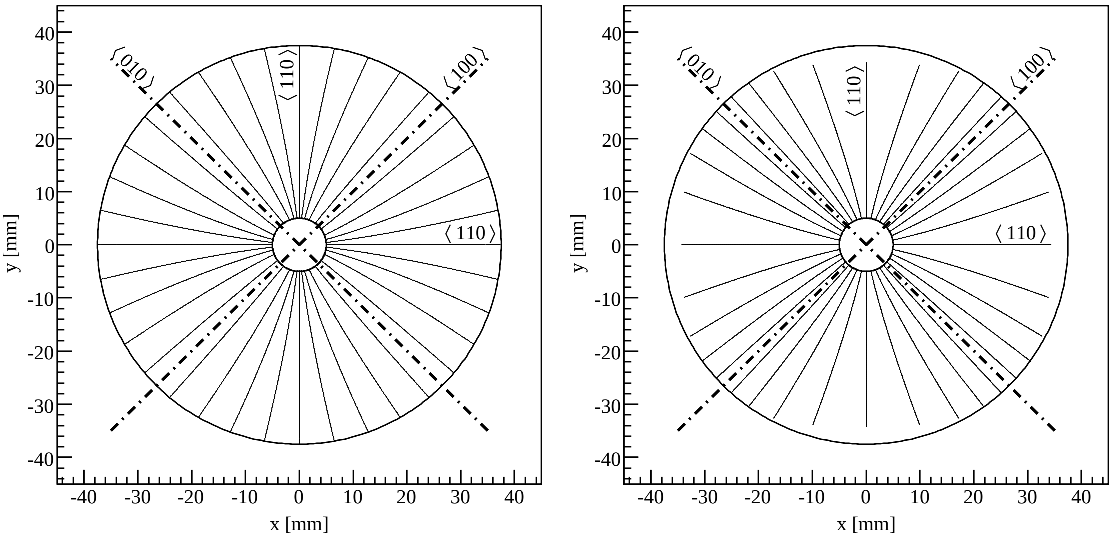

Figure 10.8: Drift trajectories projected on the x-y cross sections of Siegfried-like detectors: Left, electrons drift inward; Right, holes drift outward.

The trajectories along the crystal axes are straight as explained in Sec. 10.3.1. However, they are clearly bent along other directions. This causes the different occupancies in different segments that was shown in Fig. 8.5b. The crystal axis orientation can be deduced by comparing the occupancy distributions of data and MC. This will be described in detail in Chapter 11.

10.5 Raw pulse shapes

Once the weighting fields and potentials as well as the drift velocities and trajectories of the charge carriers are known, Eq. 4.4 and 4.5 introduced in Sec. 4.4 can be used to calculate the time development of the induced charge $Q(t)$ and current $I(t)$ in each electrode (raw pulses in short), which are shown in Figure 4.1b.

10.6 Effects of electronics

The pulses recorded by the DAQ system are quite different from the raw pulses. Not only their amplitudes but also their shapes are changed by the electronics. The baseline after a pulse exponentially decreases to its original level with a time constant τ. The limit on the bandwidth of the signal transmission through the electronics cuts off the signal components with frequencies higher than the limit. Sharp edges in a pulse are hence smeared. Electronic noise may destroy any detailed structure of a pulse. All these effects need to be simulated.

Figure 10.9 shows a modified pulse after folding in the decay of the baseline after the pulse, the limited bandwidth and the noise. The decay time was 5μs, the cut-off in bandwidth was 10 MHz and the noise level was 5% of the pulse amplitude. These values are worse than observed in the tests stands. They were chosen to clearly demonstrate influence of the effects.

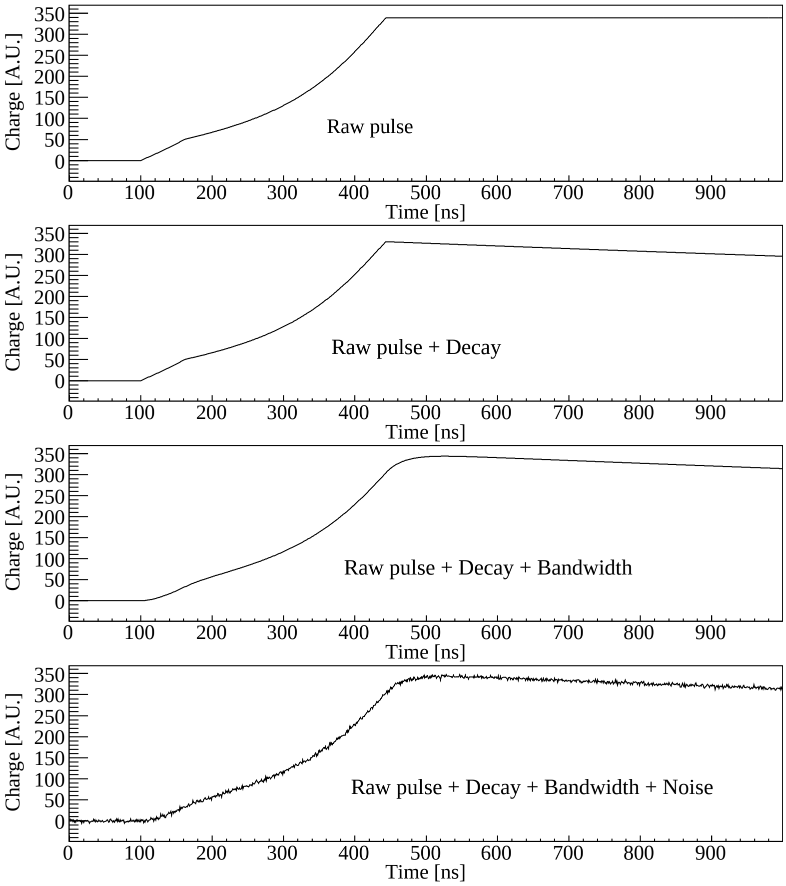

Figure 10.9: Modified pulses after folding in the decay of the baseline after the pulse, the limited bandwidth and the noise.

Chapter 11

Validation of pulse shape simulation

The physics models [153, 156] for the drift of charge carriers and their measured input parameters [153, 156] alone are not enough to provide a realistic pulse shape simulation. While some input parameters are generic to germanium, others, like the impurity density and the detailed properties of the surface layers, are different for each detector. Thus the simulation has to be tuned for each individual detector or at least for a series of similar detectors.

Several data samples were taken with the first GERDA Phase II prototype detector Siegfried I (see Sec. 3.3.3) operated in its test stand (see Sec. 5.1.1) to characterize the detector. The pulse shape simulation was verified using these data. The results are presented in this chapter.

11.1 Detector characterization measurements

A detailed description of the characterization of Siegfried I is available in Ref. [123]. Two data samples were used to verify the simulation:

Surface scanning: The surfaces of segments 13, 14 and 15 (see Fig. 3.7) were scanned in ϕ (azimuth angle) using a 75 kBq ^{152}Eu source inside a copper collimator with a length of 52 mm and a pin-hole diameter of 11 mm. The spot size on the detector surface was estimated to be ≈ 150 mm^2. The distance between the collimator and the center of the detector was ≈ 85 mm. The center of the collimator was pointed at $z = 0$ (see Fig. 10.4). The step size of the scan was 5° in segment 14 and 10° in segment 13 and 15. The uncertainty in ϕ is $\approx \Delta\phi = 2.5°$. In total 25 measurements were performed to cover 180° in azimuth. The pulses of the core and all segments were recorded. There were about 50 000 events per measurement.

Occupancy measurement: A 60 kBq ^{60}Co source was positioned about 15 cm above the center of Siegfried I (see Fig. 8.4). The energy deposits seen by each segment and the core were recorded.

The 122 keV γ line of the ^{152}Eu source used in the scan provided the events to study the drift of electrons. Because these low energy photons in average do not penetrate deeply into germanium and most likely deposit energy locally through the photoelectric effect (see Sec. 4.1.2), they create electron-hole pairs predominantly near the outer surface of the detector. The holes reach the outer surface almost immediately while the electrons have to drift through nearly the whole bulk of the detector until they reach the inner surface. Therefore, the pulse shapes are mainly determined by the drift of the electrons.

To analyze the pulse shapes quantitatively the 10%-30% and 10%-90% risetimes of the core pulses were calculated. Figure 11.1 shows the average risetimes as a function of the azimuth angle ϕ. The segment boundaries are also indicated. Clear oscillation patterns can be seen in both cases. This confirms the longitudinal anisotropy of the drift velocity of electrons depending on the angle ϕ. The electrons need different times to drift nearly the same distance.[1]

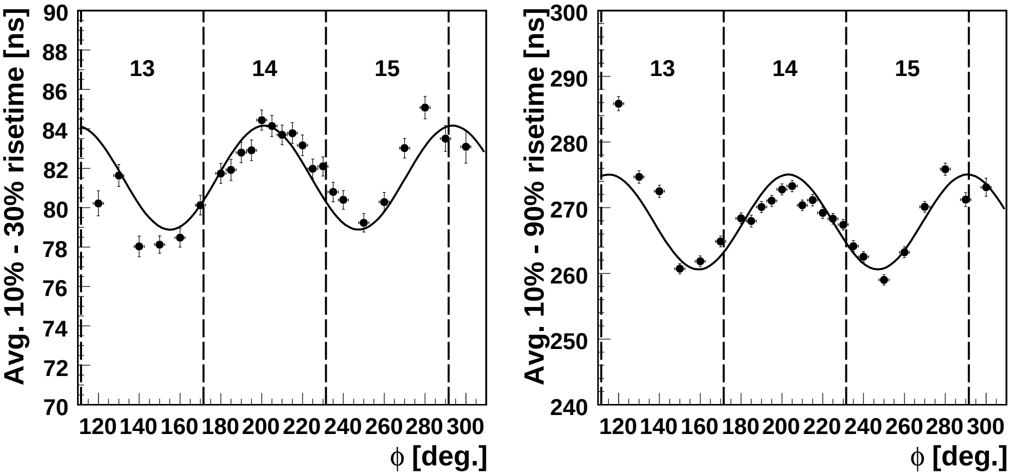

Figure 11.1: Average 10%-30% (left) and 10%-90% (right) risetimes of the core pulses as a function of the azimuth angle ϕ (taken from Ref. [123]). The dashed lines indicate the segment boundaries.

Fits with a sine function (Fig. 11.1) give periods of about 90° for the longitudinal anisotropy. This supports the model introduced in the previous chapter. The effect is illustrated in Fig. 10.8. A direct comparison of the pulse shapes in data and simulation will follow in the next section.

---

[1] Strictly speaking, because of the bend of the drift trajectories the distances covered by electrons in different ϕ angles are sightly different from each other. However, this is a second-order effect. The difference of the risetimes is mainly caused by the different drift velocity along r at different angles ϕ.

11.2 Longitudinal anisotropy

Pulses induced in the core electrode by the drift of electrons starting at the outer surface of Siegfried I were simulated. The geometry, the operational voltage and the impurity density were implemented in the simulation according to the values listed in Table 3.1.

According to the model, electrons drift slowest along the $\langle 110 \rangle$ axes and risetimes reach their maxima. Thus, Figure 11.1 indicates that one of the $\langle 110 \rangle$ axes is nearly aligned with the right boundary of segment 15 at $\approx 290°$. This was implemented in the simulation. A decay time of 50 μs and a cut-off bandwidth of 37.5 MHz were implemented according to the specification of the electronics system. Electronic noise was not added to the pulse simulation to simplify direct comparisons with individual pulses. Several parameters, *i.e.* the *Amplitude*, the *Time offset* and the *Time scaling factor* of the pulse, were introduced to fit the shape of a simulated to a measured pulse. The time offset shifts the pulse while the time scaling factor stretches or squeezes the pulse in time.

Figure 11.2 shows a randomly selected core pulse and the result of a fit with the simulated pulse along the $\langle 110 \rangle$ axis. The fit yields a time scaling factor of 0.81, indicating that the simulated pulse underestimates the pulse-length by $\approx$ 20%. Nevertheless the χ^2/NDF is excellent. In general a factor between 1 and 1.06 is expected as the simulation reflects the maximal risetime.

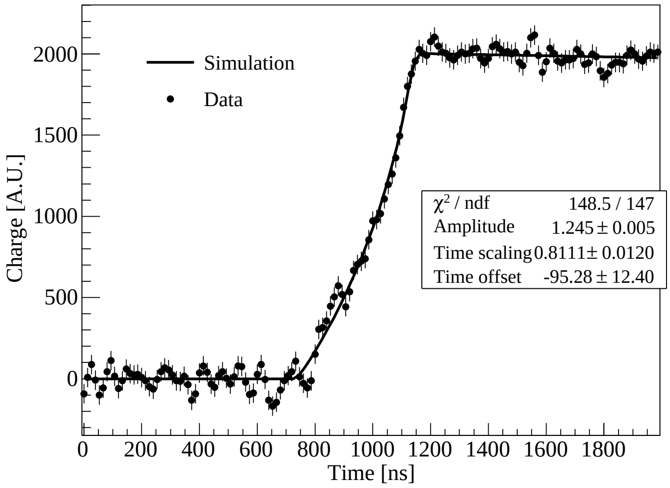

Figure 11.2: Fit of a simulated to a measured pulse. The dots represent the data and their error bars indicate the noise level.

A subset of pulses with fits were selected requiring

- $\chi^2 < 200$ to eliminate background events,
- The pulse amplitude in simulation must be equal to that in data within the resolution to eliminate events mis-recorded by the DAQ,

- Time offset > -300 ns as very early pulses were not treated correctly by the DAQ.

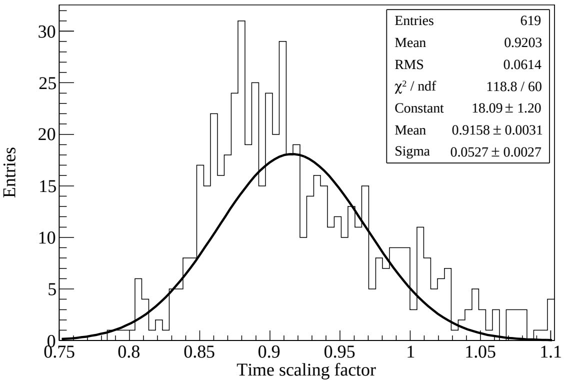

Figure 11.3: Time scaling factors from the fits of the simulated to measured pulses taken at $\phi = 280°$.

The distributions of the time scaling factors for each scan position were fitted with a Gaussian function. Fig. 11.3 shows the distribution for $\phi = 280°$. The scaling factor at 280° should be close to one, if the model would represent the detector perfectly. It is about 7% lower.

The mean scaling factors obtained from the fits versus azimuth are displayed in Fig. 11.4. The points were fitted with a sine wave plus a 1^{st}-order polynomial. The period of the sinusoid was fixed to 90°. The shifted polynomial is shown as a baseline in Fig. 11.4. The data is reasonably well described by the fit. However, the different values obtained for different instances of the $\langle 110 \rangle$ configuration indicate that the actual detector is more complex than assumed. One possible interpretation is that the impurity density given in Table 3.1 is an average density and in reality varies with the azimuthal angle ϕ.

The oscillation pattern expected and seen in Fig. 11.4 should disappear when the pulses are simulated for the individual angular configuration of the the scan points. This was done and the result is depicted in Fig. 11.5. Also given is the shifted polynomial from the fit to the data in Fig. 11.4 and a straight line fit to the points in Fig. 11.5. The two lines are very close confirming the predictions of the model for the angular dependence of the rise-time. The deviations from the fitted straight line are below 3% and indicate that the real crystal is not as perfect as the simulated one. The overall shift relative to one is in average about 10% and can easily be corrected for.

11.3 Transverse anisotropy

The transverse anisotropy of the drift leads to the bent drift trajectories shown in Fig. 10.8. Consequently, the charge carriers created in one segment may drift into a neighboring segment. As a result, some segments always show a higher occupancy, because the trajectories

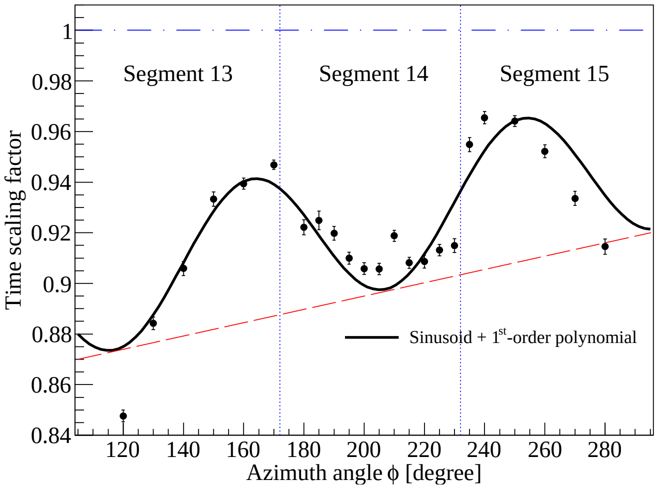

Figure 11.4: Mean time scaling factor (black dots) of a simulated ⟨110⟩ pulse versus azimuth. The solid line represents a fit with a sine wave plus a 1^{st}-order polynomial. The dashed line shows the shifted polynomial as a baseline.

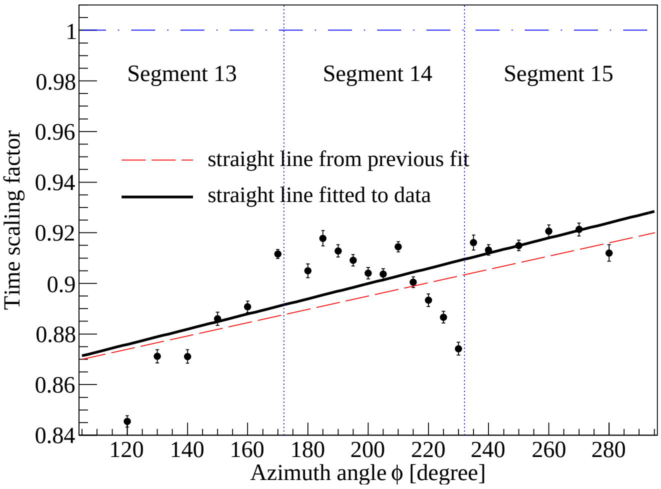

Figure 11.5: Mean time scaling factor (black dots) for pulses simulated for each angle individually against ϕ. The result of a straight line fit is given as a solid line. The shifted polynomial from Fig. 11.4 is overlaid for comparison.

are more likely to bend towards them. This effect was already shown in Fig. 8.5b. It is independent of the amount of energy deposited.

To verify quantitatively how well the effect can be described, 100 000 hits with the same energy were homogeneously distributed in the middle layer of Siegfried I. The drift of holes was simulated for each location. If a trajectory ended on the outer surface of a given segment, its occupancy increased by one.

The predicted occupancies depend on the orientation of the crystal axes where the $\langle 110\rangle$ axis is again used as a reference. The resulting ϕ-dependence of the occupancies was fitted to data with the orientation of the $\langle 110\rangle$ axis as a free parameter. The occupancies from the best fit are given in Fig. 11.6a. The direction of the $\langle 110\rangle$ axis from the fit is only 4° different from one of the segment boundaries. This is in good agreement with the result from the scan.

Figure 11.6b shows the χ^2/NDF versusϕ_{110}, the azimuthal difference between the orientation of the $\langle 110\rangle$ axis and the segment boundary. Due to the crystal structure there is a 90° degeneracy in the χ^2 distribution. As also reflected in Fig. 11.6a the χ^2/NDF is not good. However, the minima in the χ^2 distribution are very distinct, allowing nevertheless a precise determination of the orientation of the crystal axes.

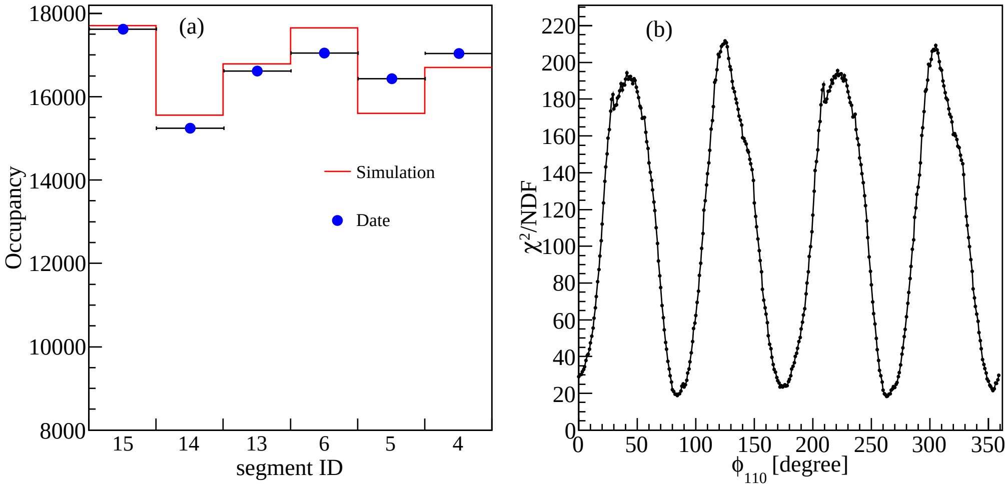

Figure 11.6: (a) Occupancies of each segment (see Fig. 3.7 for the segmentation scheme) for data (dots) and best fit simulation(histogram). (b) χ^2/NDF of the fit described in the text versus ϕ_{110}, the angle between the $\langle 110\rangle$ axis and the segment boundary.

While the overall behavior of the data is well described, the precise differences in occupancy cannot be perfectly reproduced. The segmentation and crystal axes orientations together have a 180° degeneracy: if the segment boundaries or the crystal axes are rotated around the z-axis by 180°, the whole configuration does not change. This is reflected in the simulation which predicts the same pattern for segments 15, 14, and 13 and segments 6,5, and 4. The data, however, do not provide identical differences in occupancy. The first three segments show larger differences than the last three. One possible explanations is that the impurity density varies around ϕ.

11.4 Summary

The data confirm the longitudinal and transverse anisotropies inherent to the model of the drift of charges carriers used to simulate pulses in germanium detectors. The longitudinal anisotropy connected to the drift of electrons was seen in the dependence of the risetime on the azimuthal angle, ϕ, of the energy deposition. After adjusting the simulation reproduces the risetimes within $\pm 3\%$.

The transverse anisotropy connected to the drift of holes was observed as variations of the occupancy of segments located at different ϕ. It was established that these variations can be used to determine the crystal orientation without a time consuming scan of the crystal.

Summary and outlook

The results presented in this thesis can be summarized as follows:

1. Segmented n-type germanium detectors can be operated stably over long periods submerged in a cryogenic liquid;
2. They can facilitate the discrimination of both photon- and neutron-induced background from beta decay signals.
3. The pulse shapes of segmented detectors can be simulated reliably using basic information about semiconductor-detectors;
4. A novel way to determine the crystal orientation and impurity distribution of a segmented detector was developed.

The work was performed in the context of detector development for Phase II of the GERDA neutrinoless double beta decay experiment. The results are highly relevant for the realization of this experiment.

1. Segmented n-type germanium detectors are considered to be used in GERDA Phase II which is based on the idea to submerge detectors in liquid argon to achieve extremely low background levels using the liquid as a shield against external radiation.
2. The background level due to the predicted radioactivity within GERDA can only reach the extremely low level targeted, if both photon- and neutron-induced backgorund can be rejected with good efficiency.
3. Even though background events are identified very well using segment information, an additional suppression factor of ≈ 1.3 for photon-induced events is expected from pulse shape analysis. However, the verification of this expectation is important and impossible without excellent pulse shape simulation.
4. As handling has to be minimized during the production of the GERDA detectors in order to minimize possible contamination, the control measurements should be kept to a minimum. This novel way to determine the crystal orientation needed for pulse shape analysis allows an in-situ measurement of crystal properties during a normal energy calibration inside the GERDA cryostat.

As part of the work presented in this thesis, many tests were made to study segmented germanium detectors and the complete read-out and support system. The understanding of these novel kinds of detectors was enhanced considerably. The operation of the detectors and the tuning of the electronics provides guidelines for the operation of GERDA. This includes monitoring and control software.

The Monte Carlo package, MaGe, used to simulate all aspects of the GERDA experiment, was verified using photon-induced and neutron-induced events. Several problems, especially in the simulation of neutron interactions, were identified and solved. The overall agreement of the Monte Carlo predictions with data taken in the test facilities was very satisfactory.

The detector system including read-out and signal transmission and processing is still being optimized:

- the signal transmission inside the cryogenic liquid needs to be further improved to minimize cross-talks and micro-phonic effects;
- the high voltage distribution into the cryogenic volume has to be improved to allow stable running not only with liquid nitrogen, but also with liquid argon;

It is planned to operate three segmented germanium detectors together in liquid argon, providing a test environment as close as possible to the GERDA environment and allowing a large variety of detector studies.

- Data will be collected with a low energy gamma source placed inside the core of a segmented n-type detector. Holes created close to the inner surface of the detector will drift outwards while electrons reach the inner surface almost immediately. Thus, the drift of the holes can be studied separately.
- Various surface scans will be performed on at least three different segmented detectors of the same type. This will allow the verification of the pulse shape simulation package with a large variety of data.
- Several pulse shape analyses will be performed and evaluated using data and Monte Carlo including pulse shape simulation. The potential for background discrimination will be studied in detail.

All these studies will rely on the work presented in this thesis and will further the understanding of segmented germanium detectors. The results will provide information for the operation of GERDA and the planning of future germanium based experiments.

Bibliography

[1] I. Abt *et al.*, arXiv:hep-ex/0404039v1.

[2] S. Schönert *et al.*, [GERDA Collab.], Nucl. Phys. Proc. Suppl. **145** (2005) 242.

[3] W. Pauli, *Vorträge und Aufsätze über Physik und Erkenntnistheorie*, 2. Auflage, Friedr, Vieweg & Sohn, Braunschweig/Wiesbaden, (1984) 156.

[4] E. Fermi, Ricercha Scient. **2** (1933) 12.

[5] E. Fermi, Z. Phys. **88** (1934) 161.

[6] L. M. Langer and R. J. D. Moffat, Phys. Rev. **88** (1952) 689.

[7] I. Curie and J. F. Joliot, Comptes Rendus **198** (1934) 254.

[8] L. W. Alvarez, Phys. Rev. **53** (1938) 606.

[9] C. L. Cowan, *et al.*, Science **124** (1956) 103.

[10] F. Reines and C. L. Cowan, Jr., Nature **178** (1956) 446.

[11] R. Davis Jr., Phys. Rev. **97** (1955) 766.

[12] R. Davis Jr., Bull. American Phys. Soc., Washington Meeting (1956) 219.

[13] T. D. Lee and C. N. Yang, Phys. Rev. **104** (1956) 254.

[14] C. S. Wu *et al.*, Phys. Rev. **105** (1957) 1413.

[15] R. L. Garwin *et al.*, Phys. Rev. **105** (1957) 1415.

[16] J. L. Friedman and V. L. Telegdi, Phys. Rev. **105** (1957) 1681.

[17] T. D. Lee and C. N. Yang, Phys. Rev. **105** (1957) 1671.

[18] A. Salam, Nuovo Cimento **5** (1957) 229.

[19] L. Landau, Nucl. Phys. **3** (1957) 127.

[20] H. Weyl, Z. Phys. **56** (1929) 330.

[21] M. Goldhaber *et al.*, Phys. Rev. **109** (1958) 1015.

[22] V. Gribov, B. Pontecorvo, Phys. lett. B **28** (1969) 493.

[23] R. Davis Jr., Phys. Rev. lett. **12** (1964) 303.

[24] R. Davis Jr. *et al.*, Phys. Rev. lett. **20** (1968) 1205.

[25] J. N. Bahcall, S. Basu and M. H. Pinsonneault, Phys. Lett. B **433** (1998) 1.

[26] L. Wolfenstein, Phys. Rev. D **17** (1978) 2369.

[27] S. P. Mikheyev, A. Yu. Smirnov, Yad. Fiz. **42** (1985) 1441; Nuovo Cimento C **9** (1986) 17.

[28] K. S. hirata *et al.*, [Kamiokande Collab.], Phys. Rev. Lett. **63** (1989) 16.

[29] A. I. Abazov *et al.*, [SAGE Collab.], Phys. Rev. Lett. **67** (1991) 3332.

[30] P. Anselmann *et al.*, [Gallex Collab.], Phys. Lett. B **285** (1992) 376.

[31] Q. R. Ahmad *et al.*, [SNO Collab.], Phys. Rev. Lett. **87** (2001) 071301.

[32] S. Fukuda *et al.*, [Kamiokande Collab.], Phys. Rev. Lett. **86** (2001) 5651.

[33] T. J. Haines *et al.*, [IMB Collab.], Phys. Rev. Lett. **57** (1986) 1986.

[34] K. S. Hirata *et al.*, [Kamiokande Collab.], Phys. lett. B **205** (1988) 416.

[35] Y. Fukuda *et al.*, [Kamiokande Collab.], Phys. Lett. B **335** (1994) 237.

[36] Y. Fukuda *et al.*, [Kamiokande Collab.], Phys. Rev. Lett. **81** (1998) 1562; Phys. Lett. B, **436** (1998) 33.

[37] T. Araki *et al.*, [KamLAND Collab.], Phys. Rev. Let. **90** (2003) 021802.

[38] S. Abe *et al.*, [KamLAND Collab.], arXiv:0801.4589v3 [hep-ex].

[39] M. Apollonio *et al.*, [Chooz Collab.], Eur. Phys. J. C **27** (2003) 331.

[40] Yu. Kozlov, L. Mikaelyan, V. Sinev, Phys. Atom. Nucl. **66** (2003) 1934; Yad. Fiz. **66** (2003) 1986.

[41] F. Ardellier *et al.*, arXiv:hep-ex/0606025v4.

[42] Daya Bay Collab. arXiv:hep-ex/0701029v1.

[43] S. Kim, NuFact 07. AIP Conf. Proc. **981** (2008) 205.

[44] M. H. Ahn *et al.*, [K2K Collab.], Phys. Rev. D **74** (2006) 072003.

[45] D. G. Michael *et al.*, [MINOS Collab.], Phys.Rev.Lett. **97** (2006) 191801.

[46] R Acquafredda *et al.*, [OPERA Collab.], New J. Phys. **8**, (2006) 303.

[47] B. Armbruster *et al.*, [KARMEN Collab.], Phys. Rev. Lett. **90** (2003) 181804.

[48] S. Dodelson, A. Melchiorri, A. Slosar, Phys. Rev. Lett. **97** (2006) 04301.

[49] A. A. Aguilar-Arevalo *et al.*, [MiniBooNE Collab.], Phys. Rev. Lett. **98** (2007) 231801.

[50] Y. Oyama, arXiv:hep-ex/0512041v2.

[51] D. S. Ayres *et al.*, [NOvA Collab.], arXiv:hep-ex/0503053.

[52] C. Amsler *et al.*, [Particle Data Group], Phys. Lett. B **667** (2008) 1.

[53] K. A. Olive arXiv:astro-ph/0202486.

[54] A. Strumia and F. Vissani, arXiv:hep-ph/0503246v1.

[55] G.L. Fogli *et al.*, arXiv:0805.2517v2 [hep-ph].

[56] Planck Collab., ESA-SCI(2005)-1. Version 2.

[57] C. Weinheimer *et al.*, Phys. Lett. B **460** (1999) 219.

[58] V. M. Lobashev *et al.*, Phys. Lett. B **460** (1999) 227.

[59] A. Osipowicz *et al.*, arXiv:hep-ex/0109033.

[60] A. Monfardini *et al.*, arXiv:hep-ex/0509038.

[61] C. Arnaboldi *et al.*, [CUORICINO Collab.], arXiv:0802.3439v1 [hep-ex].

[62] H. V. Klapdor-Kleingrothaus *et al.*, Phys. Lett. B **586** (2004) 198.

[63] G. L. Fogli *et al.*, Phys. Rev. D **75** (2007) 053001.

[64] K. Assamagan *et al.*, Phys. Rev. D **53** (1996) 6065.

[65] NuMass Collab. `http://www.hep.umn.de/numass`.

[66] M. Yoshimura, arXiv:hep-ph/0611362v4.

[67] K. Fujikawa and R. Shrock, Phys. Rev. Lett. **45** (1980) 963.

[68] C. S. Lim and W. J. Marciano, Phys. Rev. D **37** (1988) 1368.

[69] E. Kh. Akhmedov, preprint IAE-4568/1 (1988).

[70] W. Grimus *et al.*, Nucl. Phys. B **648** (2002) 376.

[71] A. Caldwell, K. Kröninger, Phys. Rev. D **74** (2006) 092003; arXiv:physics/0608249 [physics.data-an].

[72] K. Muto *et al.*, Z. Phys. A **334** (1989) 187; Z. Phys. A **339** (1991) 435.

[73] V. Rodin *et al.*, Nucl. Phys. A **766** (2006) 107. [Erratum A **793** (2007) 213].

[74] F. Simkovic *et al.*, arXiv:0710.2055v3 [nucl-th].

[75] E. Caurier *et al.*, Eur. Phys. J. A **36** (2008) 195; arXiv:0709.0277v2 [nucl-th].

[76] I. Ogawa *et al.*, Nucl. Phys. A **730** (2004) 215.

[77] Y. Hirano *et al.*, J. Phys. Conf. Series **120** (2008) 052053.

[78] Yu. G. Zdesenko *et al.*, Astropar. Phys. **23** (2005) 249.

[79] C. E. Aalseth *et al.*, [IGEX Collab.] Phys. Rev. D **65** (2002) 092007; arXiv:hep-ex/0202026.

[80] R. Gaitskell *et al.*, [Majorana Collab.] arXiv:nucl-ex/0311013.

[81] C. E. Aalseth *et al.*, [Majorana Collab.] Phys. Atom. Nucl. **67** (2004) 2002; Yad. Fiz. **67** (2004) 2025; arXiv:hep-ex/0405008.

[82] K. Zuber, Phys. Lett. B **519** (2001) 1.

[83] S. Elliot, P. Vogel, Ann. Rev. Nucl. Part. Sci. (2002).

[84] H. Kiel *et al.*, Nucl. Phys. A **723** (2003) 499.

[85] F T Avignone III, G S King III and Yu G Zdesenko, New J. Phys. **7** (2005) 6.

[86] F. A. Danevich *et al.*, Phys. Rev. C **62** (2000) 045501.

[87] F. A. Danevich *et al.*, Phys. Rev. C **68** (2003) 035501.

[88] G. Bellini *et al.*, Phys. Lett. B **493** (2000) 216.

[89] G. Bellini *et al.*, Eur. Phys. J. C **19** (2001) 43.

[90] C. Arpesella *et al.*, [Borexino Collab.], Phys. Lett. B **658**, (2008) 101.

[91] E. Previtali *et al.*, Nucl. Instr. Meth. A **518** (2004) 256258.

[92] C. Arnaboldi *et al.*, Nucl. Instr. Meth. A **518** (2004) 775798.

[93] R. Ardito *et al.*, arXiv:hep-ex/0501010.

[94] C. Arnaboldi *et al.*, arXiv:0802.3439v1 [hep-ex].

[95] L. Gironi *et al.*, arXiv:0809.5126v1 [nucl-ex].

[96] R. Luescher *et al.*, Phys. Lett. B **434** (1998) 407.

[97] M. Danilov *et al.*, Phys. Lett. B 480 (2000), 12.

[98] Y. D. Kim, [XMASS Collab.], Phys. Atomic Nuclei, **69** (2006) 1970.

[99] K. Zuber, [SNO+ Collab.], AIP Conf. Proc. **942** (2007) 101.

[100] I. Štekl *et al.*, Czech. J. Phys. **48** (1998) 249.

[101] I. Štekl *et al.*, Czech. J. Phys. **50** (2000) 553.

[102] I. Štekl *et al.*, Czech. J. Phys. **56** (2006) 505.

[103] D. Dassié *et al.*, Nucl. Instr. Meth. A **309** (1991) 465.

[104] R. Arnold *et al.*, Nucl. Instr. Meth. A **354** (1995) 338.

[105] R. Arnold *et al.*, Nucl. Instr. Meth. A **536** (2005) 79.

[106] R. Arnold *et al.*, Nucl. Phys. A **781** (2007) 209.

[107] SuperNEMO homepage: `http://nemo.in2p3.fr/supernemo/`

[108] H. Nakamura *et al.*, J. Phys. Conf. Ser. **39** (2006) 350.

[109] N. Ishihara *et al.*, Nucl. Phys. B Proc. Suppl. **143** (2005) 549.

[110] M. Nakahata, Talk on IIIrd International Workshop on Low Energy Solar Neutrinos (LowNu 2002), `http://www.mpi-hd.mpg.de/nubis/www_lownu2002/transparency/nakahata_lownu2002.pdf`.

[111] N. Ishihara, Talk on International Workshop on Double Beta Decay and Neutrinos (DBD07), `http://dbd07.phys.sci.osaka-u.ac.jp/presentation/Ishihara.pdf`.

[112] G. Heusser, Annu. Rev. Nucl. Part. Sci. **45** 1995 543.

[113] M. Ambrosio *et al.*, [MACRO Collab.], Phys. Rev. D **52** (1995) 3793.

[114] P. Lipari, T. Stanev, Phys. Rev. D **44** (1991) 3543.

[115] M. Ambrosio *et al.*, [MACRO Collab.], Astropar. Phys. **19** (2003) 313.

[116] D. M. Mei and A. Hime, Phys. Rev. D **73** (2006) 053004.

[117] C. Cattadori *et al.*, Nucl. Instr. Meth. A, **572** (2007) 479.

[118] I. Abt *et al.* Nucl. Instr. Meth. A, **570** (2007) 479.

[119] I. Abt *et al.* Eur. Phys. J. C **52** (2007) 19; arXiv:0704.3016v1 [nucl-ex].

[120] P. Peiffer *et al.*, Nucl. Phys. B Proc. Supp. **143** (2005) 511.

[121] J. L. Orrell, C. E. Aalseth, J. F. Amsbaugh, P. J. Doe and T. W. Hossbach, arXiv:nucl-ex/0610018.

[122] H. V. Klapdor-Kleingrothaus *et al.*, Nucl. Instr. Meth. A **481** (2002) 149; arXiv:hep-ex/0012022.

[123] I. Abt *et al.*, Nucl. Instr. Meth. A **577** (2007) 574; arXiv:nucl-ex/0701004v1.

[124] U. Amaldi, Phys. Scripta **23** (1981) 409.

[125] D. K. Brice, Nucl. Instr. Meth. B **12** (1985) 187.

[126] W. Sasaki and M. Shibuya, J. Phys. Soc. Japan **11** (1956) 1202.

[127] E. Gatti, *et. al.*, Nucl. Instr. Meth. **193** (1982) 651.

[128] V. radeka, Ann. Rev. Nucl. Part. Sci. **38** (1988) 217.

[129] Z. He, Nucl. Instr. Meth. A **463** (2000) 250.

[130] B. Bruyneel, Ph.D. Thesis, `http://kups.ub.uni-koeln.de/volltexte/2006/1858/`, (2006).

[131] *Digital Gamma Finder (DGF) PIXIE-4, User's Manual*, X-Ray Instrumentation Associates, Version 1.20, `http://www.xia.com`.

[132] H. Utsunomiya *et al.*, Nucl. Instr. Meth. A **548** (2005) 455.

[133] J. Eberth and J. Simpson, Prog. Par. Nucl. Phys. **60** (2008) 283.

[134] I. Abt *et al.*, Nucl. Instr. Meth. A **583** (2007) 332.

[135] M. Bauer *et al.*, J. Phys. Conf. Series. **39** (2006) 362.

[136] Y. Chan *et al.*, arXiv:0802.0860v1 [nucl-ex].

[137] S. Agostinelli *et al.*, [Geant4 Collab.], Nucl. Instr. Meth. A **506** (2003) 250.

[138] J. Allison *et al.*, IEEE Trans. Nucl. Sci. **53** (2006) 207.

[139] J. W. Marsh *et al.*, Nucl. Instr. Meth. A **366** (1995) 340.

[140] K. W. Geiger, L. Van Der Zwan, Nucl. Instr. Meth. **131** (1975) 315.

[141] D. Lister, A. B. Smith, Phys. Rev. **183** (1969) 954.

[142] J. J. Kraushaar *et al.*, Phys. Rev. **101** (1956) 139.

[143] Refer to "problem 675" in the Geant4 Problem Tracking System: `http://bugzilla-geant4.kek.jp/`

[144] Refer to "problem 955" in the Geant4 Problem Tracking System: `http://bugzilla-geant4.kek.jp/`

[145] Refer to "problem 956" in the Geant4 Problem Tracking System: `http://bugzilla-geant4.kek.jp/`

[146] Refer to "problem 957" in the Geant4 Problem Tracking System: `http://bugzilla-geant4.kek.jp/`

[147] B. Aspacher, A. C. Rester, Nucl. Instr. Meth. A **338** (1994) 511.

[148] J. Gerl, W. Korten eds., Online AGATA Technical Proposal, `http://agata.pd.infn.it/documents/Agata-proposal.pdf` (2001).

[149] I. Abt *et al.*, Eur. Phys. J. C **54** (2008) 425.

[150] S. R. Elliott *et al.*, Nucl. Instr. Meth. A **558** (2006) 504.

[151] D. González *et al.*, Nucl. Instr. Meth. A **515** (2003) 634.

[152] G. F. Knoll, *Radiation of Detection and Measurement* (third ed.), Wiley, New York (1999).

[153] L. Mihailescu *et al.*, Nucl. Instr. Meth. A **447** (2000) 350.

[154] G. Ottaviani *et al.*, IEEE Trans. Nucl. Sci. **NS-22** (1975) 192.

[155] L. Reggiani *et al.*, Phys. Rev. B **16** (1977) 2781.

[156] B. Bruyneel *et al.*, Nucl. Instr. Meth. A **569** (2006) 764.

Acknowledgments

First of all, I would like to thank Prof. Dr. Allen Caldwell for allowing me to work in his group. Many thanks to Dr. Iris Abt for having selected me as an IMPRS Ph.D. student and for her encouragement all along my three years of studies. Thanks a lot for the help from Dr. Iris Abt and Dr. Béla Majorovits with my studies in their groups. I can hardly forget the paper reading with them in the beer garden. And thanks to all my bosses for their valuable guidance in physics and kind considerations of my personal life.

I appreciate the big help from Xiang. He explained to me patiently all the details about our work during my first days here when I hardly spoke any English. I enjoyed the cooperation with Kevin and Xiang in the background study, with Daniel in the pulse shape simulation and with Dan, Andreas and Gregor in LabVIEW programming. Thanks a lot for their suggestions to my parts of work and selfless sharing their own efforts with me. I received a lot of help from Jens with statistics and C++ problems. I learned plenty from Jozsef about basic electronics. Luciano, Jason, Mike and all the members of the MC groups in both the GERDA and the Majorana collaborations helped a lot with my work on background and pulse shape simulations. I would like to thank them all. My thanks also go to all our interns and summer students for their help with our daily lab work.

Thanks to all the members of the Chinese book-reading club and all the friends and colleagues at our institute for the happy times we spent together.

And finally, a big “thank you” to my wife, for her love, patience and support.